University of California
Santa Barbara

Microplasma jet synthesis of Ni-Fe oxide films for magnetic exchange bias and electrocatalytic studies

A dissertation submitted in partial satisfaction
of the requirements for the degree

Doctor of Philosophy
in
Materials

by

Andrew Christian Pebley

Committee in charge:

Professor Tresa M. Pollock, Co-chair
Professor Michael J. Gordon, Co-chair
Professor Carlos G. Levi
Professor Ram Seshadri

June 2017

The Dissertation of Andrew Christian Pebley is approved.

Professor Carlos G. Levi

Professor Ram Seshadri

Professor Michael J. Gordon, Committee Co-chair

Professor Tresa M. Pollock, Committee Co-chair

April 2017

Microplasma jet synthesis of Ni-Fe oxide films for magnetic exchange bias and electrocatalytic studies

by

Andrew Christian Pebley

Acknowledgements

I could not have gotten to this point in life without the love and unwavering support of my family. My mother, Wendy, has been the stabilizing force in my life and has always supported the decisions I have made. She taught me by example that through hard work and persistence you can always accomplish your goals, no matter the obstacles that may block your path. My Dad, Greg, and Steve have all been father figures in my life and have truly had a hand in shaping the person I have become. I cannot thank my grandparents, aunts, uncles, and cousins enough for the love and guidance they have given me. Without such a caring family, I do not know if accomplishing this PhD would have been possible.

I have been lucky to meet many brilliant and kind people during my 10 years at UCSB. My advisors Drs. Michael Gordon and Tresa Pollock epitomize the level of excellence and rigor that has made the engineering department at UCSB one of the best in the world. Mike truly taught me what it means to be an engineer and has been the most influential figure in my professional development. I have come a long way since I first walked into his introductory chemical engineering class 9 years ago, and through his tutelage, I have gone from a naïve undergraduate student to an engineer ready to make a scientific impact in this world. I will always remain grateful for the opportunity that Mike and Tresa have given me. In addition, my other two committee members, Drs. Ram Seshadri and Carlos Levi, were influential in not only guiding the direction of my research project, but also in my understanding of magnetism and material structure, synthesis, and characterization. I am very grateful to have worked so closely with such intelligent people.

During my graduate studies, I have had the opportunity to learn and use many different materials characterization tools. I want to thank all of the development engineers who I have had the pleasure of working with and who have taught me the foundations of these techniques: Mark Cornish (scanning electron microscopy), Dr. Stephan Kraemer

(transmission electron microscopy), Dr. Youli Li and Miguel Zepeda (X-ray diffraction), Dr. Tom Mates (X-ray photoelectron spectroscopy and secondary ion mass spectroscopy), and Drs. Amanda Strom and Neil Dilley (superconducting quantum interference device, i.e., magnetometer). There was never a problem or design challenge that I could not solve without the help of these amazing people.

I would also like to thank both the Gordon and Pollock research groups for their scientific input and support of my research. I would specifically like to acknowledge Travis Koh, who took me under his wing when I first arrived. He taught me the foundations of microplasmas, and more importantly, demonstrated how to be a successful graduate student. Katie Mackie, my microplasma buddy over the past 4 years, has been influential in my success and has also played a role in keeping my sanity. I will always cherish our conversations and the bond we developed in our never ending endeavor to understand microplasmas. There is nobody I would have rather shared this journey with.

My graduate life would not have been as enjoyable or successful if it was not for all of the wonderful friends I have made along the way. My fellow Gordonites Alex Heilman, Rich Hermann, Katie Mackie, Federico Gonzalez, Elizabeth Decolvenaere, Chris Carach, Travis Koh, Louis Jones, Isaac Riisness, Leslie Chan, Pavel Shapturenka, Ryan Ley, and Sheng-Ping Liang, are the reason why the Gordon group was the best possible group I could have worked for. I am grateful that many, if not all, will be life long friends.

During my first day as a graduate student, I headed to my new desk in my new office, which happened to be adjacent to Alan Liu, a fellow first year Materials student, and I remember saying to myself, "Cool, I think am going to like this guy." Alan turned out to be a close friend and the best roommate I could have asked for. I will never forget the time when we watched IT4 destroy the Lakers, which caused us to destroy our good friend Jim Beam, or our countless attempts at imitating professional basketball players on the tiny toddler hoop in our office, or the constant shade we would throw on LeBron

James. Even though we now live on opposite sides of the country, I know that the bonds we made during our time as PhD students will not allow the distance to weaken our friendship.

Anybody who knows me knows that I have played a lot of Ultimate Frisbee in my college years. This was my outlet, a platform to compete in, to satisfy my competitive drive, to give me a break from the rigors of college. I have played for the Black Tide, Condors, and even professionally for the Los Angeles Aviators. I want to give a shout out to all of my teammates and dear friends I have made while playing this sport. This brotherhood gave me the balance and support network I needed to be able to focus and be successful in my studies. I know that life would have been much harder if it was not for these fierce competitors and friends that I am proud to say I shared the field with.

Lastly, and most importantly, my girlfriend Anya has been my everything. It is hard to describe in words just how important she has been for me in getting through my PhD. Her love, compassion, and relentless efforts in doing whatever she can to make sure I was able to complete this degree has been nothing short of incredible. I am so grateful for the happenstance event that led to us meeting each other, and am so excited for our next chapter in Portland, OR.

Curriculum Vitæ

Andrew Christian Pebley

Education

2017	Ph.D. in Materials Science, University of California, Santa Barbara.
2011	B.S. in Chemical Engineering, University of California, Santa Barbara.

Publications

1. **A. C. Pebley**, A. Peek, T. M. Pollock, and M. J. Gordon, "Microplasma-based growth of biphasic $NiFe_2O_4$/NiO nanogranular films for exchange bias applications," *Chem. Mater.* **2014**, 26, 6026-6032.
2. **A. C. Pebley**, P. Fuks, T. M. Pollock, and M. J. Gordon, "Exchange bias and spin glass behavior in biphasic $NiFe_2O_4$/NiO thin films," *J. Magn. Magn. Mater.* **2016**, 419, 29-36.
3. **A. C. Pebley**, E. Decolvenaere, T. M. Pollock, and M. J. Gordon, "Oxygen evolution on Fe-doped NiO electrocatalysts deposited via microplasma," *Nanoscale* **2017**, submitted.
4. K. E. Mackie, **A. C. Pebley**, M. M. Butala, J. Zhang, G. Stucky, and M. J. Gordon, "Microplasmas for direct, substrate-independent deposition of nanostructured metal oxides," *Appl. Phys. Lett.* **2016**, 109, 033110.

Presentations

1. **A. C. Pebley**, T. M. Pollock, and M. J. Gordon, *Poster*: "Synthesis of nanostructured, biphasic thin films for exchange bias applications using supersonic microplasma jets," *Materials Research Outreach Program Symposium*, Santa Barbara, CA (February **2013**).
2. **A. C. Pebley**, T. M. Pollock, and M. J. Gordon, *Presentation*: "Microplasma-assisted deposition of $NiFe_2O_4$/NiO films for interrogation of exchange bias phenomena," *Materials Research Society Spring Meeting*, San Francisco, CA (April **2014**).
3. **A. C. Pebley**, T. M. Pollock, and M. J. Gordon, *Presentation*: "Microplasma-based growth of $NiFe_2O_4$/NiO nanogranular films for exchange bias applications," *Chemical Sciences Student Seminar*, Santa Barbara, CA (December **2014**).
4. **A. C. Pebley**, T. M. Pollock, and M. J. Gordon, *Poster*: "Microplasma spray deposition of nanostructured $NiFe_2O_4$/NiO thin films for exchange bias applications," *Center for NanoScience Workshop*, San Servolo, Italy (September **2015**).

Awards

1. Finalist for the PANalytical Award (**2014**): Global competition recognizing groundbreaking research that required the use of X-ray characterization techniques.
2. Graduate Student Opportunity Fellow (**2012-2013**): Provides one year of graduate funding to graduate students who contribute to the diversity mission of UCSB.
3. Donald F. Othmer Sophomore Academic Excellence Award (**2008-2009**): Recognizes the top academic sophomore Chemical Engineering student at UCSB.
4. McConnell Foundation Scholar (**2007-2011**): Merit-based award covering $10,000/year of undergraduate tuition and fees.

Abstract

Microplasma jet synthesis of Ni-Fe oxide films for magnetic exchange bias and electrocatalytic studies

by

Andrew Christian Pebley

Ni-Fe oxides have received significant interest from the scientific community because they have attractive magnetic and electrochemical properties for use in next generation data storage and energy conversion technologies. For example, the $NiFe_2O_4$/NiO nanogranular system exhibits the exchange bias effect, a magnetic phenomenon occurring at the interface of a ferro- or ferrimagnet (FM or FiM) and an antiferromagnet (AFM), where the AFM acts to increase the magnetic hardness of the corresponding FM or FiM. Additionally, doping of NiO with Fe has resulted in remarkably high catalytic activities for water splitting, a potential clean energy alternative to fossil fuels. A key challenge in implementing these Ni-Fe oxides for magnetic and electrocatalytic applications is the ability to control film morphology, crystallinity, composition, chemical phase, and doping during synthesis. Moreover, how these physiochemical properties effect magnetic and electrochemical behavior in the Ni-Fe oxide system is not fully understood.

This dissertation focuses on the development and use of a novel synthesis technique, known as microplasma (MP) jet-based deposition, for the fabrication of biphasic $NiFe_2O_4$(FiM)/NiO (AFM) and Fe-doped NiO nanostructured films for fundamental studies of exchange bias and electrocatalysis, respectively. The goal of this work was to understand how MP operation and deposition conditions (e.g., precursor composition, flux, substrate temperature, and post-deposition heat treatment) influence Ni-Fe oxide growth and film microstructure. Specifically, the role of composition, phase frac-

tion, grain size, temperature, and interfacial density on exchange bias phenomena in $NiFe_2O_4$/NiO nanogranular films was investigated. MP jets were also used to realize metastable Fe-doped NiO films with high surface area to assess how doping affects the electrochemical properties of NiO for the oxygen evolution reaction (OER).

Biphasic $NiFe_2O_4$/NiO films of different composition were synthesized using MP jets and post-deposition annealing. The exchange bias effect (H_E) and enhanced coercivity (H_C) were seen at 300 K, which was the first time that H_E has been reported at room temperature in the $NiFe_2O_4$/NiO nanogranular system. These values increased with Ni incorporation, and were rationalized as due to increased $NiFe_2O_4$/NiO interfacial density. Moreover, MP jet deposition of $NiFe_2O_4$/NiO films on heated substrates was explored to realize higher interfacial densities. H_E was observed at low temperatures in these films, but not at room temperature, which was attributed to spin glass coupling arising from structurally disordered interfaces. Through systematic post-deposition heat treatments, it was found that spin glass-like phases disappeared after annealing, and the observed H_E was due to direct exchange coupling between the NiO and $NiFe_2O_4$ phases.

MP jets were also used to deposit high-surface area, metastable Fe-doped NiO films of different composition (up to 20% Fe on a metals basis) at room temperature on indium tin oxide (ITO) substrates for OER catalysis. It was seen that Fe fully incorporated into the NiO rocksalt lattice, decreasing the overpotential for OER (i.e., 360 to 310 mV at 10 mA/cm^2 for NiO and $Ni_{0.95}Fe_{0.05}O$, respectively). Turnover frequency (TOF) calculations demonstrated an improvement in the catalytic activity of the NiO surface with Fe doping, and chronopotentiometry measurements verified that Fe-doped NiO films were mechanically and chemically robust during extended operation under OER conditions.

Overall, this work demonstrates the potential of MP jet deposition as a versatile, one-step approach to realize multi-phase and doped nanostructured oxide films with high interfacial densities and surface areas for a variety of magnetic and energy conversion applications.

Contents

Chapter 1

Introduction: nanomaterials for magnetic exchange bias and electrocatalytic applications

1.1 Dissertation motivation and objectives

Nickel-iron oxide materials have received significant interest from the scientific community in part because of their attractive magnetic and electrochemical properties. For example, the diverse range of magnetic phases accessible across composition space (e.g., Fe_2O_3, $Ni_xFe_{3-x}O_4$, and $Ni_{1-x}Fe_xO$) has allowed for fundamental studies of ferri- and antiferromagnetism [1–4]. Moreover, the thermodynamic stability of multiple magnetic phases over a wide composition range simultaneously has enabled the study of more complex interfacial magnetic phenomena, such as exchange bias in $NiFe_2O_4$/NiO nanogranular systems, which is a promising material for ultra high-density data storage application [5–7]. It is important in these systems to have precise control of magnetic phase, crystallinity, grain size, and interfacial area and structure for fundamental studies of exchange

bias. Tuning composition in Ni-Fe oxides has also been shown to alter the chemical and electrical properties of the material (e.g., bond lengths [8], lattice parameter [9] and electrical conductivity [10]). Doping of NiO with Fe, for instance, has resulted in remarkably better electrocatalytic behavior for the oxygen evolution reaction (OER) compared to pure-phase NiO, where composition, crystallinity, surface area and structure play a crucial role in electrochemical processes [9–11].

A key challenge in implementing Ni-Fe oxides for magnetic and electrochemical applications is the ability to control morphology, chemical phase, composition, doping, and crystallinity during synthesis. Moreover, a detailed understanding of the effects of the aforementioned physiochemical properties on the magnetic and electrochemical behavior of Ni-Fe oxides is lacking. In this dissertation, a novel synthesis technique, known as microplasma jet-based deposition, has been developed to deposit Ni-Fe oxide thin films with tunable morphology, chemical phase(s), composition, crystallinity, and interfacial density and structure to enable fundamental studies of the effects of these physiochemical properties on magnetic exchange bias and electrocatalytic phenomena.

The principal scientific and engineering objectives of this dissertation were to:

1. Design and develop a microplasma-based deposition system for the synthesis of Ni-Fe oxide thin films with the ability to tune composition, doping, chemical phase, crystallinity, and morphology.

2. Study how microplasma operation and deposition conditions (e.g., metal precursor concentration and flux, *in situ* substrate heating, post-deposition annealing, and growth time) influence Ni-Fe oxide growth and the resulting film microstructure.

3. Investigate how composition, phase fraction, grain size, temperature, and interfacial density affect the magnetic properties and the nature of exchange bias coupling in $NiFe_2O_4$/NiO nanogranular films.

4. Realize metastable, Fe-doped NiO films with high surface area to examine the effects of doping on the electronic and electrocatalytic properties of NiO in alkaline electrolytes for OER.

The remainder of this introduction provides the requisite background to better understand and appreciate the scientific work of this thesis. Section 1.2 highlights the basic principles of magnetic materials and the exchange bias effect in nanostructured systems. Section 1.3 focuses on Ni-Fe based oxides as catalysts for the oxygen evolution reaction, as well as the elementary electrochemical methods needed to study these materials. Section 1.4 introduces microplasma jets as a novel approach to realize nanostructured Fe-doped NiO and $NiFe_2O_4$/NiO films for electrocatalysis of OER and exchange bias applications, respectively. Lastly, Section 1.5 provides an outline of this dissertation.

1.2 Magnetism and the exchange bias effect

Intimate contact between a ferromagnet (FM) and an antiferromagnet (AFM) can result in exchange bias (EB), a phenomenon where the strong magnetic anisotropy of the AFM causes a shift in the magnetic behavior of the FM. Exchange bias has also been witnessed in other inhomogeneous systems, such as those involving ferrimagnets (FiM) and spin glass (SG) phases (e.g., FiM/AFM, FM/SG, FiM/SG and SG/AFM). To better appreciate the exchange bias effect, a basic understanding of the magnetic characteristics of the constituent materials involved (i.e., FM, AFM, FiM, and SG) is necessary. A more in depth discussion of magnetism and magnetic materials can be found in [12].

1.2.1 Magnetic materials

Ferromagnetism arises from strong electronic interactions between unpaired valence electrons. The better known ferromagnets (FM) are Fe, Ni and Co, all of which are located in the 3d block of the periodic table. FMs are often characterized by their non-linear, irreversible magnetic response in the presence of an applied magnetic field. Figure 1.1(a) is an example of a typical 'magnetic hysteresis' loop characteristic of FMs with schematic representations of the unpaired electron spin arrangements at important points along the loop. As the magnetic field (H) is increased, the magnetization (M), i.e., magnetic moment per unit volume, increases exponentially at first, and then gradually reaches a maximum value known as the magnetic saturation (M_S). Due to the irreversible nature of FMs, the magnetization does not go to zero when the applied field is removed, but instead retains a finite remanent magnetization (M_{rem}). The magnetization will return to zero when the field is ramped sufficiently high in the opposite direction, and the field value when this occurs is known as the coercivity (H_C), which represents the resistance to reversal of the atomic magnetic moments (i.e., unpaired electrons) in the presence of a magnetic field. Magnets with large coercivity values are often categorized as 'hard' magnets, while those with small values are classified as 'soft'. At even higher reverse fields, the FM will eventually saturate in the reverse direction. The field can then be cycled again in the original direction, resulting in the full hysteresis loop depicted in Figure 1.1(a). It is important to note that the 'long-range' FM interactions between unpaired electron spins only occurs at temperatures below the Curie temperature (T_C), i.e., where the magnetic transition between ferromagnetism and paramagnetism occurs. Above this temperature, the FM will behave like a paramagnet, where the magnetic moments act independently and weakly with an applied field, resulting in a linear M-H response with magnetizations orders of magnitude less than that for FM interactions.

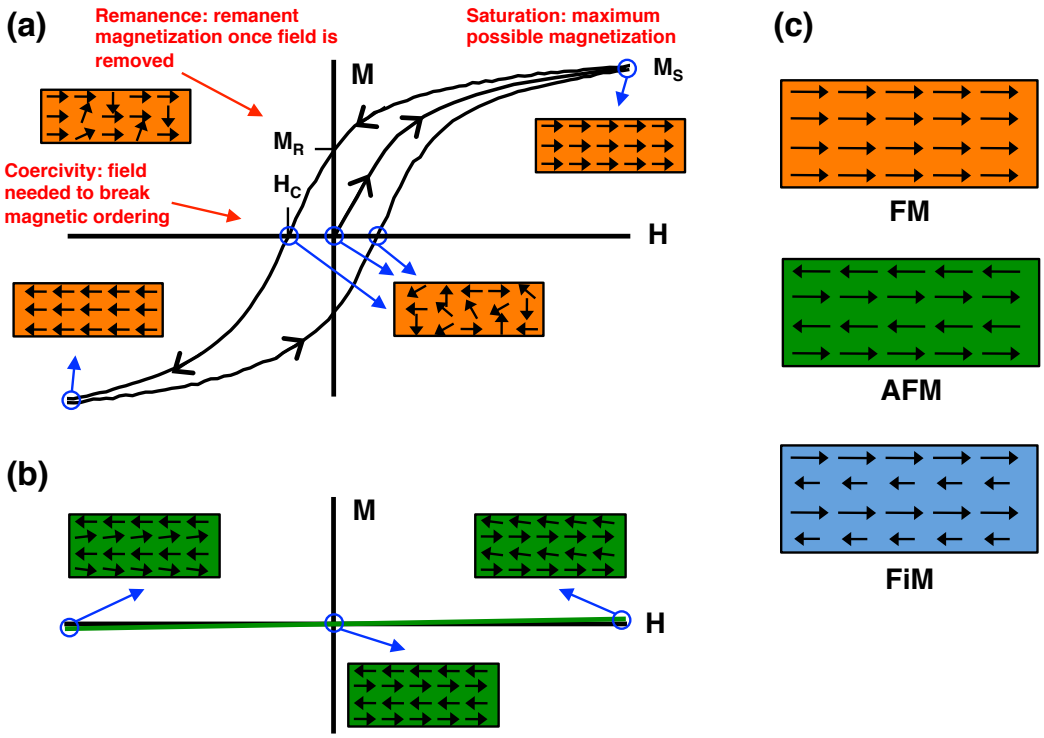

Figure 1.1: (a) Magnetization (M) vs. field (H) hysteresis loop of a typical ferromagnetic (FM) material with schematic representations of the unpaired electron spin arrangements for a single magnetic domain at important points along the curve. M_S = magnetic saturation, M_R = magnetic remanence and H_C = coercivity. (b) M-H behavior of an antiferromagnetic (AFM) material with depiction of the local spin structure at varying magnetic fields. (c) Schematic of local spin structure for a FM, AFM and ferrimagnet (FiM). The FM and FiM are depicted at saturation with a net magnetic moment pointing to the right.

Antiferromagnetism is also a long-range effect, but its behavior is quite different from that of ferromagnetism. The atomic magnetic moments in an antiferromagnet (AFM) are ordered such that neighboring moments are antiparallel to each other (see Figure 1.1(c)). The moments on neighboring atoms cancel each other, resulting in very small magnetization. Similarly to ferromagnetism, antiferromagnetic coupling is only witnessed at temperatures below its transition temperature (i.e., Néel temperature, T_N). Because of the strong magnetic anisotropy induced from coupling, this long-range, antiparallel configuration is maintained in the presence of small to moderate applied fields. As

such, the M(H) behavior is more characteristic of a paramagnet, except that the slight increase in magnetization with field is due to a collective canting of the magnetic moments in the direction of the field (Figure 1.1(b)). Many transition metal (TM) oxides (e.g., NiO, CoO, MnO and Fe_2O_3) are AFMs because of strong electronic interactions (i.e., superexchange) between the O 2p and TM 3d orbitals that results in antiferromagnetic coupling of electrons between next nearest neighbor TM atoms [13].

Ferrimagnets (FiM) are often associated with ferromagnets, as they share the same M-H dependence (c.f. Figure 1.1(a)), but are more similar to antiferromagnets at the atomic level because neighboring magnetic moments couple antiferromagnetically. However, neighboring moments have different magnitudes in the FiM case, and the net magnetization is non-zero. Ferrimagnets can be thought of as two interpenetrating ferromagnetic lattices oriented antiparallel to each other as shown in Figure 1.1(c). The larger of the two moments tends to align with an applied field while the smaller moments align opposite to the field direction. Ferrimagnetism is seen almost exclusively in oxide materials with multiple sub-lattices, such as in spinels (e.g., $NiFe_2O_4$, Fe_3O_4, and $NiCo_2O_4$).

When the above mentioned magnetic materials are confined to very small length scales (< 50 nm), atomic rearrangements at the surface and grain boundaries can take place, and spin glass (SG) phases can form. A spin glass is a structurally disordered magnetic phase, where the individual magnetic moments experience competing magnetic interactions, resulting in a randomized magnetic arrangement. Much like a paramagnet, there are no long-range order interactions and the moments weakly align with an applied magnetic field. When a spin glass is cooled through its blocking temperature (T_B), the magnetic moments will 'lock' into place with the current spin configuration, much like the cooling of a glass through its glass transition temperature, and will effectively be 'blocked' from rearrangement. Given the unique magnetic structure of spin glass phases, they can act as an AFM, and exchange couple with a ferro- or ferrimagnet, or act as an

FM on AFM surfaces in SG/AFM exchange bias systems.

1.2.2 The exchange bias effect

The phenomenon of exchange bias (or exchange anisotropy) was first observed by Meiklejohn and Bean in 1956 in fine particles of partially oxidized Co (20 nm Co particles with ∼nm oxide shell), where they witnessed an anomalous shift in the magnetization curve of Co along the field axis [14]. This shift of the magnetization curve is the macroscopic fingerprint of exchange bias, a phenomenon resulting from exchange coupling across the interface between a ferromagnet (FM) and an antiferromagnet (AFM) where the strong anisotropy of the AFM 'pins' the spins of the FM [15, 16]. Arising from structural defects or grain size distributions in the FM/AFM system, this magnetization shift can be accompanied with an increase in coercivity, H_C (i.e., broadening of the magnetization curve). These effects are only realized if the FM/AFM system is field-cooled through the Néel temperature, T_N, of the AFM, upon which the AFM spins order along an anisotropic 'easy direction' that minimizes the magnetic energy at the FM interface, effectively pinning the FM moment along the field cooled direction (Figure 1.2). The exchange bias effect is not limited to FM/AFM systems, but has also been observed in other inhomogeneous systems, such as those containing ferrimagnets (FiM) and spin glass (SG) phases (e.g., FiM/AFM, SG/AFM, FiM/SG and FM/SG). The net result of exchange bias is the magnetic hardening of the FM material, where large fields are required to flip the spins.

While the physical origin of exchange bias is generally accepted to be the exchange coupling at the FM/AFM interface, the microscopic mechanism by which it occurs is not completely understood, and there have been many models proposed to explain it [17–20]. However, the intuitive picture of exchange bias is simple to understand. Figure 1.3 shows

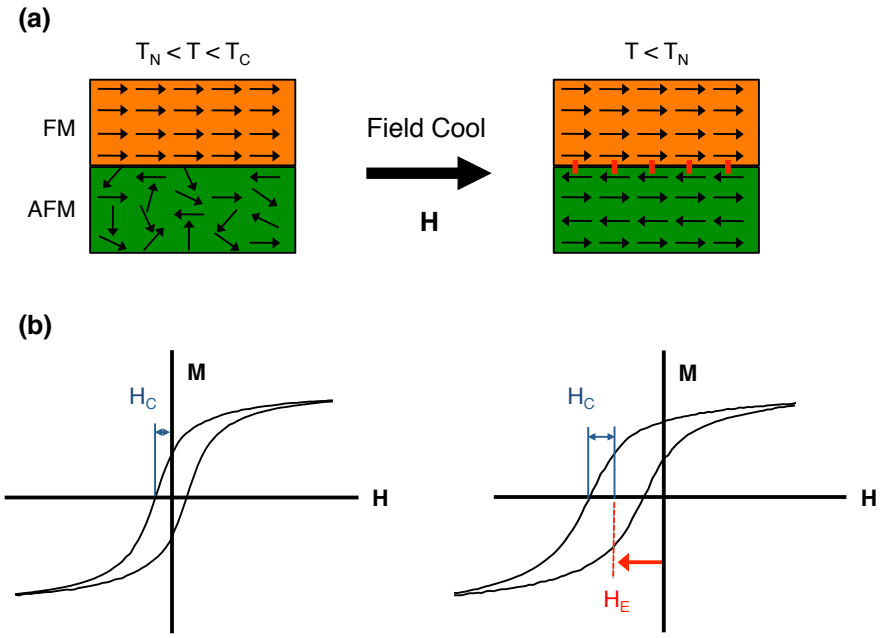

Figure 1.2: (a) Schematic demonstrating the spin rearrangement in the AFM when an FM/AFM material is field cooled through the Néel temperature, T_N, of the AFM, where the red lines represent the built-in exchange coupling between the FM and AFM. (b) Illustration of the shift and broadening of the FM/AFM hysteresis loop from the built-in exchange field, H_E, and enhanced coercivity, H_C, respectively, after field cooling.

the intuitive spin configuration for a FM/AFM couple in different regions of the hysteresis loop. The FM and AFM are originally coupled antiparallel at the interface (assuming an AFM coupling) at large fields and after cooling through T_N of the AFM. When the field is sufficiently reversed, the FM spins will begin to rotate with the field; however, the microscopic torque induced by the AFM at the interface resists this rotation. As such, larger fields are needed to completely flip the FM spins than if uncoupled, and the coercivity in the negative field branch increases. Conversely, when the field is ramped back to positive values, the FM spins are more inclined to rotate with the field because of the assistive torque induced on the FM spins by the AFM. This results in a smaller coercivity in the positive field branch, and therefore, the entire hysteresis loop will shift in the negative field direction. The net effect is that the FM spins will only have one

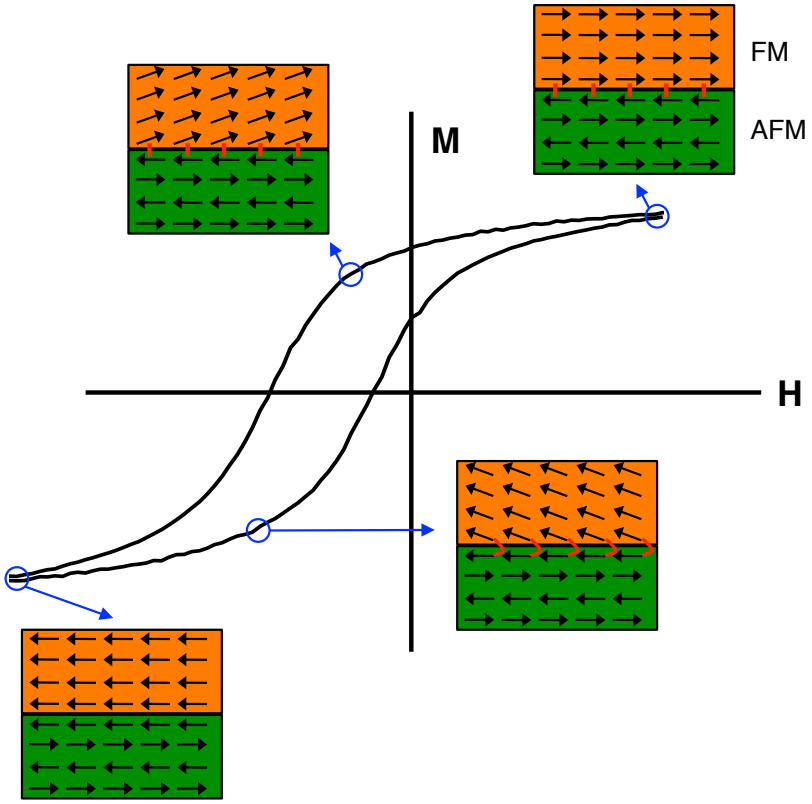

Figure 1.3: Schematic of the spin configurations in an FM/AFM couple at different stages of a hysteresis loop, where the red lines represent the microscopic torque induced on the FM spins from the AFM.

stable configuration (i.e., unidirectional anisotropy), and a larger external field will be needed to overcome this preferred orientation.

1.2.3 Exchange bias in nanostructures

Interest in exchange biased (EB) nanostructures is stimulated by a variety of potential applications ranging from soft to hard magnetic materials, and from ultra-high density data storage to medicine [15, 21]. Exchange biasing has been studied extensively in multilayer structures essential for application in magnetic sensing and random access memories (RAM), such as read/write heads and magnetoresistive RAM (MRAM), respectively. More recently, there has been renewed interest in magnetic nanoparticles (d

< 20 nm) by virtue of their potential in ultra-high density recording [21]. Magnetic particles become superparamagnetic (i.e., magnetically unstable due to thermal fluctuations) with a reduction in size ($\sim$10's of nm's), and therefore, can no longer be used to store memory. In addition, high coercivities of $\sim$ 4–6 kOe need to be maintained at these smaller length scales to be useful for magnetic recording [22]. It has been shown that this so-called 'superparamagnetic limit' can be broken by exchange biasing FM particles with an AFM shell, effectively increasing the anisotropy energy of the FM as well as increasing the coercivity [23]. The ever-increasing industrial demand for miniaturization is pushing the dimensions of magnetic memory sensors and recording devices to smaller and smaller length scales, requiring new and intelligent ways to engineer magnetically hard systems.

A number of solid-state and solution based processes have been explored to synthesize a variety of exchange bias systems. Traditionally, core@shell (FM@AFM) exchange bias systems were achieved by chemically modifying the surface of FM nanoparticles through oxidation [24], sulfidation [25] or nitridation [26]. These techniques are rather limited because only a narrow suite of material systems can be realized, and it is difficult to independently control the size and crystallinity of the particle and shell. Mechanical ball milling of metal and/or ceramic powders has also been extensively used to create exchange bias systems, allowing a large number of exchange coupled systems to be realized (e.g., Co-NiO [27], Ni-NiO [28, 29], FeNi-CoO [30]). Unfortunately, this technique can lead to broad particle size distributions, limited morphology control at the nanoscale, and disordered interfacial regions, which diminish the exchange bias effect. In addition, a variety of solution-based techniques have been employed to overcome some of these shortcomings, as well as to create exchange bias systems with FiM (or FM) nanoparticles dispersed in an AFM matrix, where the continuity of the AFM phase has been shown to strengthen the exchange coupling at FiM/AFM interfaces [6, 31–33]. The strength of

this coupling is quite complex and has been shown to depend on several variables, including particle size, chemical intermixing, and interfacial strain, contact and structure. Moreover, this coupling becomes quite complicated when a spin glass (SG) is present at surfaces and interfaces, which is often the case in nanoparticle or nanogranular EB systems synthesized by mechanical ball milling [28, 34] or wet chemical methods [35, 36]. The disordered spins in the SG can couple to the reversible phase (e.g., FM or FiM) at low temperatures, yielding EB. Although the EB effect can be quite profound in SG systems, the effect does not persist up to room temperature, making these systems undesirable for data storage. As such, it is of significant interest to find novel ways to engineer the magnetic behavior of nanogranular EB systems to achieve magnetically robust nanomaterials at room temperatures.

1.3 Catalysis of the oxygen evolution reaction

In response to diminishing fossil fuel reservoirs and an increasing demand for energy, there has been significant interest in the discovery of economically feasible, alternative energy sources. One promising solution is the production of clean hydrogen gas (H_2), given its high mass-specific energy density, from the electrolysis of water ($2H_2O_{(l)} \longrightarrow 2H_{2(g)}+O_{2(g)}$) by electricity or sunlight [37, 38]. The oxygen evolution reaction (OER), an important half-reaction in water splitting, is a demanding reaction requiring four proton-coupled electron transfers and oxygen-oxygen bond formation (see Equations 1.1 and 1.2). This results in a high-energy barrier and sluggish kinetics, necessitating catalysts to expedite the reaction. The reaction, when operated in acidic conditions, involves the oxidation of two water molecules (H_2O) by losing four electrons (e^-) to give four protons (H^+) and one oxygen molecule (O_2). In basic conditions, four hydroxyl groups (OH^-) are oxidized to form two water molecules and an oxygen molecule with the same number

of electrons involved:

$$2H_2O_{(l)} \longleftrightarrow 4H^+ + O_{2(g)} + 4e^- \qquad (acidic) \tag{1.1}$$

$$4OH^-_{(aq)} \longleftrightarrow 2H_2O_{(l)} + O_{2(g)} + 4e^- \qquad (basic) \tag{1.2}$$

The standard potential for OER against a Pt/H_2 electrode operated at pH=0 (i.e., normal hydrogen electrode or NHE) is 1.23 V; therefore, an external stimulus, such as electricity or sunlight, is required to drive the reaction [37, 38]. The slow kinetics of OER results in high overpotentials (i.e., potential above the thermodynamic value of 1.23 V vs. NHE) that must be overcome for the reaction to occur. As such, there has been intensive research on OER electrocatalysts over the past few decades to accelerate the reaction and lower the overpotential.

Iridium (IrO_2) and ruthenium (RuO_2) oxides are the current state-of-the-art OER electrocatalysts, which when operated in acidic conditions, have demonstrated high activity and low overpotentials (< 250 mV at 10 mA/cm^2) [39–41]. However, the high cost and scarcity of these precious metal-containing catalysts make them impractical for economical, large-scale production of clean H_2 energy from water splitting. A suitable replacement for the electrocatalysis of OER would ideally be earth abundant, affordable, and demonstrate low overpotentials with long-term stability. To this end, considerable effort has been taken to study first-row transition metal oxides (e.g., Mn, Fe, Co, and Ni-based oxides and (oxy)hydroxides)), which have been shown to have intrinsic activities comparable to and even higher than Ru and Ir-based catalysts when operated in alkaline media [42–46]. In particular, Ni-Fe oxides and (oxy)hydroxides have consistently demonstrated the highest activities, and consequently, have become the most promising earth-abundant catalysts for OER [9, 11, 47–50]. A short review of Ni-Fe based OER

catalysts is given below to set the context for the work presented in Chapter 5.

Cyclic voltammetry (CV) is the most prominent technique used to assess the catalytic properties of electrocatalysts, and a picture of the electrochemical setup used in this study is shown in Figure 1.4(a). In this three-electrode electrochemical cell, a potential is applied and cyclically ramped between the working electrode (i.e., catalyst under test) and a reference electrode (e.g., NHE) with the current passed between the working electrode and an inert counter electrode (e.g., C or Pt) recorded. Figure 1.4(b) shows a typical CV curve of an NiO working electrode using an Ag/AgCl/sat'd KCl reference electrode in a 0.5 M KOH electrolyte. As the potential is ramped in the positive direction, the current density through the working electrode is approximately zero until ∼0.4 V vs. Ag/AgCl/satd KCl, where the large increase in current is due to the oxidation of $Ni(OH)_2$ to NiOOH. It is important to note that even though the working electrode is crystalline NiO, it spontaneously forms $Ni(OH)_2$ surface layers when exposed to basic electrolytes. The large increase in current density at higher potentials is from the OER. As the potential is ramped back down to zero, a large cathodic peak is seen at ∼0.3 V, which is from the reduction of NiOOH back to $Ni(OH)_2$.

To directly compare overpotentials between different catalysts and among separate studies, researchers often report overpotentials measured at a current density of 10 mA/cm^2, which is the approximate current density of a 10% efficient solar-to-fuels conversion device [44]. The overpotential (η) here is calculated as the potential difference between the measured potential at 10 mA/cm^2, V_{meas}, and the thermodynamic potential for OER, V_{OER} (i.e., 1.23 V vs NHE):

$$\eta = V_{meas} - V_{OER} \tag{1.3}$$

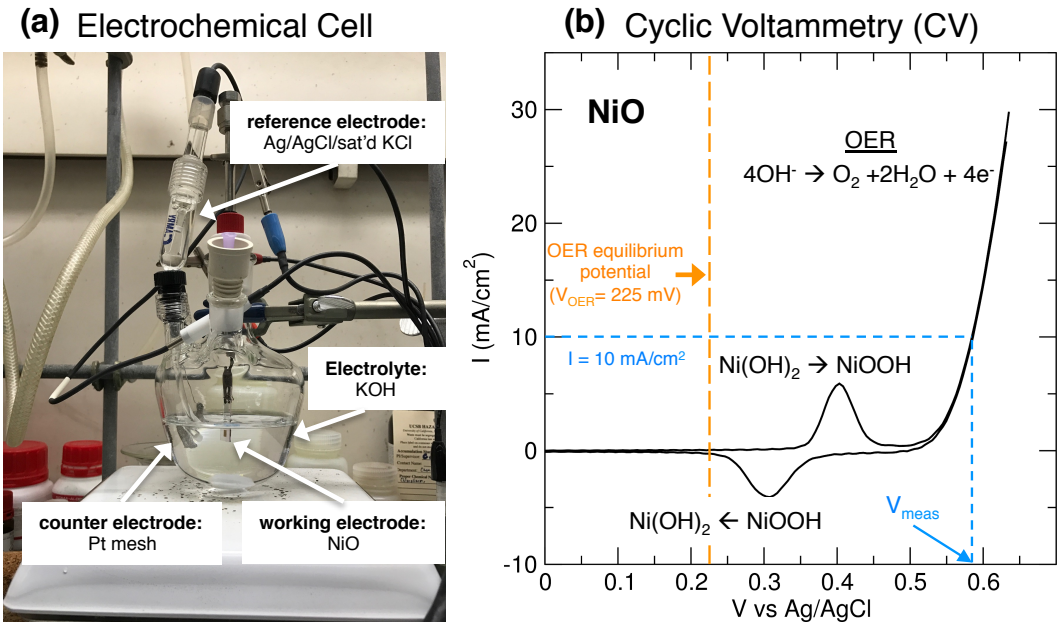

Figure 1.4: (a) Picture of the three-electrode electrochemical cell used for the electrochemical measurements presented in Chapter 5. (b) Cyclic voltammogram (CV) of a NiO electrode obtained with the electrochemical cell depicted in (a). The long-dashed line (orange) represents the equilibrium potential at which the oxygen evolution reaction (OER) occurs when measured against an Ag/AgCl/sat'd KCl reference electrode in an electrolyte with pH=13.7, and the short-dashed lines (blue) demonstrate how to extract the potential at a current density of 10 mA/cm^2 (i.e., V_{meas}).

Figure 1.4(b) demonstrates how to calculate V_{meas} from a CV scan. Since an Ag/AgCl/sat'd KCl reference electrode and a 0.5 M KOH electrolyte with pH=13.7 are used in this experiment instead of an NHE and an acidic electrolyte with pH=0, the thermodynamic potential for OER, V_{OER}, is 0.225 V instead of 1.23 V (see section 5.3.3 for a detailed explanation).

1.3.1 Ni-Fe based nanomaterials as OER catalysts

Although it was discovered in the 1960s that Fe contaminants in nickel hydroxide ($Ni(OH)_2$) electrodes greatly reduce the overpotential for OER, detailed investigations into Ni-Fe oxides and hydroxides did not occur until the 1980s when there was growing

interest in electrochemical splitting of water. Since that time, there have been a considerable number of reports on a variety of Ni-Fe based OER catalysts, including Ni-Fe alloys, Ni-Fe oxides and Ni-Fe layered double hydroxides.

Electrodeposition has probably been the most popular approach used to create Ni-Fe alloy thin films for OER research, as it offers a facile approach to create multicomponent films that strongly adhere to the substrate surface, thereby lowering any overpotentials arising from ohmic loses [51]. Ni-Fe alloys have demonstrated very high activities that are comparable to IrO_2 and RuO_2 (< 300 mV at 10 mA/cm^2), but are limited by the necessity of oxidizing the alloy surface to obtain an OER active phase, which results in structural rearrangements, and as a consequence, hampers the long-term stability of the catalyst [11, 44, 52, 53]. Furthermore, electrodeposition of metals often results in dense films, and because OER activity is directly dependent on the number of active sites exposed to the electrolyte, the ability to improve activity by increasing surface area is rather limited in the Ni-Fe alloy system.

Ni-Fe oxide materials, such as mixed Ni-Fe oxides [9, 54] and $NiFe_2O_4$[55], have also been extensively studied as OER catalysts. A number of synthesis techniques have been used to make mixed Ni-Fe oxides and $NiFe_2O_4$, most notably co-sputtered deposition [56] and solution-based precipitation, followed by high-temperature heat treatment [9, 54]. The mixed Ni-Fe oxides have been shown to have better intrinsic activity than $NiFe_2O_4$, but for the most part, they underperform Ni-Fe alloy catalysts, and it is believed to be because of the integrity of the crystalline oxides [51]. Interestingly, the structural rigidity of Ni-Fe oxides leads to far superior stability compared to Ni-Fe alloys, where a durability of 7000 hours has been recorded for an Fe-doped NiO electrode [56]. Similarly to electrodeposition of Ni-Fe alloys, co-sputtering and spin casting of Ni-Fe oxide nanoparticles formed in solution result in dense, thin films where the number of electrochemically active sites exposed to the electrolyte is restricted.

Recently, there has been resurgence in interest in Ni-Fe layered double hydroxides (LDH) as OER electrocatalysts because of the high accessibility to electrolytes by anion exchange. The main drawback of Ni-Fe LDH is their poor electrical conductivity, which results in large overpotentials from ohmic losses [48]. However, it has recently been demonstrated that hybridizing or directly depositing thin Ni-Fe LDH sheets on a conductive material (e.g., carbon nanotubes [48], graphene [57] and Ni foam substrates [58]), results in excellent electrochemical activity and stability.

Regardless of the synthesis method or type of material, the active phase and the mechanism by which oxygen evolution occurs on Ni-Fe based catalyst surfaces remains unknown. The problem stems from the inability to identify the structure and reaction pathway during operation at OER potentials, both experimentally and theoretically. For a long time, it was believed that the active phase in NiO and mixed Ni-Fe oxides was β-NiOOH, which forms from electrochemically aged $Ni(OH)_2$ surface layers at anodic potentials [59, 60]. However, recently it was shown by Trotochaud *et al.* that γ-NiOOH is more active and that the justification for high activities witnessed for β-NiOOH was due to the incorporation of Fe impurities from unpurified electrolytes [10]. In fact, they showed that γ- and β-NiOOH are poor electrocatalysts for the OER with overpotentials > 400 mV, implying the incorporation of Fe into the Ni oxide film is necessary to realize low overpotentials.

The formation of the $NiFe_2O_4$ phase in mixed Ni-Fe oxides has also been postulated as the active phase, which was challenged by Louie and Bell using *in situ* Raman spectroscopy [11]. They did not observe the characteristic $NiFe_2O_4$ bands at OER potentials, concluding that no $NiFe_2O_4$ was formed and was therefore, not responsible for the high activities of their electrodeposited Ni-Fe films ($\eta < 300$ mV). Furthermore, Friebel *et al.* recently suggested that Fe may be the active center in these catalysts, challenging the pre-existing notion that Fe enhances the activity of Ni (oxy)hydroxides by altering the

local structure and electronic properties of the catalytically active Ni sites. Operando X-ray absorption spectroscopy (XAS) and density functional theory (DFT) calculations of $Ni_{1-x}Fe_x(OH)_2/Ni_{1-x}Fe_xOOH$ catalysts by Friebel *et al.* revealed that the Fe-O bond length is unusually short due to edge sharing with NiO_6 octahedra, resulting in lower activation energies for oxygen intermediate formation (i.e., lower overpotential) on Fe^{3+} compared to Ni^{3+} [8]. Overall, many groups have attempted to discover the active phase and understand the mechanism responsible for improved activity in Ni-Fe based electrocatalysts, but there has yet to be a conclusive, agreed upon explanation.

1.4 Microplasma jets as a novel synthesis technique to realize $NiFe_2O_4$/NiO and Fe-doped NiO films

In this dissertation, MP jets were explored as a new way to synthesize exchange bias systems, with emphasis on the nickel ferrite ($NiFe_2O_4$; FiM) / nickel oxide (NiO; AFM) nanogranular thin film system. This all-oxide system is ideal for the study of exchange bias phenomena because it is chemically and thermally stable, magnetically stable at and above room temperature (i.e., T_N (NiO) = 252 °C), and can easily be synthesized in a variety of nanostructured architectures (i.e., core@shell particles, bilayers and nanogranular thin films). Moreover, with only a limited number of exchange bias studies on this system in the literature, there is a unique opportunity to use microplasma jets as an alternative synthesis route to realize $NiFe_2O_4$/NiO nanogranular films for the fundamental study of exchange bias. Specifically, the effects of microplasma operating conditions (e.g., precursor composition, flux, and substrate temperature) on the resulting composition, morphology, crystallinity, phase fraction, grain size, interfacial density, and magnetic response in the $NiFe_2O_4$/NiO films are discussed in detail.

Although Ni-Fe based materials have shown great promise as electrocatalysts for OER, current synthesis techniques (e.g., co-sputtering, electrodeposition and wet chemical methods) are not ideal for creating high-surface area oxide films to enable higher geometric activities (i.e., larger number of catalytically active sites per unit area). Furthermore, Fominykh *et al.* recently showed that by simultaneously doping rocksalt NiO with Fe and using nanoparticles < 5 nm, low overpotentials and extremely high catalytic activity could be realized [9]. As such, novel, high-pressure microplasma (MP) jets have also been utilized herein to create high surface area Fe-doped NiO films with very small grain sizes (< 15 nm). The unique aspects of microplasma jets, namely non-equilibrium thermodynamics ($T_{electron} >> T_{gas}$, T_{ion}), high pressures (10-760 Torr), and fast jet velocities ($\sim$ 300 m/s), enables the synthesis of highly crystalline, metastable nanomaterials that can be spray deposited onto any substrate to form very high surface area films. A portion of this dissertation describes how varying precursor composition and flux delivered to the microplasma influences film morphology, crystallinity, doping and surface area, as well as how these physiochemical properties correlate with the resulting catalytic behavior.

1.5 Dissertation outline

The scientific efforts put forth in this dissertation are focused on developing and utilizing novel microplasma jets as a new approach to synthesize biphasic $NiFe_2O_4$/NiO and metastable Fe-doped NiO nanostructured films for fundamental studies of magnetic exchange bias and electrocatalysis, respectively. Chapter 2 starts with an introduction of non-equilibrium plasmas for nanomaterial synthesis to give the appropriate background to understand the deposition technique developed in this work. Next, an in depth description of microplasmas is presented with emphasis on their unique operating conditions

that make them ideally suited for synthesis of crystalline, metastable nanomaterials. This is followed by a description of the microplasma jet reactor developed in this work, where the specifics of microplasma operation as well as the tunable parameters available to vary film morphology, crystallinity, and doping are discussed. Chapter 3 describes the effects of Ni/Fe precursor flux ratios delivered to the microplasma and post-deposition annealing on $NiFe_2O_4$/NiO film morphology, composition, crystallinity, phase fraction, and magnetic response. The nature of magnetic exchange bias coupling in nanogranular $NiFe_2O_4$/NiO films, prepared via microplasma jets and post-deposition annealing, is discussed in Chapter 4. More specifically, the effects of annealing on morphology, structure, grain size, and the characteristics of spin glass coupling at $NiFe_2O_4$/NiO interfaces are presented. Chapter 5 details microplasma jet deposition of metastable Fe-doped NiO nanostructured films as electrocatalysts for the oxygen evolution reaction. The effects of precursor compositions and fluxes delivered to the microplasma on film morphology, crystallinity, doping and surface area, as well as how these physiochemical properties correlate with the resulting catalytic behavior for OER are highlighted. Finally, Chapter 6 discusses the conclusions of this dissertation and provides recommendations for future work.

References

[1] J. M. D. Coey, "Noncollinear spin arrangement in ultrafine ferrimagnetic crystallites," *Phys. Rev. Lett.*, vol. 27, no. 17, p. 1140, 1971.

[2] R. H. Kodama, A. E. Berkowitz, E. McNiff Jr, and S. Foner, "Surface spin disorder in $NiFe_2O_4$ nanoparticles," *Phys. Rev. Lett.*, vol. 77, no. 2, p. 394, 1996.

[3] M. T. Hutchings and E. Samuelsen, "Measurement of spin-wave dispersion in NiO by inelastic neutron scattering and its relation to magnetic properties," *Phys. Rev. B*, vol. 6, no. 9, p. 3447, 1972.

[4] R. H. Kodama, S. A. Makhlouf, and A. E. Berkowitz, "Finite size effects in antiferromagnetic NiO nanoparticles," *Phys. Rev. Lett.*, vol. 79, no. 7, p. 1393, 1997.

[5] B. Negulescu, L. Thomas, Y. Dumont, M. Tessier, N. Keller, and M. Guyot, "Exchange biasing in $NiO/NiFe_2O_4$ bilayers," *J. Magn. Magn. Mater.*, vol. 242, pp. 529–531, 2002.

[6] Z. Tian, S. Yuan, S. Yin, L. Liu, J. He, H. Duan, P. Li, and C. Wang, "Exchange bias effect in a granular system of $NiFe_2O_4$ nanoparticles embedded in an antiferromagnetic NiO matrix," *Appl. Phys. Lett.*, vol. 93, no. 22, p. 222505, 2008.

[7] Y. Zhang, F. Zhang, Y. Lu, T. Chen, and L. Yang, "Preparation and characterization of $NiFe_2O_4$/NiO composite film via a single-source precursor route," *J. Phys. Chem. Solids*, vol. 71, no. 4, pp. 604–607, 2010.

[8] D. Friebel, M. W. Louie, M. Bajdich, K. E. Sanwald, Y. Cai, A. M. Wise, M.-J. Cheng, D. Sokaras, T.-C. Weng, R. Alonso-Mori, *et al.*, "Identification of highly active Fe sites in (Ni,Fe)OOH for electrocatalytic water splitting," *J. Am. Chem. Soc.*, vol. 137, no. 3, pp. 1305–1313, 2015.

[9] K. Fominykh, P. Chernev, I. Zaharieva, J. Sicklinger, G. Stefanic, M. Döblinger, A. Müller, A. Pokharel, S. Böcklein, C. Scheu, *et al.*, "Iron-doped nickel oxide nanocrystals as highly efficient electrocatalysts for alkaline water splitting," *ACS Nano*, vol. 9, no. 5, pp. 5180–5188, 2015.

[10] L. Trotochaud, S. L. Young, J. K. Ranney, and S. W. Boettcher, "Nickel–iron oxyhydroxide oxygen-evolution electrocatalysts: the role of intentional and incidental iron incorporation," *J. Am. Chem. Soc.*, vol. 136, no. 18, pp. 6744–6753, 2014.

[11] M. W. Louie and A. T. Bell, "An investigation of thin-film Ni–Fe oxide catalysts for the electrochemical evolution of oxygen," *J. Am. Chem. Soc.*, vol. 135, no. 33, pp. 12329–12337, 2013.

[12] B. D. Cullity and C. D. Graham, *Introduction to magnetic materials*. John Wiley & Sons, 2011.

[13] P. Anderson, "Antiferromagnetism. theory of superexchange interaction," *Phys. Rev.*, vol. 79, no. 2, p. 350, 1950.

[14] W. H. Meiklejohn and C. P. Bean, "New magnetic anisotropy," *Phys. Rev.*, vol. 102, no. 5, p. 1413, 1956.

[15] J. Nogués and I. K. Schuller, "Exchange bias," *J. Magn. Magn. Mater.*, vol. 192, no. 2, pp. 203–232, 1999.

[16] J. Nogués, J. Sort, V. Langlais, V. Skumryev, S. Surinach, J. Munoz, and M. Baró, "Exchange bias in nanostructures," *Phys. Rep.*, vol. 422, no. 3, pp. 65–117, 2005.

[17] D. Mauri, H. Siegmann, P. Bagus, and E. Kay, "Simple model for thin ferromagnetic films exchange coupled to an antiferromagnetic substrate," *J. Appl. Phys.*, vol. 62, no. 7, pp. 3047–3049, 1987.

[18] M. Stiles and R. McMichael, "Model for exchange bias in polycrystalline ferromagnet-antiferromagnet bilayers," *Phys. Rev. B*, vol. 59, no. 5, p. 3722, 1999.

[19] T. Schulthess and W. Butler, "Consequences of spin-flop coupling in exchange biased films," *Phys. Rev. Lett.*, vol. 81, no. 20, p. 4516, 1998.

[20] D. Givord, V. Skumryev, and J. Nogués, "Exchange coupling mechanism for magnetization reversal and thermal stability of Co nanoparticles embedded in a CoO matrix," *J. Magn. Magn. Mater.*, vol. 294, no. 2, pp. 111–116, 2005.

[21] R. Kodama, "Magnetic nanoparticles," *J. Magn. Magn. Mater.*, vol. 200, no. 1, pp. 359–372, 1999.

[22] S. Piramanayagam, "Perpendicular recording media for hard disk drives," *J. Appl. Phys.*, vol. 102, no. 1, p. 2, 2007.

[23] V. Skumryev, S. Stoyanov, Y. Zhang, G. Hadjipanayis, D. Givord, and J. Nogués, "Beating the superparamagnetic limit with exchange bias," *Nature*, vol. 423, no. 6942, pp. 850–853, 2003.

[24] T. Seto, H. Akinaga, F. Takano, K. Koga, T. Orii, and M. Hirasawa, "Magnetic properties of monodispersed Ni/NiO core-shell nanoparticles," *J. Phys. Chem. B*, vol. 109, no. 28, pp. 13403–13405, 2005.

[25] J. Greiner, I. Croll, and M. Sulich, "Ferromagnetic-antiferromagnetic interaction in Fe-FeS," *J. Appl. Phys.*, vol. 31, no. 12, pp. 2316–2317, 1960.

[26] H.-M. Lin, C. Hsu, Y. Yao, Y. Cben, T. Kuan, F. Yang, and C. Tung, "Magnetic study of both nitrided and oxidized Co particles," *Nanostruct. Mater.*, vol. 6, no. 5, pp. 977–980, 1995.

[27] J. Sort, J. Nogués, X. Amils, S. Suriñach, J. Munoz, and M. Baró, "Room-temperature coercivity enhancement in mechanically alloyed antiferromagnetic-ferromagnetic powders," *Appl. Phys. Lett.*, vol. 75, no. 20, pp. 3177–3179, 1999.

[28] L. Del Bianco, F. Boscherini, M. Tamisari, F. Spizzo, M. V. Antisari, and E. Piscopiello, "Exchange bias and interface structure in the Ni/NiO nanogranular system," *J. Phys. D: Appl. Phys.*, vol. 41, no. 13, p. 134008, 2008.

[29] S. Doppiu, V. Langlais, J. Sort, S. Suriñach, M. Baro, Y. Zhang, G. Hadjipanayis, and J. Nogués, "Controlled reduction of NiO using reactive ball milling under hydrogen atmosphere leading to Ni-NiO nanocomposites," *Chem. Mater.*, vol. 16, no. 26, pp. 5664–5669, 2004.

[30] S. Mishra, I. Dubenko, J. Losby, S. Roy, N. Ali, and K. Marasinghe, "Magnetic behavior of mechanically milled FeNi-CoO nanocomposites," *IEEE Trans. Magn.*, vol. 40, no. 4, pp. 2716–2720, 2004.

[31] J. Nogués, J. Sort, V. Langlais, S. Doppiu, B. Dieny, J. Munoz, S. Surinach, M. Baró, S. Stoyanov, and Y. Zhang, "Exchange bias in ferromagnetic nanoparticles embedded in an antiferromagnetic matrix," *Int. J. Nanosci.*, vol. 2, no. 1-2, pp. 23–42, 2005.

[32] M. Artus, S. Ammar, L. Sicard, J.-Y. Piquemal, F. Herbst, M.-J. Vaulay, F. Fiévet, and V. Richard, "Synthesis and magnetic properties of ferrimagnetic $CoFe_2O_4$ nanoparticles embedded in an antiferromagnetic NiO matrix," *Chem. Mater.*, vol. 20, no. 15, pp. 4861–4872, 2008.

[33] L. Del Bianco, D. Fiorani, A. M. Testa, E. Bonetti, and L. Signorini, "Field-cooling dependence of exchange bias in a granular system of Fe nanoparticles embedded in an Fe oxide matrix," *Phys. Rev. B*, vol. 70, no. 5, p. 052401, 2004.

[34] E. Passamani, C. Larica, C. Marques, J. Proveti, A. Takeuchi, and F. Sanchez, "Exchange bias and anomalous vertical shift of the hysteresis loops in milled Fe/MnO_2 material," *J. Magn. Magn. Mater.*, vol. 299, no. 1, pp. 11–20, 2006.

[35] L. Wang, C. Zhu, D. Bao, Z. Tian, and S. Yuan, "Giant exchange bias behavior and training effect in spin-glass-like $NiCr_2O_4$/NiO ceramics," *J. Mater. Sci.*, vol. 50, no. 17, pp. 5904–5911, 2015.

[36] Z. Tian, S. Huang, Y. Qiu, S. Yuan, Y. Wu, and L. Li, "Size-dependent scaling of exchange bias in $NiFe_2O_4$/NiO nanogranular systems synthesized by a phase separation method," *J. Appl. Phys.*, vol. 113, no. 14, p. 143906, 2013.

[37] M. G. Walter, E. L. Warren, J. R. McKone, S. W. Boettcher, Q. Mi, E. A. Santori, and N. S. Lewis, "Solar water splitting cells," *Chem. Rev.*, vol. 110, no. 11, pp. 6446–6473, 2010.

[38] T. R. Cook, D. K. Dogutan, S. Y. Reece, Y. Surendranath, T. S. Teets, and D. G. Nocera, "Solar energy supply and storage for the legacy and nonlegacy worlds," *Chem. Rev.*, vol. 110, no. 11, pp. 6474–6502, 2010.

[39] H. Over, "Surface chemistry of ruthenium dioxide in heterogeneous catalysis and electrocatalysis: from fundamental to applied research," *Chem. Rev.*, vol. 112, no. 6, pp. 3356–3426, 2012.

[40] Y. Lee, J. Suntivich, K. J. May, E. E. Perry, and Y. Shao-Horn, "Synthesis and activities of rutile IrO_2 and RuO_2 nanoparticles for oxygen evolution in acid and alkaline solutions," *J. Phys. Chem. Lett.*, vol. 3, no. 3, pp. 399–404, 2012.

[41] T. Reier, M. Oezaslan, and P. Strasser, "Electrocatalytic oxygen evolution reaction (OER) on Ru, Ir, and Pt catalysts: a comparative study of nanoparticles and bulk materials," *ACS Catal.*, vol. 2, no. 8, pp. 1765–1772, 2012.

[42] A. Singh and L. Spiccia, "Water oxidation catalysts based on abundant 1st row transition metals," *Coord. Chem. Rev.*, vol. 257, no. 17, pp. 2607–2622, 2013.

[43] M. E. Lyons and M. P. Brandon, "A comparative study of the oxygen evolution reaction on oxidised nickel, cobalt and iron electrodes in base," *J. Electroanal. Chem.*, vol. 641, no. 1, pp. 119–130, 2010.

[44] C. C. McCrory, S. Jung, J. C. Peters, and T. F. Jaramillo, "Benchmarking heterogeneous electrocatalysts for the oxygen evolution reaction," *J. Am. Chem. Soc.*, vol. 135, no. 45, pp. 16977–16987, 2013.

[45] R. Subbaraman, D. Tripkovic, K.-C. Chang, D. Strmcnik, A. P. Paulikas, P. Hirunsit, M. Chan, J. Greeley, V. Stamenkovic, and N. M. Markovic, "Trends in activity for the water electrolyser reactions on 3d M (Ni, Co, Fe, Mn) hydro(oxy)oxide catalysts," *Nat. Mater.*, vol. 11, no. 6, pp. 550–557, 2012.

[46] M. S. Burke, S. Zou, L. J. Enman, J. E. Kellon, C. A. Gabor, E. Pledger, and S. W. Boettcher, "Revised oxygen evolution reaction activity trends for first-row transition-metal (oxy) hydroxides in alkaline media," *J. Phys. Chem. Lett.*, vol. 6, no. 18, pp. 3737–3742, 2015.

[47] O. Diaz-Morales, I. Ledezma-Yanez, M. T. Koper, and F. Calle-Vallejo, "Guidelines for the rational design of Ni-based double hydroxide electrocatalysts for the oxygen evolution reaction," *ACS Catal.*, vol. 5, no. 9, pp. 5380–5387, 2015.

[48] M. Gong, Y. Li, H. Wang, Y. Liang, J. Z. Wu, J. Zhou, J. Wang, T. Regier, F. Wei, H. Dai, *et al.*, "An advanced Ni-Fe layered double hydroxide electrocatalyst for water oxidation," *J. Am. Chem. Soc.*, vol. 135, no. 23, pp. 8452–8455, 2013.

[49] A. S. Batchellor and S. W. Boettcher, "Pulse-electrodeposited Ni–Fe (oxy) hydroxide oxygen evolution electrocatalysts with high geometric and intrinsic activities at large mass loadings," *ACS Catal.*, vol. 5, no. 11, pp. 6680–6689, 2015.

[50] J. Wang, L. Ji, and Z. Chen, "In situ rapid formation of a nickel–iron-based electrocatalyst for water oxidation," *ACS Catal.*, vol. 6, no. 10, pp. 6987–6992, 2016.

[51] M. Gong and H. Dai, "A mini review of NiFe-based materials as highly active oxygen evolution reaction electrocatalysts," *Nano Res.*, vol. 8, no. 1, pp. 23–39, 2015.

[52] M. D. Merrill and R. C. Dougherty, "Metal oxide catalysts for the evolution of O_2 from H_2O," *J. Phys. Chem. C*, vol. 112, no. 10, pp. 3655–3666, 2008.

[53] R. Solmaz and G. Kardaş, "Electrochemical deposition and characterization of NiFe coatings as electrocatalytic materials for alkaline water electrolysis," *Electrochim. Acta*, vol. 54, no. 14, pp. 3726–3734, 2009.

[54] L. Trotochaud, J. K. Ranney, K. N. Williams, and S. W. Boettcher, "Solution-cast metal oxide thin film electrocatalysts for oxygen evolution," *J. Am. Chem. Soc.*, vol. 134, no. 41, pp. 17253–17261, 2012.

[55] N. Singh and R. Singh, "Electrocatalytic properties of spinel type $Ni_xFe_{3-x}O_4$ synthesized at low temperature for oxygen evolution in koh solutions," *Indian J. Chem. Sect A-Inorg. Bio-Inorg. Phys. Theor. Anal. Chem.*, vol. 38, pp. 491–495, 1999.

[56] E. L. Miller and R. E. Rocheleau, "Electrochemical behavior of reactively sputtered iron-doped nickel oxide," *J. Electrochem. Soc.*, vol. 144, no. 9, pp. 3072–3077, 1997.

[57] X. Long, J. Li, S. Xiao, K. Yan, Z. Wang, H. Chen, and S. Yang, "A strongly coupled graphene and FeNi double hydroxide hybrid as an excellent electrocatalyst for the oxygen evolution reaction," *Angew. Chem. Int. Ed.*, vol. 126, no. 29, pp. 7714–7718, 2014.

[58] Z. Lu, W. Xu, W. Zhu, Q. Yang, X. Lei, J. Liu, Y. Li, X. Sun, and X. Duan, "Three-dimensional NiFe layered double hydroxide film for high-efficiency oxygen evolution reaction," *Chem. Commun.*, vol. 50, no. 49, pp. 6479–6482, 2014.

[59] H. Bode, K. Dehmelt, and J. Witte, "Nickel hydroxide electrodes. 2. oxidation products of nickel (2) hydroxides," *Zeitschrift fur Anorganische und Allgemeine Chemie*, vol. 366, no. 1-2, p. 1, 1969.

[60] M. E. Lyons and M. P. Brandon, "The oxygen evolution reaction on passive oxide covered transition metal electrodes in aqueous alkaline solution. part 1-nickel," *Int. J. Electrochem. Sci*, vol. 3, no. 12, pp. 1386–1424, 2008.

Chapter 2

Non-thermal plasmas: physics and materials synthesis

This chapter gives a brief introduction to plasmas and their use for nanomaterial synthesis to provide the context necessary to appreciate the advantages of microplasma-based deposition. A detailed description of microplasma physics and operating regime, as well as the unique properties characteristic of microplasmas that provide certain advantages over non-equilibrium plasmas for nanomaterial synthesis is given. Finally, the microplasma jet reactor developed in this work for the deposition of a variety of Ni-Fe oxide films is discussed in detail. The capabilities and tunable operating parameters of the microplasma system and their effect on film morphology, composition, and crystallinity are highlighted.

2.1 Introduction to plasmas

A plasma is a quasi-neutral, ionized gas composed of equal populations of ions and electrons [1]. Plasmas are often characterized in terms of the energy, or temperature, of the ions (T_i), neutral gas species (T_g), and electrons (T_e), as well as the density

of charge carriers present (n). Moreover, they can be categorized as either being in equilibrium, where the energies of the neutrals, ions, and electrons are approximately the same ($T_g \sim T_i \sim T_e$), or not in equilibrium, where the energy of the electrons is significantly greater than the neutrals and ions ($T_e >> T_g, T_i$). Examples of equilibrium, or thermal, plasmas include stars, coronas, and arcs, all of which are strongly ionized and form at high pressures. High collisional frequencies effectively transfer heat to the gas, resulting in gas temperatures often in excess of thousands of Kelvin. Conversely, the gas temperature in non-equilibrium plasmas, such as in direct-current glow discharges and inductively coupled radio frequency plasmas, can be as low as room temperature (0.026 eV), while the electrons can achieve temperatures between ∼10,000 and 50,000 K (1–5 eV) [1]. Non-equilibrium plasmas are often formed at low-pressures (i.e., 1 to 1000 mTorr) and are weakly ionized (i.e., 10^{-8} – 10^{-3} of the gas is ionized) [1].

While thermal plasmas can be formed by simply heating the gas to temperatures in excess of the ionization temperature of the gas (e.g., 180,000, 250,000 and 285,000 K for Ar, Ne, and He, respectively), striking non-equilibrium plasmas is a bit more complex. Consider the parallel plate setup shown in Figure 2.1(a). Free electrons, which are initially created from random high-energy cosmic radiation ionization events, are accelerated in an applied electric field between the electrodes. A fraction of these electrons will gain sufficient energy to ionize a neutral gas atom upon collision according to the following reaction:

$$A + e^- \longrightarrow A^+ + 2e^- \tag{2.1}$$

This reaction results in the production of a secondary electron that will in turn be accelerated in the applied electric field, and may ionize another gas atom upon collision. If the electric field is strong enough, this process will continue, resulting in an electron

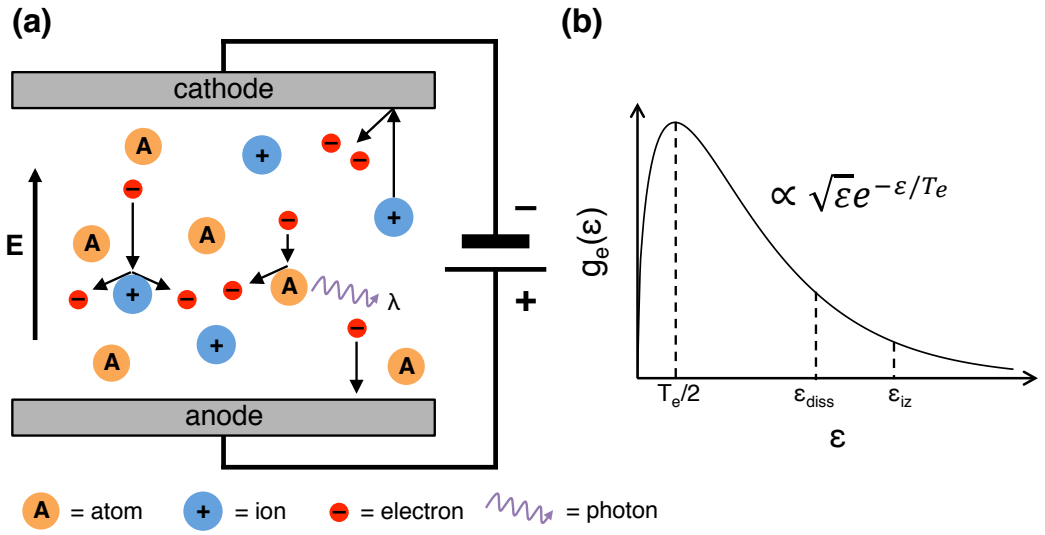

Figure 2.1: (a) Schematic of the elementary processes in a non-equilibrium plasma. λ is the photon emission wavelength from an atom or ion that was excited via electron impact, and E is the electric field. (b) Electron energy distribution function for a non-equilibrium plasma, where ε is the electron energy, T_e is the average electron temperature (energy) of the distribution, and ε_{diss} and ε_{iz} are the dissociation and ionization energies of the gas, respectively.

avalanche. Furthermore, the newly created ions will be accelerated in the opposite direction and upon colliding with the electrode, will produce a shower of secondary electrons. This avalanche process results in an exponential growth in electron density and ionization events, and is responsible for not only striking, but also maintaining the non-equilibrium discharge. Steady state will eventually be reached and the production of ions and electrons from the avalanche process will be balanced by recombination and losses to the container housing the plasma [2].

The electron energy distribution function in non-equilibrium plasmas can be modeled as a Maxwellian [1], and is shown in Figure 2.1(b). Typical low-pressure, non-equilibrium plasmas have average electron energies, T_e, of ~1–3 eV with a small population of electrons having energies in excess of 10 eV in the high-energy tail of the distribution [1]. It is these high-energy electrons that are responsible for ionization and sustaining the discharge of some common plasma forming gases, where electron-impact ionization energies

range between ∼5–25 eV (i.e., the first ionization event for Ar, Ne, and He occurs at 15.6, 21.56, and 24.6 eV, respectively) [3]. While non-equilibrium plasmas have many technological applications, such as dry etching and surface functionalization and cleaning, this dissertation focuses on material synthesis. As such, attributes of non-equilibrium plasmas conducive for nanomaterial production, and their advantages over thermal and liquid phase synthesis techniques are covered in the following section.

2.2 Non-equilibrium plasma synthesis of nanomaterials

A wide variety of gas-phase synthesis techniques have been explored to synthesize nanomaterials that have traditionally been made in the liquid phase. These gas-phase processes are generally operated under conditions in thermal equilibrium, or far from it. In the former case, thermal plasmas have been utilized. For example, thermal plasma torches [4] and sprays [5] have been used to synthesize high melting point materials such as oxides and ceramics. The predominant mechanism for material synthesis here relies on the decomposition of nanoparticle precursors through thermal heating from the hot gas atoms in the plasma, which can be in excess of 10,000 K. A common attribute of this technique is that the uncharged nanoparticles undergo agglomeration, resulting in broad particle size distributions. Additionally, this technique is not suitable for synthesis of temperature sensitive materials, such as semiconductors, which will decompose from the high temperature of the gas in the plasma.

Non-equilibrium plasmas, on the other hand, offer a number of benefits for synthesis of many different nanomaterials with narrow particle size distributions. The large disparity in temperature between the hot electrons (∼10,000 to 50,000 K) and cold neutral

gas atoms (∼300 K) allows for dissociation of chemical precursors via electron impact to produce highly reactive radicals and ions. These reactive growth species collide and react irreversibly to nucleate small nanoclusters and particles. Larger particles grow quickly from the collision and coagulation of initial clusters and particles; this process continues until nanoparticles are big enough to obtain a uniform negative surface charge from accumulation of free electrons in the plasma. The negatively charged particles cease to coagulate as they are repelled from each other due to Coulombic forces, and instead continue to grow through surface reactions with the radicals and ions produced from dissociation of chemical precursors [6]. This growth process limits agglomeration, and allows for the production of nanoparticles (< 10 nm) with narrow size distributions that are not possible in thermal plasma synthesis processes. Furthermore, the irreversible nature of growth in non-equilibrium discharges permits doping of the growing nanoparticles, resulting in the formation of metastable phases that are often unattainable by thermal means. Finally, the unique environment of non-equilibrium plasmas enables the formation of crystalline materials through selective heating of the nanoparticles to temperatures well above that of the neutral gas [6]. Energetic surface processes have been hypothesized to include ion/e- collisional heating, ion/e- recombination, and association of atoms on the growing nanoparticle surface, resulting in heating of nanoparticles to hundreds of Kelvin above the neutral gas temperature [7–9]. This selective heating is essential in forming crystalline nanoparticles, and enables the synthesis of not only high melting point materials, but also temperature sensitive materials. To summarize, the unique characteristics of non-equilibrium plasmas, namely production of reactive species and ions from vapor phase precursors, and the charging and selective heating of nucleated clusters and particles, has enabled the production of small, crystalline nanoparticles ($<$ 10 nm) with narrow size distributions.

Non-equilibrium plasmas have been predominately utilized to create doped [10, 11]

and undoped [12, 13] group IV semiconductors (e.g., C, Si and Ge), compound semiconductors (e.g., oxides [14], nitrides [15], sulfides [16]) and metal nanoparticles [17, 18]. These materials have traditionally been made using liquid phase synthesis methods, which suffer from a few drawbacks. For example, nanomaterial synthesis in liquids often (1) requires many, time consuming processing steps, (2) are thermally limited by the boiling points of the solvent, (3) may require organic solvents and chemicals, and (4) the underlying mechanism for nanoparticle growth is chemistry specific. This may result in contamination from organic ligands (i.e., capping agents used to prevent agglomeration), difficultly in reaching high enough temperatures for crystallization, and a limited number of obtainable nanomaterial systems for a given solvent-precursor system. In contrast, non-equilibrium plasma processes are inherently solvent and ligand free, enabling the production of high purity nanomaterials. Moreover, they are capable of high temperature processing, and the nucleation and growth mechanism is not chemistry specific, which allows for the production of a large variety of crystalline materials (e.g., metals, oxides, and semiconductors). Microplasmas, a special type of non-equilibrium discharge, have gained significant attention recently as a viable method for nanomaterial synthesis as they offer certain advantages over low-pressure discharges as discussed in detail in the following section.

2.3 Microplasma discharges

2.3.1 Physics and operating regime

Microplasmas are hollow-cathode discharges formed inside the cavity of an electrode where at least one of the physical dimensions is reduced to sub-millimeter length scales. Cathode geometries used to house microplasma discharges include parallel plates, cylin-

ders, and spherical cavities, and when coupled with a remote anode, can be operated either in batch or flow-through mode. Figure 2.2 shows a schematic for a batch microplasma reactor using parallel plates, and for a flow-through configuration where a gas line has been attached to the back end of a stainless steel tube. The large current densities (0.1–10 mA/cm^2) characteristic of microplasmas stem from the symmetry and close proximity of the cathode walls. Secondary electrons created at one of the negatively charged cathode walls are accelerated through the cathode fall (i.e., the plasma sheath) and ionize neutral gas atoms, resulting in the negative glow of the discharge. As the electrons approach the opposite cathode wall, high negative electric fields decelerate and then accelerate electrons back into the negative glow, resulting in more ionization events. These oscillating pendulum electrons are responsible for the large current densities seen in hollow-cathode discharges.

Due to their pD scaling (where p is the pressure and D is the sub-mm characteristic dimension of the plasma), microplasmas can be characterized as high-pressure, non-equilibrium plasmas with non-Maxwellian electron energy distributions and high electron density. Generally speaking, high-pressure operation of plasmas leads to instabilities and gas heating, resulting in thermal discharges, such as arcs and atmospheric pressure thermal plasma sprays. The stable, non-equilibrium operation of microplasmas at high pressures, however, can be understood using a 0D energy balance, where the large surface-to-volume ratio of the plasma leads to effective cooling of the ions and neutrals in the plasma. Plasma confinement often results in high electric fields, which leads to the production of electrons with high temperatures and densities that exchange energy with neutrals and ions through gas phase collisions [19, 20]. As such, the power density (P_{heat}/V) transferred from electrons to neutral gas atoms can be approximated as [21]:

$$\frac{P_{heat}}{V} = \varepsilon(T_e) n_g n_e K_e(T_e) \tag{2.2}$$

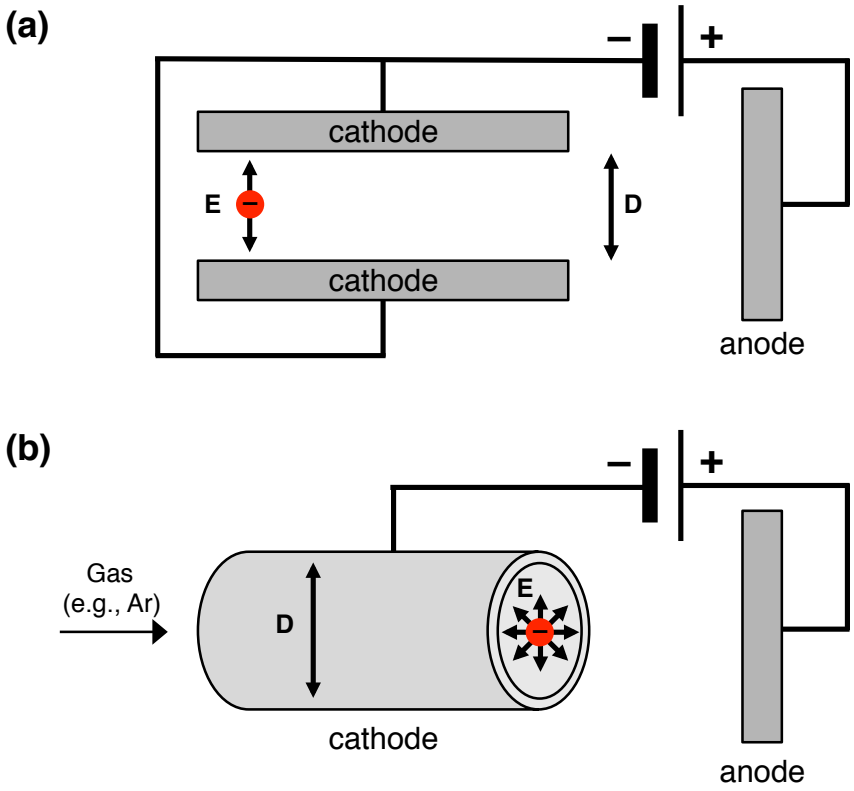

Figure 2.2: Schematic of the electrode geometry for (a) batch and (b) flow-through hollow-cathode microplasmas. The characteristic size of the plasma (D) is given by the size of the cathode cavity ($<$ 1 mm for microplasma). The effect of cathode geometry on the electric field (E) is shown.

Here, ε is the average energy transferred per collision, n_g is the gas density, n_e is the electron density, K_e is the collision rate, and T_e is the effective electron temperature. Assuming that the dominant cooling mechanism is by conduction with the walls containing the plasma, the power loss per unit volume (P_{loss}/V) can be expressed as [22]:

$$\frac{P_{cool}}{V} \propto n_g \frac{T_g^{3/2}}{pD^2} \tag{2.3}$$

where p is the pressure and D is the size of the plasma. At steady state, heat lost to the walls surrounding the plasma must balance the heat transferred to the gas atoms, and

from equations (2.2) and (2.3), we arrive at:

$$p \propto \frac{T_g^{3/2}}{D^2 \varepsilon K_e n_e} \tag{2.4}$$

The terms ε and K_e are a function of the electron energy distribution function (EEDF), which does not follow a Maxwellian distribution in microplasmas, and has an extended high-energy electron tail [23]. However, for the electron energies considered here, ε and K_e increase with the electron temperature, T_e.

Figure 2.3(a) displays the different regimes of plasma operation as a function of the pressure (p) and plasma size (D) for a specific gas composition, input power density, and electrode geometry [21]. The thermal equilibrium line (i.e., $T_g \sim T_e$) is displayed as the bold red curve, and the non-equilibrium regime (i.e., $T_g < 0.1T_e$) is shaded in grey. Between these two regions (i.e., $0.1T_e < T_g < T_e$), the plasma may undergo thermal fluctuations and instabilities [22]. Finally, the black dashed line is the pressure-volume boundary between traditional low-pressure non-equilibrium plasmas and microplasma discharges. This simple energy balance shows that non-equilibrium thermodynamics can be maintained at higher pressures (e.g., atmosphere) by simply reducing the size of the plasma. This size reduction increases both the rate of heat removal and the electric field strength, which decreases the gas temperature and simultaneously increases the electron temperature.

In addition to manipulating plasma thermodynamics with pressure and electrode spacing, the thermal equilibrium line can be shifted by adjusting input power, electrode cooling, and gas composition. For example, increasing the power to the plasma will shift the equilibrium curve down and to the left, where an increase in electron energy increases the heat transfer rate to the neutral gas (Figure 2.3(b)) [24]. This results in a smaller volume-pressure space to achieve non-equilibrium operation. Conversely,

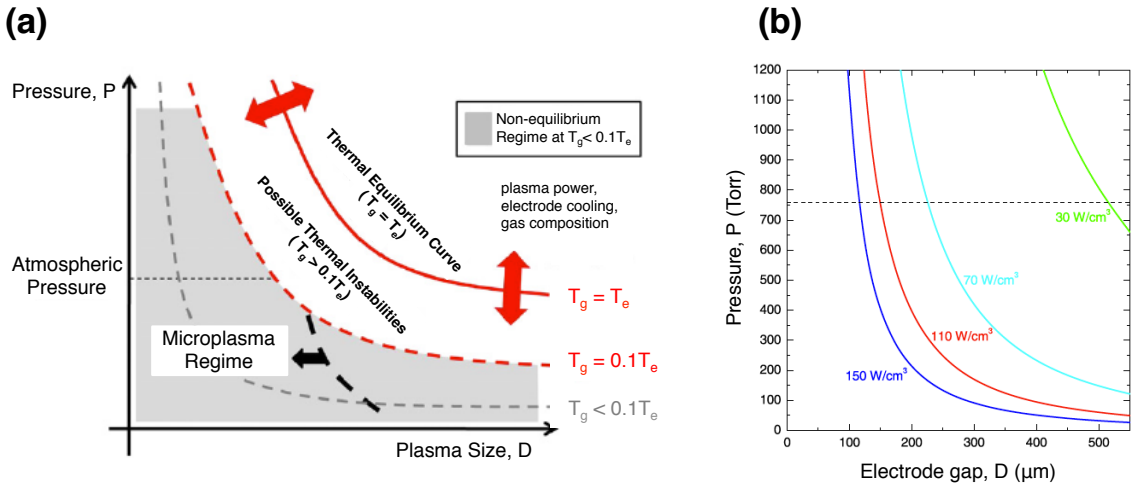

Figure 2.3: (a) Schematic representation of plasma operating regimes as a function of pressure (p) and plasma size (D) calculated for a single power density, electrode geometry and gas composition. The transition between thermal and non-thermal regimes are indicated by the solid and dashed red lines, respectively. The bold dashed line in the non-equilibrium regime distinguishes microplasmas from low-pressure, large-scale plasmas. (b) Thermal equilibrium curves calculated from experimental conditions at different power densities for a parallel plate He discharge. Adapted from Ref. [21].

water-cooling the electrodes enhances the rate of heat removal from the plasma, which would shift the thermal equilibrium curve up and to the right, resulting in a larger non-equilibrium region. The gas composition also plays a critical role in the range of volume-pressure conditions where non-equilibrium operation can be maintained. This can easily be understood by comparing Ar and He discharges. Although the ionization energy for He is relatively high (24.6 eV), the minimum energy needed to excite He (> 21.2 eV) is similar [21]. As such, electrons effectively transfer their energy via ionization events, and relatively low powers are needed to ignite and sustain He plasmas. Low power operation reduces the energy transferred to the gas, enabling the formation of large volume, non-equilibrium He discharges at atmospheric pressures [25]. In contrast, there is a larger energy gap between ionization (15.6 eV) and excitation (> 11.5 eV) events for Ar. The energy transferred in many electron-Ar collisions will result in excitation instead of ionization; therefore, a higher plasma power is required to increase the number

of ionization events for sustaining Ar discharges [21]. This results in a shift of the equilibrium curve down and to the left with respect to a He discharge at the same conditions, where a smaller pressure-volume regime for non-equilibrium operation exists.

This simple 0D energy balance highlights the many design variables that can be tuned to maintain non-equilibrium operation. It also demonstrates the ability to control two system temperatures (gas and electron temperatures) simultaneously by simply confining the plasma. The new opportunities for nanomaterial synthesis using confined non-equilibrium plasmas are discussed in detail in the following section.

2.3.2 Microplasma jets as sources for nanomaterial synthesis

Early on, researchers used the high-energy environment of microplasmas predominately for excimer generation [26], gas remediation [27], and local substrate etching [28]. Only recently have they been leveraged for nanomaterial synthesis. Microplasmas offer many of the same benefits as the low-pressure plasmas discussed in Section 2.2 (i.e., production of reactive radical and ion growth species via electron-impact of chemical precursors, selective heating of gas-phase nanoparticles, and synthesis of small crystalline, nanoparticles with narrow size distributions), but also provide certain advantages that open up new possibilities for nanomaterial synthesis. The following properties of microplasma operation highlight these inherent advantages:

1. *High electron densities and energies*: Plasma confinement enhances local electric fields, which in turn leads to higher electron energies. The electrons in microplasmas do not follow a Maxwellian energy distribution and have a high-energy tail with a sufficient population of high-energy electrons (> 10 eV) that can dissociate vapor phase precursors (e.g., SiH_4, CH_4 and metalorganics) or sputter solid metal sources, producing reactive radicals and ions for nanoparticle growth. Furthermore,

confinement of electrons in the discharge of microplasmas through the pendulum effect, result in high electron current densities (0.1–10 mA/cm^2) and therefore, high frequencies of collisions with gas-phase species. Consequently, vapor phase precursors are dissociated more efficiently, yielding more radical growth species than in low-pressure, non-equilibrium discharges, where lower electron temperatures and densities exist.

2. *High-pressure*: The nucleation mechanism in non-equilibrium discharges is surmised to be from gas-phase collisions between reactive radicals and ions (e.g., Si nanoparticles have been shown to nucleate from Si_xH_y radical polymerization in a low-pressure plasma [29]). At higher pressures, the number of gas-phase collisions between radicals is enhanced, resulting in more efficient particle nucleation. Since microplasmas can be operated at high pressures (e.g., 10–760 Torr), and because they contain high densities of radical species, they offer a more reactive environment for nanoparticle nucleation than low-pressure plasmas.

3. *Continuous flow*: By attaching a gas line to the back of a hollow-cathode, a flow-through microplasma (i.e., microplasma jet) can be realized. This configuration offers certain advantages over non-equilibrium plasmas, which are generally constructed in a batch-type configuration for nanoparticle nucleation and growth. The long residence times characteristic of batch reactors can lead to agglomeration, making it difficult for precise control of particle size and distribution. In contrast, microplasma jets can be operated with very short residence times for nanoparticle synthesis. Vapor phase precursors can be continuously delivered to the hollow-cathode of a microplasma jet, whereby they are dissociated and react to nucleate nanoparticles. The small size of the microplasma reactor ($\sim 10^{-4}$ cm^3), combined with high flow rates ($\sim$100s sccm), results in very short space-times in the reac-

tor (∼1 μs). As such, nanoparticle growth is quickly quenched as the high gas flow velocities (∼300 m/s) rapidly push nanoparticles out of the 'active' reactor volume, resulting in small nanoparticles with narrow size distributions [30, 31]. Furthermore, the gas flow rate and precursor flux can be tuned to control the resulting particle size. Collection of the synthesized particles is easily accomplished by filtration or deposition on substrates downstream, which is inherently difficult in batch-type, low-pressure discharges.

In terms of nanomaterial synthesis, microplasmas have been predominately utilized to create a variety of aerosolized semiconductor and metallic nanoparticles (e.g., Si [30, 32], diamond [33] and NiFe [34]) in the gas-phase for optical, catalytic, battery and photovoltaic applications. There has also been significant interest in coupling microplasmas with aqueous liquid solutions to rapidly form colloidal metallic nanoparticles through metal salt reduction [35, 36]. Despite the growing interest in microplasma-based synthesis of nanomaterials, very little effort has been focused on thin film formation. Koh and Gordon have demonstrated that microplasma jets offer a general synthesis route to create many different single-phase metal (e.g., Cu, Ni and Pd) [31] and metal-oxide (e.g., CuO, NiO and PdO) [37, 38] films with a variety of unique morphologies. However, microplasma jets have yet to be exploited to create more complex systems, such as biphasic and metastable, doped oxide films. Biphasic materials are quite interesting for studying interfacial properties such as magnetic exchange bias, and doped oxides have demonstrated unique magnetic and electrochemical properties. There exists an exciting opportunity to explore microplasma jets for deposition of $NiFe_2O_4$/NiO biphasic films and metastable Fe-doped NiO films for magnetic exchange bias and electrocatalysis applications, respectively, with emphasis on how growth parameters (i.e., precursor flux, composition and substrate temperature) effect the resulting film morphology and proper-

ties. Section 2.4 discusses in detail the microplasma jet reactor developed in this work for the deposition of $NiFe_2O_4$/NiO nanogranular films exhibiting exchange bias (Chapters 3 and 4), and metastable Fe-doped NiO films demonstrating high activity for the oxygen evolution reaction (Chapter 5).

2.4 Microplasma jet-based deposition system

A schematic of the microplasma reactor developed in this work for deposition of Ni-Fe oxide nanostructured films is shown in Figure 2.4. A flow-stabilized, direct current hollow-cathode Ar discharge is struck inside a stainless steel capillary (ID $\leq$ 500 μm) using a current-regulated, negative high-voltage power supply (0–5 kV, 0–25 mA). The plasma circuit is completed through a remote stainless steel ring positioned concentrically around the cathode with Macor insulator. An auxiliary Ar gas flow introduced into the background of the vacuum chamber and a rotary-vane pump are used to stabilize the microplasma jet and regulate the operating pressure (10–760 Torr).

Solid organometallic precursors (i.e., nickelocene, $Ni(Cp)_2$, and ferrocene, $Fe(Cp)_2$) are sublimed in temperature-controlled brass cells. Their vapors are entrained in an Ar gas flow and subsequently delivered to the hollow-cathode, where high-energy, oscillating electrons ($>$ 10 eV) dissociate the precursors via electron impact, resulting in activated growth species (i.e., atoms, ions, and radicals). High-pressure operation ($>$ 10 Torr) leads to many gas phase collisions ($\sim 10^{10}$–10^{11} s^{-1}) that foster nucleation and growth of crystalline nanoclusters and/or particles. Growth is rapidly quenched due to the small size of the hollow-cathode ($< 10^{-4}$ cm^3) and high jet velocity ($>$ 300 m/s), resulting in short residence times ($\sim$1 μs), yielding nanoparticles with narrow size distributions. The microplasma jet is directed at a substrate located downstream of the throat of the capillary for nucleation and growth of nanostructured films. The substrate stage is

equipped with x-y stepper motors for raster scanning during growth, making it possible to deposit films much larger than the cross-sectional area of the microplasma (i.e., cm^2 vs. 0.2 mm^2).

A photo of the microplasma reactor, which was designed and built in-house, is shown in Figure 2.5(a). A stainless-steel vacuum chamber (12 in. diameter with multiple Conflat

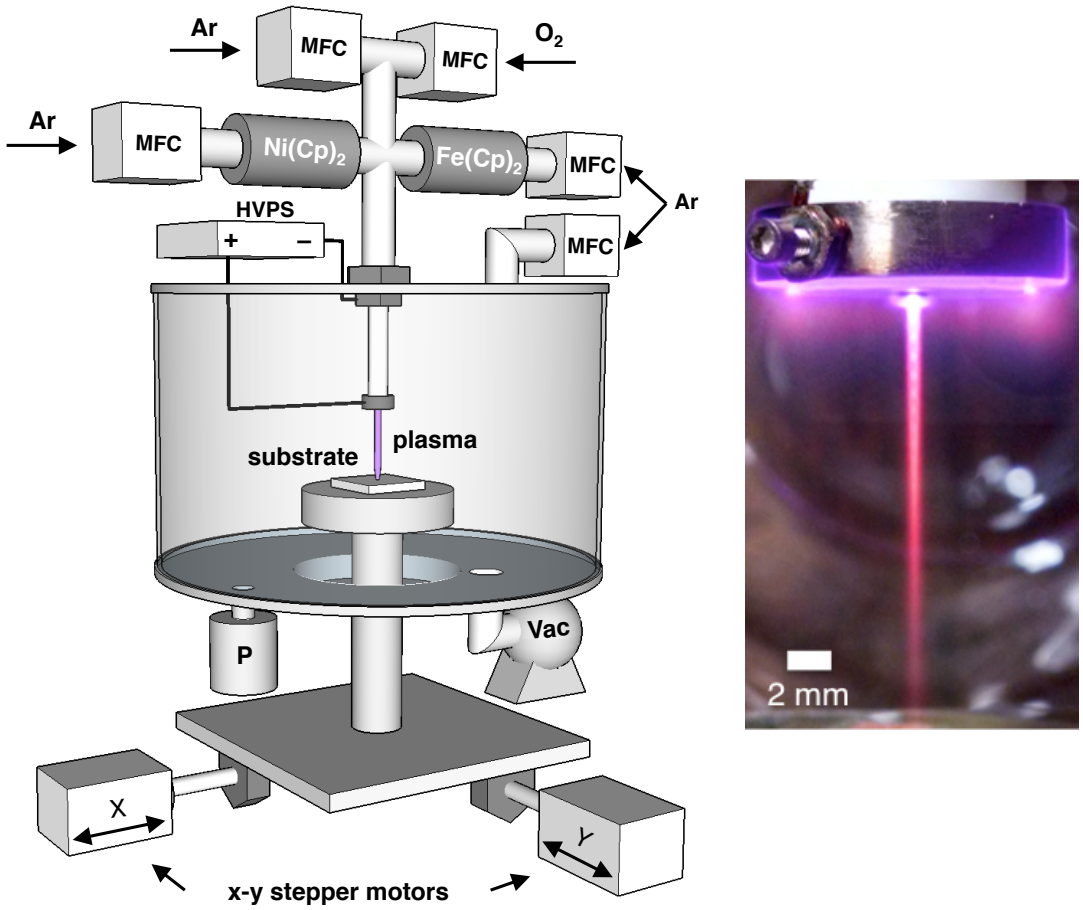

Figure 2.4: Schematic of the microplasma reactor developed in this work to deposit Ni-Fe oxide films. A flow-stabilized, direct-current Ar/O_2 discharge is struck inside a stainless steel capillary tube. $Ni(Cp)_2$ and $Fe(Cp)_2$ vapors delivered to the plasma are dissociated via electron impact, and react to form Ni/Fe-oxide nanoclusters and/or nanoparticles, which are subsequently spray deposited onto a Si or ITO substrate located downstream. The substrate stage is equipped with x-y stepper motors for raster scanning during deposition. HVPS = high voltage power supply, MFC = mass flow controller, Vac = vacuum, and P = pressure transducer. A photo of an Ar microplasma jet operated at 14 Torr is shown on the right.

ports) was used to house all of the microplasma and substrate stage components, and a custom aluminum lid was machined for correct positioning of the capillary tube, high voltage and ground leads, sample shutter, and gas feeds. An MKS Baratron capacitance manometer was used to measure chamber pressure, and mass flow controllers (MFC) were used to precisely regulate gas flows. The bellows is a critical component of the system for large area film deposition because it allows the substrate stage to move independently of the microplasma jet assembly. Attached to the bellows is a set of guide rails on an x-y stage with stepper motors. The motors are controlled through custom-written LabView code to create any desired 2D pattern (e.g., line, square, and 'UCSB'). Figure 2.5(b) shows the stepper motor-guide rail assembly. A two-gear system attaches each stepper motor to a potentiometer that functions as a voltage divider to indicate position.

Figure 2.6(a) details the components of the microplasma jet assembly. A 1/16 in. OD (0.02 in. ID) stainless steel capillary tube was used as the hollow-cathode and was slip fit into a cylindrical Macor insulator. The counter electrode was a 3/16 in. stainless steel hex nut positioned around the Macor, and held in place with three set screws. A copper wire, attached to the hex nut, was fed through an electrically isolated port and connected to ground. Traditionally, the substrate acts as the grounded counter electrode in DC microplasma systems, limiting deposition to conductive materials (e.g., metals) onto conductive substrates only. The remote counter electrode assembly displayed in Figure 2.6(a) enables a larger suite of materials (e.g., metals, oxides, and semiconductors) to be deposited on virtually any substrate (e.g., conductors, insulators, semiconductors, and polymers). A thin Hastalloy sheet functioned as a shutter to protect the substrate during the transient processes of starting and shutting down the plasma, and was rotated via a feedthrough port on the aluminum lid. The substrate stage (Figure 2.6(b)) was machined from stock Inconel 600, a nickel-chromium alloy, which was chosen because of its good oxidation resistance at high temperatures. This enabled high temperature

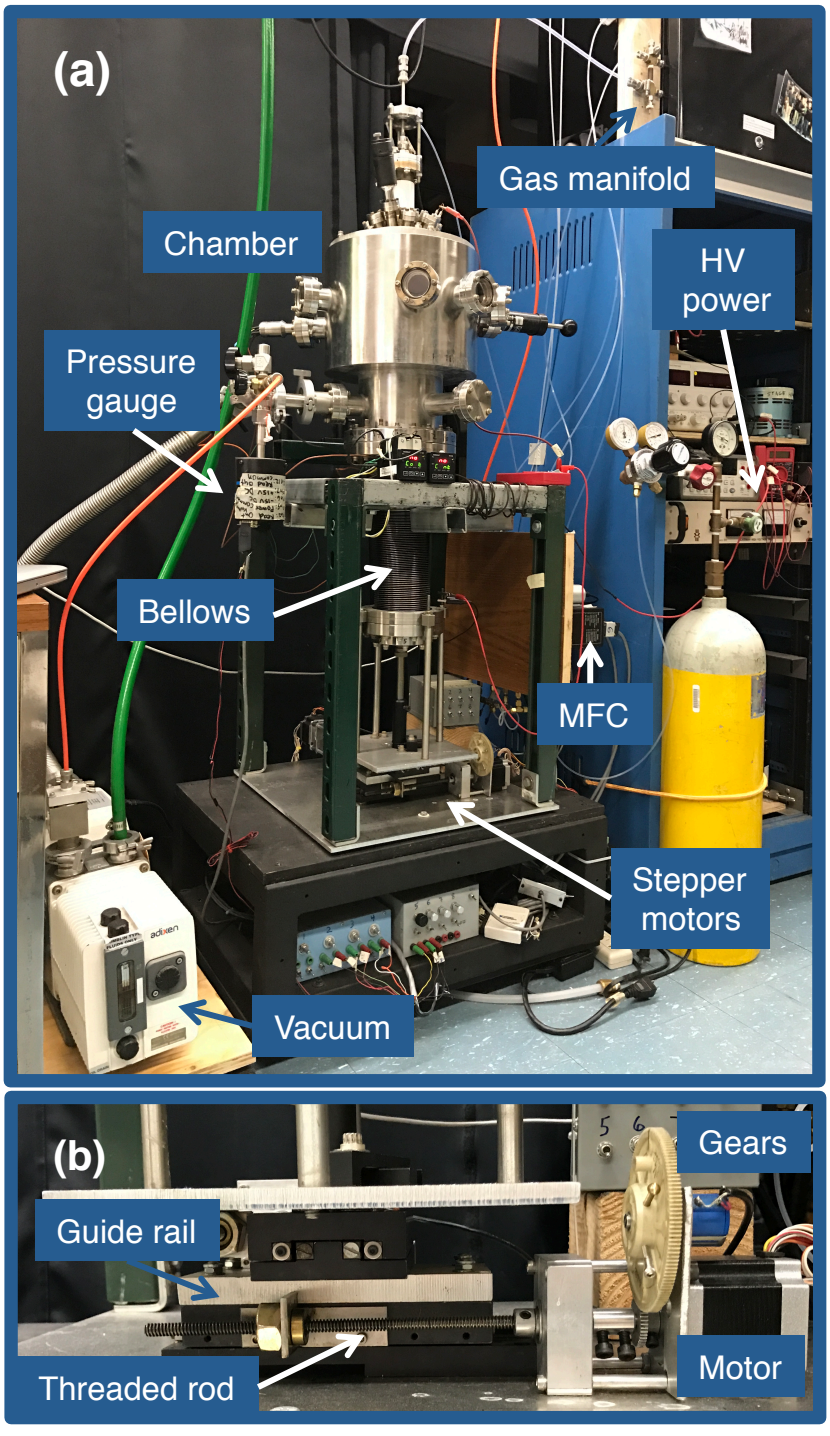

Figure 2.5: Photos of the (a) entire microplasma reactor system, and (b) x-y stepper motor assembly used in this work to deposit Ni-Fe oxide films.

growth in oxidizing environments without jeopardizing the structural or chemical stability of the stage. The substrate was securely fastened using two clips made from the same Inconel alloy. An Inconel cartridge heater was slip fit through a drilled hole in the bottom of the stage that extended to within 1/8 in. of the top surface of the stage that enabled heating to 600 °C during deposition. Two thermocouples were used; one on the substrate surface and one attached to the stage with a PID temperature controller. An alumina cup with a 1 in. opening was positioned over the substrate stage during growth (Figure 2.6(a)) for the purpose of electrically shielding the grounded stage from the plasma, such that only the substrate was 'seen' by the plasma during growth.

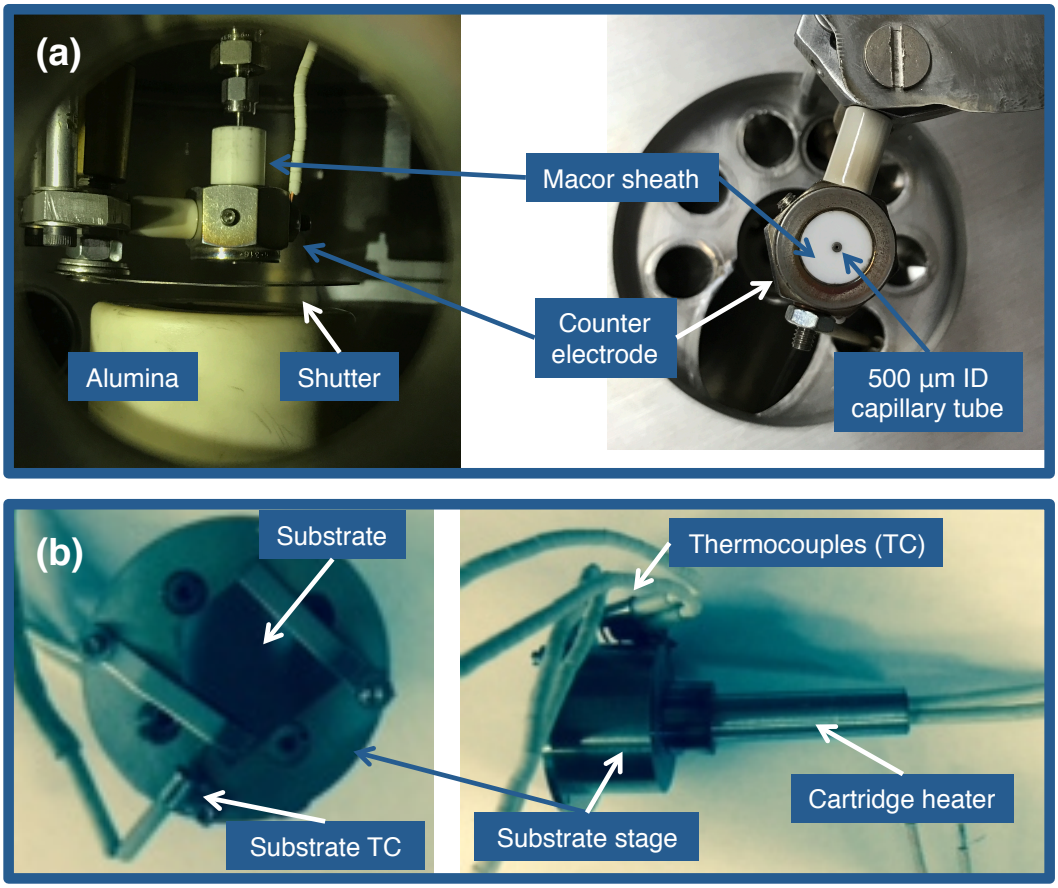

Figure 2.6: (a) Cross-sectional and top-down photos of the microplasma jet assembly, and (b) substrate stage components. TC = thermocouple.

This system offers many controls that can be used to influence growth and tune film stoichiometry, composition, morphology, and structure. For example, by introducing either oxidizing or reducing gases (i.e., O_2 or H_2) into the chamber background, or directly into the hollow-cathode where precursor breakdown occurs, the stoichiometry and morphology of the film can be manipulated. Figure 2.7 shows the film morphology of a NiO and Ni film grown by introducing O_2 or H_2 in the capillary, respectively. The NiO film is porous and composed of large, highly crystalline hierarchical columns, while the Ni film is much more dense with smaller columns and crystalline features. The gas composition of the microplasma jet plays a critical role, not only in film stoichiometry, but also on the growth mechanism and resulting film morphology.

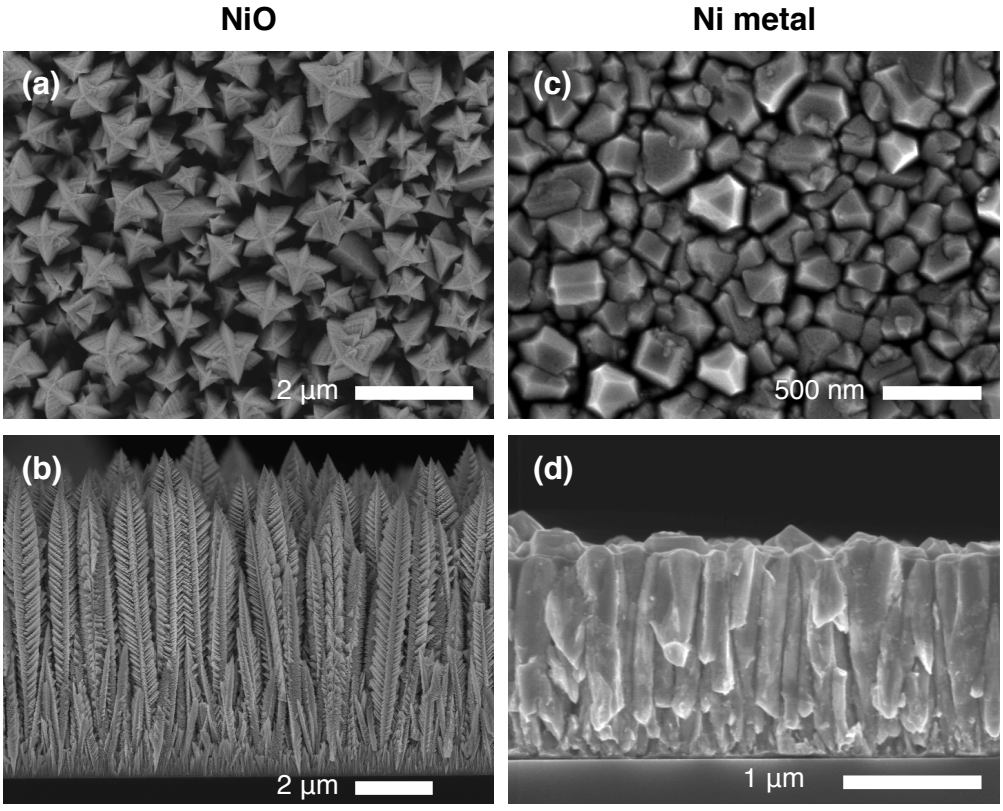

Figure 2.7: Plan and cross-sectional SEM micrographs of (a,b) NiO and (c,d) Ni metal films deposited on Si substrates at 350 °C using an Ar/O_2 or Ar/H_2 microplasma jet, respectively, operated at 20 Torr.

As mentioned above, the substrate stage has been outfitted with a cartridge heater to enable *in-situ* heating during deposition (up to 600 °C). The thermal energy supplied to the substrate results in enhanced surface diffusion, which has a strong effect on the growth mechanism of the film and the resulting morphology and structure. Figure 2.8 exemplifies the substantial changes in $Ni_{1-x}Fe_xO$ film morphology when heating the substrate during deposition, where deposition at a higher temperature (300 °C) results in a film with highly crystalline and textured columns with much larger grain sizes than those observed with a room temperature substrate.

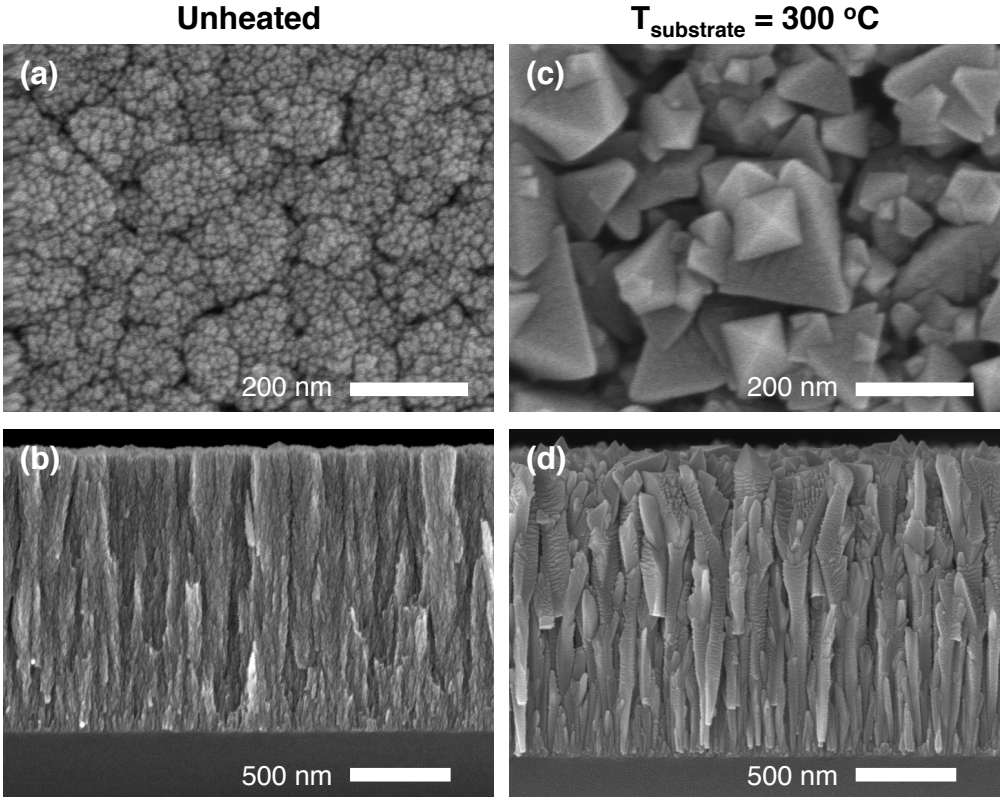

Figure 2.8: Plan and cross-sectional SEM micrographs of $Ni_{0.6}Fe_{0.4}O$ films deposited on (a,b) unheated and (c,d) heated (300 °C) Si substrates with an Ar/O_2 microplasma jet operated at 20 Torr. The thermal energy from the substrate at 300 °C changes the growth mode of the film, resulting in highly crystalline and textured columns with much larger grain sizes than the randomly oriented film deposited at room temperature.

The precursor cell temperature or entrainment flow rate can be varied to adjust the precursor flux delivered to the hollow-cathode. This allows precise control of film composition when depositing multi-component films, such as Ni-Fe oxides. Precursor fluxes were calibrated by growing various $Ni_{1-x}Fe_xO$ films with different composition as a function of precursor cell temperatures and flow rates, as displayed in Figures 2.9(a) and (b), respectively. The effect of composition and substrate heating during deposition on $NiFe_2O_4$/NiO and $Ni_{1-x}Fe_xO$ film morphology, crystallinity, and grain size using an Ar/O_2 microplasma jet were investigated intensively and are presented in Chapters 3, 4, and 5.

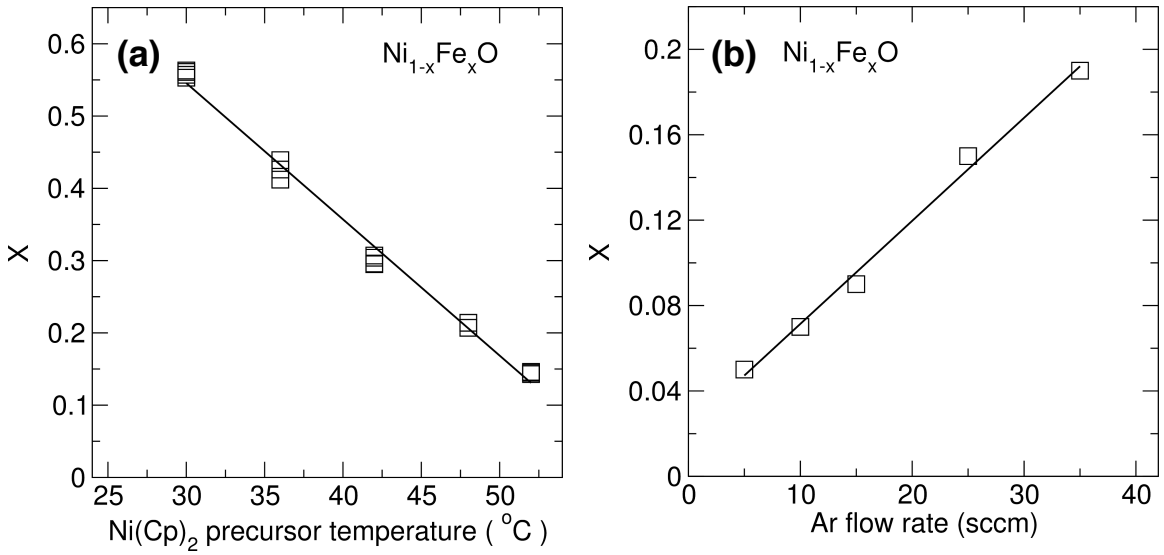

Figure 2.9: $Ni_{1-x}Fe_xO$ film compositions as a function of (a) nickelocene ($Ni(Cp)_2$) cell temperature with a 15 sccm Ar flow rate and at a constant ferrocene ($Fe(Cp)_2$) flux (15 sccm Ar at 30 °C), and (b) Ar flow rate through a $Fe(Cp)_2$ precursor cell at 7 °C and with a constant $Ni(CP)_2$ flux (40 sccm Ar at 20 °C). Films were deposited using an Ar/O_2 microplasma jet operated at 20 Torr, X is the molar composition of Fe calculated on a metals basis (i.e., Fe/Fe+Ni) and measured via energy dispersive X-ray spectroscopy (XPS), and sccm = standard cubic centimeter per minute.

References

[1] M. A. Lieberman and A. J. Lichtenberg, *Principles of plasma discharges and materials processing*. New Jersey: John Wiley & Sons, 2005.

[2] W. Schottky, "Diffusionstheorie der positiven säule," *Phys. Zeits*, vol. 25, no. 23, p. 635, 1924.

[3] E. W. McDaniel, J. B. A. Mitchell, and M. E. Rudd, *Atomic collisions: Heavy-particle projectiles*. New York: John Wiley & Sons, 1993.

[4] J. H. J. Scott, S. A. Majetich, Z. Turgut, M. E. Mchenry, and M. Boulos, "Carbon coated nanoparticle composites synthesized in an RF plasmatorch," in *MRS Proceedings*, vol. 457, p. 219, Cambridge Univ Press, 1996.

[5] H. Herman, S. Sampath, and R. McCune, "Thermal spray: current status and future trends," *MRS Bull.*, vol. 25, no. 07, pp. 17–25, 2000.

[6] U. R. Kortshagen, R. M. Sankaran, R. N. Pereira, S. L. Girshick, J. J. Wu, and E. S. Aydil, "Nonthermal plasma synthesis of nanocrystals: Fundamental principles, materials, and applications," *Chem. Rev.*, vol. 116, no. 18, pp. 11061–11127, 2016.

[7] L. Mangolini, E. Thimsen, and U. Kortshagen, "High-yield plasma synthesis of luminescent silicon nanocrystals," *Nano Lett.*, vol. 5, no. 4, pp. 655–659, 2005.

[8] L. Mangolini and U. Kortshagen, "Selective nanoparticle heating: another form of nonequilibrium in dusty plasmas," *Phys. Rev. E*, vol. 79, no. 2, p. 026405, 2009.

[9] H. Maurer and H. Kersten, "On the heating of nano-and microparticles in process plasmas," *J. Phys. D: Appl. Phys.*, vol. 44, no. 17, p. 174029, 2011.

[10] X. Pi, R. Gresback, R. Liptak, S. Campbell, and U. Kortshagen, "Doping efficiency, dopant location, and oxidation of Si nanocrystals," *Appl. Phys. Lett.*, vol. 92, no. 12, p. 123102, 2008.

[11] B. Stoib, T. Langmann, S. Matich, T. Antesberger, N. Stein, S. Angst, N. Petermann, R. Schmechel, G. Schierning, D. E. Wolf, H. Wiggers, M. Stutzmann, and M. S. Brandt, "Laser-sintered thin films of doped SiGe nanoparticles," *Appl. Phys. Lett.*, vol. 100, no. 23, p. 231907, 2012.

[12] C. Gorla, S. Liang, G. Tompa, W. Mayo, and Y. Lu, "Silicon and germanium nanoparticle formation in an inductively coupled plasma reactor," *J. Vac. Sci. Technol. A*, vol. 15, no. 3, pp. 860–864, 1997.

[13] T. Gries, L. Vandenbulcke, J. Rouzaud, and S. De Persis, "Diagnostics in dusty C–H–O plasmas with diamond and graphitic nanoparticle generation," *Plasma Sources Sci. Technol.*, vol. 19, no. 2, p. 025015, 2010.

[14] J. H. Kim, Y. C. Hong, and H. S. Uhm, "Synthesis of oxide nanoparticles via microwave plasma decomposition of initial materials," *Surf. Coat. Technol.*, vol. 201, no. 9, pp. 5114–5120, 2007.

[15] D. Vollath and K. E. Sickafus, "Synthesis of nanosized ceramic nitride powders by microwave supported plasma reactions," *Nanostruct. Mater.*, vol. 2, no. 5, pp. 451–456, 1993.

[16] E. Thimsen, U. R. Kortshagen, and E. S. Aydil, "Nonthermal plasma synthesis of metal sulfide nanocrystals from metalorganic vapor and elemental sulfur," *J. Phys. D: Appl. Phys.*, vol. 48, no. 31, p. 314004, 2015.

[17] W.-H. Chiang and R. M. Sankaran, "In-flight dimensional tuning of metal nanoparticles by microplasma synthesis for selective production of diameter-controlled carbon nanotubes," *J. Phys. Chem. C*, vol. 112, no. 46, pp. 17920–17925, 2008.

[18] Y. Shimizu, K. Kawaguchi, T. Sasaki, and N. Koshizaki, "Generation of room-temperature atmospheric H_2/Ar microplasma jet driven with pulse-modulated ultrahigh frequency and its application to gold nanoparticle preparation," *Appl. Phys. Lett.*, vol. 94, no. 19, p. 191504, 2009.

[19] D. Mariotti, "Nonequilibrium and effect of gas mixtures in an atmospheric microplasma," *Appl. Phys. Lett.*, vol. 92, no. 15, p. 151505, 2008.

[20] R. Foest, M. Schmidt, and K. Becker, "Microplasmas, an emerging field of low-temperature plasma science and technology," *Int. J. Mass Spectrom.*, vol. 248, no. 3, pp. 87–102, 2006.

[21] D. Mariotti and R. M. Sankaran, "Microplasmas for nanomaterials synthesis," *J. Phys. D: Appl. Phys.*, vol. 43, no. 32, p. 323001, 2010.

[22] Y. P. Raizer, *Gas Discharge Physics*. Berlin: Springer, 1991.

[23] F. Iza, J. K. Lee, and M. G. Kong, "Electron kinetics in radio-frequency atmospheric-pressure microplasmas," *Phys. Rev. Lett.*, vol. 99, no. 7, p. 075004, 2007.

[24] A. J. Wagner, D. Mariotti, K. J. Yurchenko, and T. K. Das, "Experimental study of a planar atmospheric-pressure plasma operating in the microplasma regime," *Phys. Rev. E*, vol. 80, no. 6, p. 065401, 2009.

[25] J. Park, I. Henins, H. Herrmann, G. Selwyn, and R. Hicks, "Discharge phenomena of an atmospheric pressure radio-frequency capacitive plasma source," *J. Appl. Phys.*, vol. 89, no. 1, pp. 20–28, 2001.

[26] R. M. Sankaran, K. P. Giapis, M. Moselhy, and K. H. Schoenbach, "Argon excimer emission from high-pressure microdischarges in metal capillaries," *Appl. Phys. Lett.*, vol. 83, no. 23, pp. 4728–4730, 2003.

[27] C. Jiang, A.-A. Mohamed, R. H. Stark, J. H. Yuan, and K. H. Schoenbach, "Removal of volatile organic compounds in atmospheric pressure air by means of direct current glow discharges," *IEEE Trans. Plasma Sci.*, vol. 33, no. 4, pp. 1416–1425, 2005.

[28] R. M. Sankaran and K. P. Giapis, "Maskless etching of silicon using patterned microdischarges," *Appl. Phys. Lett.*, vol. 79, no. 5, pp. 593–595, 2001.

[29] Y. Watanabe, "Formation and behaviour of nano/micro-particles in low pressure plasmas," *J. Phys. D: Appl. Phys.*, vol. 39, no. 19, p. R329, 2006.

[30] R. M. Sankaran, D. Holunga, R. C. Flagan, and K. P. Giapis, "Synthesis of blue luminescent Si nanoparticles using atmospheric-pressure microdischarges," *Nano Lett.*, vol. 5, no. 3, pp. 537–541, 2005.

[31] T. L. Koh and M. J. Gordon, "Spray deposition of nanostructured metal films using hydrodynamically stabilized, high pressure microplasmas," *J. Vac. Sci. Technol. A*, vol. 31, no. 6, p. 061312, 2013.

[32] S. Askari, M. Macias-Montero, T. Velusamy, P. Maguire, V. Svrcek, and D. Mariotti, "Silicon-based quantum dots: synthesis, surface and composition tuning with atmospheric pressure plasmas," *J. Phys. D: Appl. Phys.*, vol. 48, no. 31, p. 314002, 2015.

[33] R. M. Sankaran and K. P. Giapis, "Hollow cathode sustained plasmamicrojets: Characterization and application to diamond deposition," *J. Appl. Phys.*, vol. 92, no. 5, pp. 2406–2411, 2002.

[34] P. A. Lin and R. M. Sankaran, "Plasma-assisted dissociation of organometallic vapors for continuous, gas-phase preparation of multimetallic nanoparticles," *Angew. Chemi. Int. Ed.*, vol. 50, no. 46, pp. 10953–10956, 2011.

[35] F.-C. Chang, C. Richmonds, and R. M. Sankaran, "Microplasma-assisted growth of colloidal Ag nanoparticles for point-of-use surface-enhanced raman scattering applications," *J. Vac. Sci. Technol. A*, vol. 28, no. 4, pp. L5–L8, 2010.

[36] J. Patel, L. Němcová, P. Maguire, W. Graham, and D. Mariotti, "Synthesis of surfactant-free electrostatically stabilized gold nanoparticles by plasma-induced liquid chemistry," *Nanotechnology*, vol. 24, no. 24, p. 245604, 2013.

[37] T. Koh, E. O'Hara, and M. Gordon, "Growth of nanostructured CuO thin films via microplasma-assisted, reactive chemical vapor deposition at high pressures," *J. Cryst. Growth*, vol. 363, pp. 69–75, 2013.

[38] T. L. Koh, E. C. O'Hara, and M. J. Gordon, "Microplasma-based synthesis of vertically aligned metal oxide nanostructures," *Nanotechnology*, vol. 23, no. 42, p. 425603, 2012.

Chapter 3

Microplasma-based growth of biphasic $NiFe_2O_4$/NiO nanogranular films for exchange bias applications

This chapter has been adapted from: A. C. Pebley, A. Peek, T. M. Pollock, and M. J. Gordon, "Microplasma-based growth of biphasic $NiFe_2O_4$/NiO nanogranular films for exchange bias applications," *Chem. Mater.*, vol. 26, p. 6026, 2014.

3.1 Introduction

A wealth of fabrication techniques have been explored to synthesize particle-based exchange bias systems, albeit with mixed results. The first and most widely studied method consists of chemically modifying transition metal-based FM nanoparticles using partial oxidation, nitridation or sulfidization (e.g., Ni-NiO [1], FeCo-FeCoO [2], Fe-FeS [3], Co-CoN [4]), which can result in exchange bias effects [5]. Issues with these approaches include a limited suite of material combinations and difficulty in independently controlling

the (oxide) shell thickness [6] and crystallinity [7]. The resulting 'disordered' structures often lead to weak exchange bias and the onset of superparamagnetism at temperatures well below room temperature [1, 8]. Mechanical ball milling of metal and/or ceramic powders has also been used to create exchange bias systems where FM (or FiM) nanoparticles are embedded in a continuous polycrystalline AFM matrix, allowing a large number of exchange coupled systems to be realized (e.g., Co-NiO [9], Ni-NiO [10, 11], FeNi-CoO [12]). However, this technique can lead to large particle size distributions, limited morphology control at the nanoscale, and disordered interfacial regions that can diminish the exchange bias effect. Other techniques, such as co-sputtering of FM nanoparticles and AFM films [13], and solution-based processes (e.g., polyol synthesis of $CoFe_2O_4$-NiO [14] and co-precipitation of $NiFe_2O_4$-NiO [15]), have been explored for careful control of particle size and morphology. These ferrite-based systems (e.g., containing $NiFe_2O_4$, $CoFe_2O_4$, or Fe_3O_4) are attractive because ferrites are chemically robust and magnetically stable at high temperature, they have high M_S, and they are more economical than rare-earth oxides [16]. The caveat is that most ferrites are magnetically soft; however, exchange coupling of ferrites with an AFM can increase both magnetic remanence and coercivity [14]. For instance, precipitation of $NiFe_2O_4$ from an Fe-doped NiO matrix has been used to create 8 nm $NiFe_2O_4$ nanoparticles in an NiO matrix, resulting in large hysteresis loop shifts ($\sim$2 kOe) at low temperatrures [15]. Unfortunately, exchange bias disappeared above $\sim$250 K due to exchange coupling of $NiFe_2O_4$ nanoparticles to a spin glass phase that formed because of structural disordering at the $NiFe_2O_4$/NiO interface.

This chapter describes how high-pressure microplasma-based deposition [17] and annealing can be used to synthesize nanostructured $NiFe_2O_4$ (FiM, ferrimagnet) / NiO (AFM) films which exhibit exchange bias at room temperature. Although microplasmas have been used to synthesize a wide variety of nanomaterials (e.g., aerosolized nanoparticles [18–20], structured metals [21], and metal oxides [22–24] for optical, catalytic,

and battery applications; see Refs. [25–27] for excellent reviews), our focus is on direct plasma spray deposition of biphasic, nanogranular oxide materials with high interface density to foster magnetic exchange coupling. More specifically, organometallic precursors were broken down in a flow-stabilized hollow cathode microplasma jet via electron impact to form a directed flux of active growth species (atoms, ions, clusters, etc.) which subsequently react in an oxidizing environment to form mixed nickel-iron oxides. Here, we show how precursor composition, flux and post-growth annealing affect $NiFe_2O_4$/NiO phase fraction, grain size and film porosity, as well as magnetic behavior of the resulting films (i.e., H_E, enhanced H_C and M_R/M_S).

3.2 Experimental Procedure

3.2.1 Microplasma deposition chamber and synthesis

$NiFe_2O_4$/NiO nanostructured films were synthesized with the microplasma (MP) system shown schematically in Figure 2.4. Metallorganic precursors (nickelocene ($Ni(Cp)_2$) and ferrocene ($Fe(Cp)_2$); Strem) were sublimed in separate temperature-controlled cells, entrained in Ar (180 sccm), mixed with O_2 (20 sccm), and subsequently sent to the plasma jet. Iron and nickel oxides formed in the hollow cathode were then spray deposited onto the substrate (300 nm SiO_2 on Si) located ∼1 cm downstream of the capillary exit at a pressure of 150 Torr. The substrate was unheated (∼70 °C due to warming from the MP jet afterglow) and raster scanned at 0.3 mm/s beneath the jet using 12 passes (i.e., as if painting a wall with 12 'coats') to synthesize large area deposits (∼cm^2). Ar makeup gas (50-200 sccm) was also introduced into the chamber background. The composition of deposited films was tuned by adjusting sublimation cell temperatures to control the Ni:Fe flux ratio delivered to the MP jet. Film thickness and Ni:Fe ratio were calibrated

by growing films for different deposition times at constant flux conditions and measuring the resulting film composition using XPS and EDX in the SEM (see Section 3.2.3). Four nickel-iron oxide films were studied with Ni mole fractions (X_{Ni}, metals basis) of 0.26, 0.49, 0.64, and 0.74. As-deposited films were also annealed at 900 °C for 4 hours in air to increase crystal size and allow for phase evolution. Figure 3.1 shows the Ni molar compositions of these films on the pseudo binary phase diagram of Fe_2O_3-NiO in air.

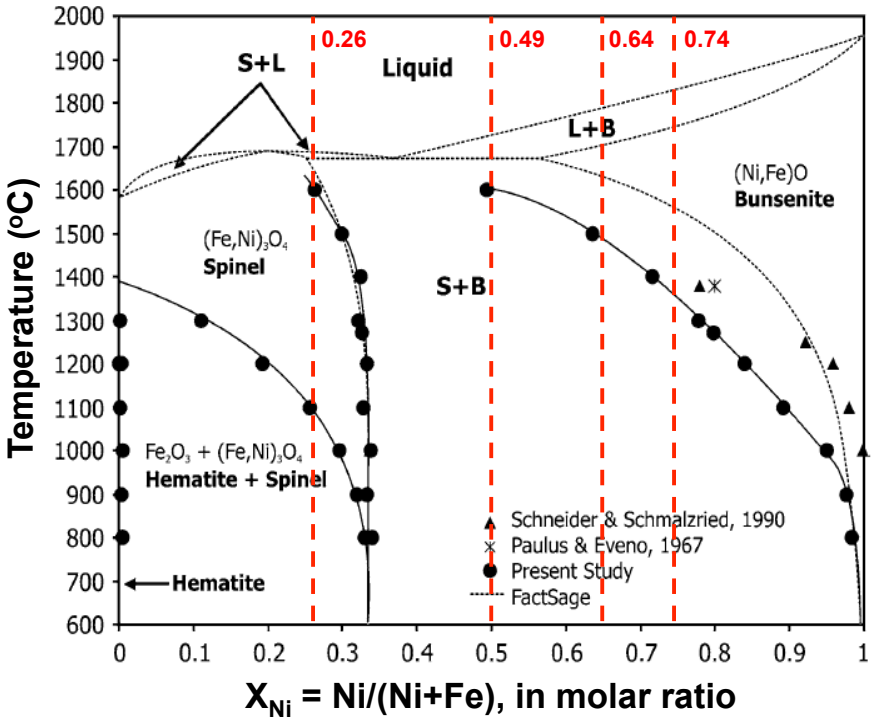

Figure 3.1: Pseudo binary phase diagram of the Fe_2O_3-NiO system in air. The vertical dashed red lines denote the composition of the four microplasma-deposited samples. Adapted from Ref. [28]

3.2.2 Effect of microplasma operation on film deposition

Detailed investigation of the effect of plasma jet operation (e.g., plasma power, growth flux, chamber pressure, etc.) on the morphology of deposited films was not undertaken in this study. Rather, the intent was to understand how film composition and heat treatment affected the biphasic nature of deposits, and to probe the effect of FiM/AFM interfaces on exchange coupling and magnetic behavior. The former can be found in earlier works on microplasma jet-based deposition [17–27]; however, a few trends pertinent to the present work should be mentioned:

1. Higher operating pressures and smaller capillaries result in gas-phase nucleation of nanoparticles, while lower operating pressures (∼150 Torr, those used here), tend to favor the formation of active species such as excited neutrals, ions, and small clusters (see Ref. [17]). The exact role of gas-phase nucleation vs. surface nucleation on the deposited film morphology at these 'low' pressures is unknown at this time.

2. The fluid dynamics associated with jet expansion, i.e., under-expanded vs. pressure-matched supersonic flow, strongly affect the local growth flux hitting the surface due to the presence or absence of shock waves, respectively. All films in the present study were grown under pressure-matched or slightly under-expanded conditions where the growth flux hitting the surface was spatially uniform, turbulent, and well mixed. See Ref. [29] for details.

3. Reducing or oxidizing species in the background gas can be used to tune the level of film oxidation. Such species also assist with the removal of C (and O or H, where appropriate) from the deposited material.

4. High precursor concentration generally results in thicker and more porous films

when the substrate is not heated, i.e., high arrival flux and limited surface diffusion lead to ballistic-like aggregation and high film porosity.

5. Raster scanning the substrate under the jet results in large area (cm^2) films with uniform morphology throughout.

3.2.3 Characterization

A Kratos Ultra X-ray photoelectron spectroscopy (XPS) system was used to measure the atomic composition of the as-deposited films. Films were sputter cleaned with Ar ($\sim$15 nm of the surface was ablated) to remove adsorbed oxygen and carbon from the air, scanned via XPS, and quantified using the CASA software package. Carbon contamination in films was seen to be < 0.9 at% (Figure 3.2(a)). A Physical Electronics 6650 secondary ion mass spectroscopy (SIMS) system was used to verify that the ratio of Ni:Fe was constant throughout the thickness of the film, confirming that the near-surface data obtained from XPS was representative of the entire thickness of the film (Figure 3.2(b)). The crystalline structure of the films was studied using glancing-angle X-ray diffraction (GA-XRD) at 1° with Cu Kα radiation (Rigaku Smartlab), and Rietveld refinement was performed to calculate phase fractions. High-resolution microscopy images were acquired with an FEI XL30 SEM, FEI Tecnai G2 Sphera TEM, and FEI Titan TEM. SEM cross-sectional samples were prepared by cleaving the Si substrate through the deposit center with a diamond scribe and sputter coating with $\sim$1 nm Au to prevent charging. TEM samples were prepared with an FEI HELIOS FIB and thinned to $\sim$100 nm. Additionally, an EDX (energy dispersive X-ray spectroscopy) area scan of the $X_{Ni} = 0.74$ film was obtained with the Titan TEM.

Quantum Design SQUID XL and MPMS 3 magnetometers were used for magnetic characterization. The MPMS 3 was used to heat the annealed films to 600 K ($> T_N$ of

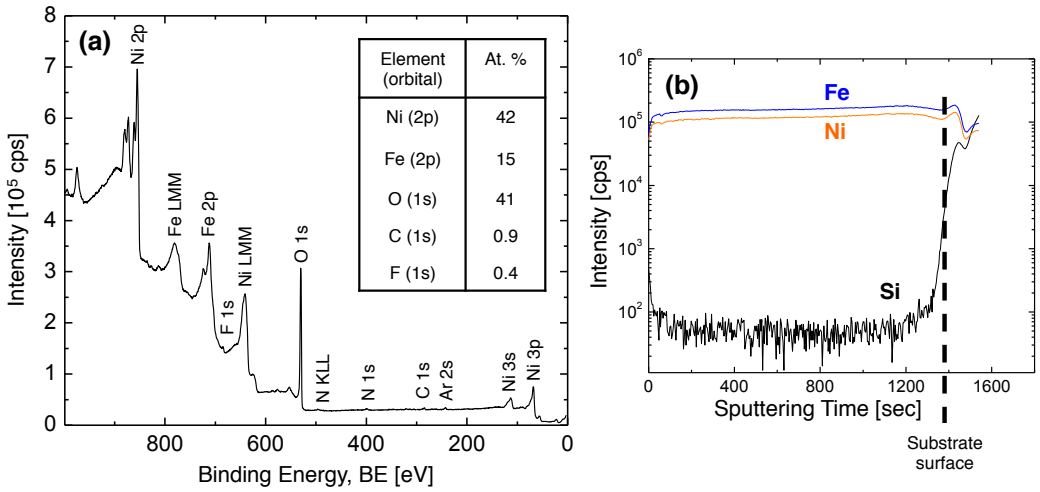

Figure 3.2: (a) XPS of the as-deposited $X_{Ni} = 0.74$ film after Ar sputtering of the surface to remove carbon and oxygen species that adsorbed from the air. Carbon contamination in the as-deposited film was < 0.9 at%. (b) SIMS of the as-deposited $X_{Ni} = 0.49$ film shows that the Fe and Ni composition throughout the film thickness is uniform.

NiO (525 K)), followed by a field cool (FC; 20 kOe) procedure through T_N of NiO down to either 20 or 305 K. After the FC procedure, +20 kOe to -20 kOe M-H hysteresis loops were measured at both 20 and 305 K, where the FC procedure was repeated between each loop measurement to ensure suppression of the training effect [30]. M-H loops (+20 kOe to -20 kOe) were also measured at 20 K in both the SQUID XL and MPMS 3 magnetometers after the films were zero-field cooled (ZFC; 0 Oe).

3.3 Results and Discussion

3.3.1 Morphology of as-deposited films

Plan and cross-sectional SEM images of the four as-deposited films are displayed in Figures 3.3(a)-(d). The iron rich film ($X_{Ni} = 0.26$) is composed of a porous distribution of

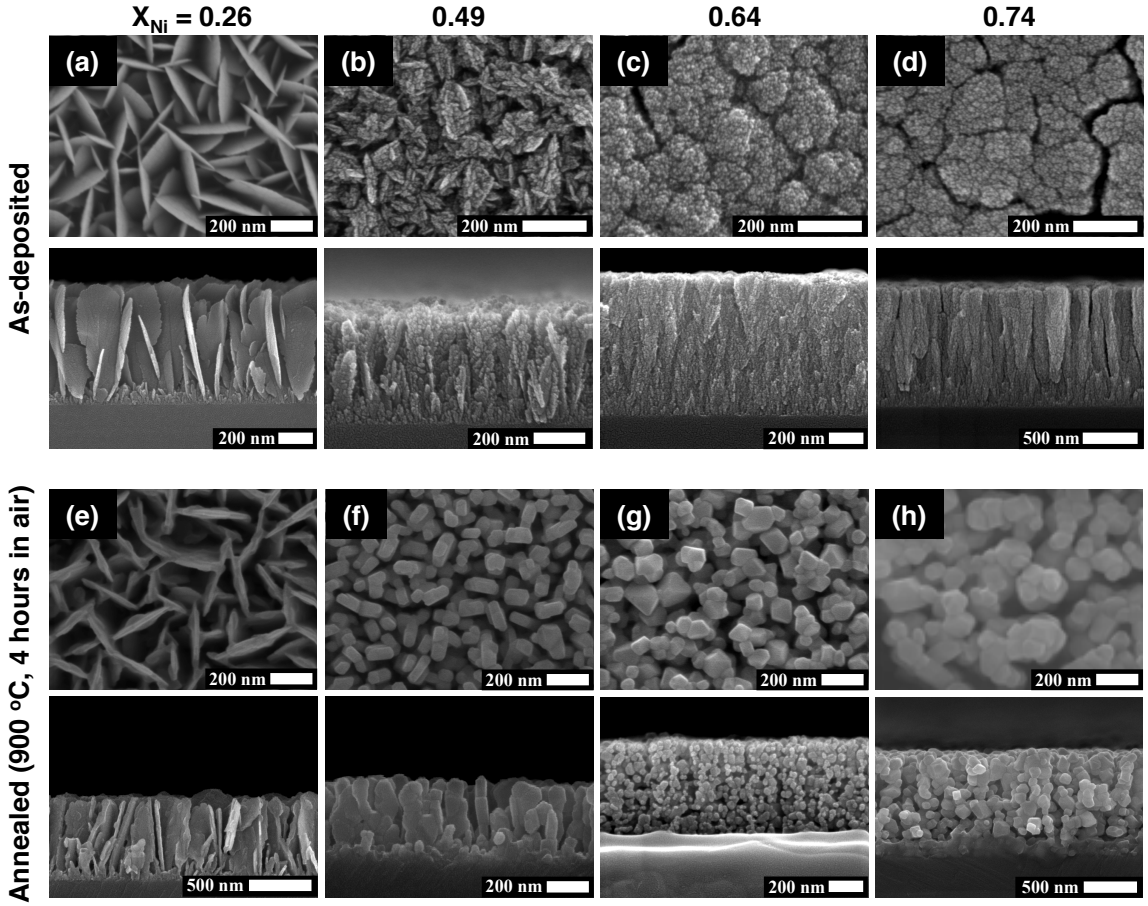

Figure 3.3: Plan and cross-sectional SEM images of as-deposited and annealed (900 °C, 4 h in air) nickel oxide-ferrite films grown via microplasmas at 150 Torr. Ni molar composition, X_{Ni} (metals basis) are (a, e) 0.26, (b, f) 0.49, (c, g) 0.64, and (d, h) 0.74.

thin 2-D nano-sheets with thicknesses of ∼30-40 nm and widths of ∼200-350 nm. Similar morphologies have been seen in β-MoO_3 films created with RF-driven microplasmas at atmospheric pressure [24], suggesting that a common growth mechanism may be involved. For example, high strain at coalescing grain boundaries has been shown to produce Al_2O_3 and Fe_2O_3 deposits with sheet or platelet-like structures [31], even though these forms do not represent relaxed equilibrium crystal habits [32]. In the present case, nickel-iron oxide nanoparticles with randomly oriented fibril textures seem to appear on the surface first, followed by rapid growth of large 2-D nano-sheets.

The increase in porosity with film thickness can be explained by atomic shadowing of the underlying film by the rapidly growing sheets, suffocating the growth of crystals with less favorable orientations. X-ray diffraction (Figure 3.4(a)) shows a relatively sharp peak at ∼35.6° which can be indexed to the (311) reflection of cubic $NiFe_2O_4$. Considering that the recorded peak can also be indexed to the (110) reflection of Fe_2O_3 and the composition of the film is sub-stoichiometric in Ni for $NiFe_2O_4$ (i.e., $X_{Ni} = 0.26 < 0.33$), we cannot rule out the possibility of Fe_2O_3 being present (see phase diagram in Figure 3.1). With similar logic, the presence of Fe_3O_4 cannot be dismissed, but its formation seems highly unlikely given the high partial pressure of oxygen in the system (∼10 Torr) would convert Fe^{2+} to Fe^{3+}, and Figure 3.1 demonstrates that this phase is not thermodynamically favored at the low deposition temperature (∼ 70 °C). The presence of only one clear diffraction peak and the anisotropy of the nano-sheets suggest textured growth out-of-plane in the (311) direction, but random in-plane orientation. Similar (311) texturing behavior has been observed for thin film deposition of nano-sheets of $NiFe_2O_4$ via a chemical bath [33]; however, the film morphology (stacked platelets randomly formed on the substrate) is much different than the structures shown here.

A substantial change in morphology (see Figures 3.3(b)-(d)) from 2-D nano-sheets to densely packed columnar structures composed of spherical nanoparticles (∼5-10 nm) occurs when X_{Ni} is increased from 0.26 to 0.74. Much like the $X_{Ni} = 0.26$ film, a high density of initial fibril textures saturate the surface in the early stages of deposition. Evolution of this dense layer of small grains into tapered columns with cauliflower-like tops during growth is reminiscent of ballistic aggregation [34–36] where growth species from the vapor phase hit and 'stick' to the surface due to low adatom mobilities (i.e., $T_{substrate} << T_{melt}$). Columns that nucleate early and grow from frequent re-nucleation out of the seed layer tend to shadow the underlying film and arrest the growth of less favorably-oriented columns that nucleated later. The morphology of the $X_{Ni} = 0.64$

film is almost identical to $X_{Ni} = 0.74$; whereas, the $X_{Ni} = 0.49$ film has a transitional morphology between the 2-D nano-blade and columnar structures (Figures 3.3(b) and (c)). The high porosity, stretched in-plane column shape, and nanoparticle building blocks suggest a competitive growth mode for this film. XRD (Figure 3.4(a)) of the $X_{Ni} = 0.49$-0.74 films indicate the presence of both $NiFe_2O_4$ and NiO, with increasing intensity of NiO reflections with Ni content. The low signal-to-noise ratio and large peak widths (∼5°) can be attributed to (i) nm-scale crystallites, which are consistent with SEM micrographs, and/or (ii) an amorphous phase when $X_{Ni} > 0.26$.

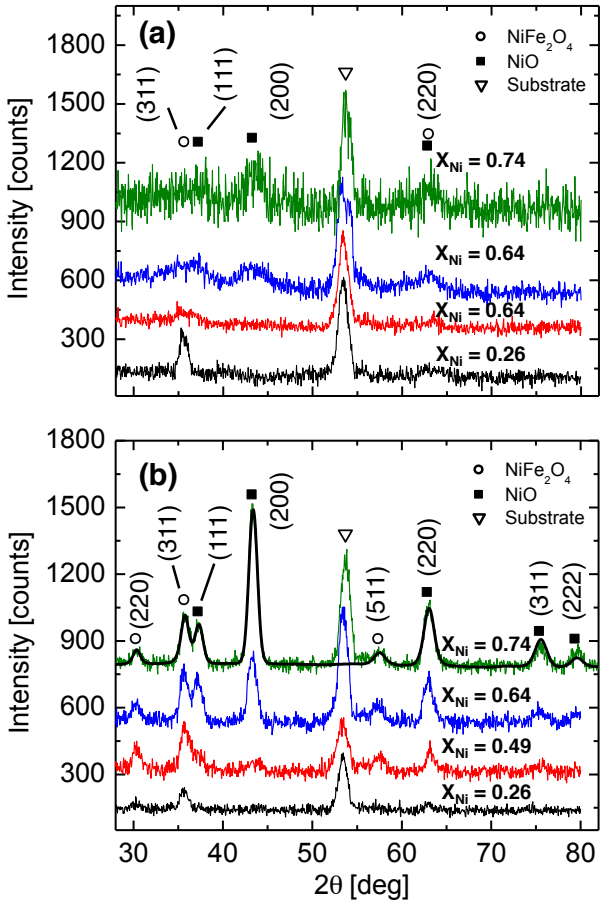

Figure 3.4: XRD spectra of nickel oxide-ferrite films shown in Figure 3.3: (a) as-deposited and (b) heat treated at 900 °C for 4 h in air. The solid black line in part (b) is the calculated pattern for the $X_{Ni} = 0.74$ film using Rietveld refinement. Reflections from $NiFe_2O_4$, NiO, and the Si substrate are noted.

3.3.2 Morphology of heat treated films

Evolution of film morphology after heat treatment can be understood from the SEM micrographs displayed in Figures 3.3(e)-(h). The 2-D nano-sheet structures of the $X_{Ni} = 0.26$ film have not changed significantly, but have broadened and coalesced with neighboring sheets. XRD data of the annealed films (Figure 3.4(b)) verify the existence of both spinel $NiFe_2O_4$ and rocksalt NiO for compositions of $X_{Ni} > 0.26$, with the relative intensity between NiO and $NiFe_2O_4$ peaks increasing with Ni content. The diffraction data of the $X_{Ni} = 0.26$ film show the evolution of the $NiFe_2O_4$ (220) reflection at ∼30.3°, but lack any indications of Fe_2O_3 or NiO. Table 3.1 presents film phase fraction data obtained via Rietveld refinement of the XRD scans, where stoichiometric $NiFe_2O_4$ and NiO were assumed. The X_{Ni} compositions determined with Rietveld agree well with XPS data, especially for high Ni content films, and carbon contamination in the films was < 1 at% (Figure 3.2(a)).

Heat-treating films with higher Ni content ($X_{Ni} > 0.26$) greatly altered the as-deposited morphology from columnar structures composed of small, spherical nanoparticles (∼5-10 nm) to columnar stacks composed of larger, faceted cuboids. TEM images and a selected area electron diffraction (SAED) pattern were taken of the $X_{Ni} = 0.74$ sample (Figure 3.5). The spot pattern can be indexed to reflections of spinel $NiFe_2O_4$ and rocksalt NiO

XPS	**EDX**	**XRD (Rietveld)**		
X_{Ni}	X_{Ni}	X_{Ni}	NiO mol fraction[a]	NiO vol fraction[a]
0.26	0.33	0.33	0	0
0.49	0.55	0.40	0.23	0.07
0.64	0.74	0.64	0.72	0.39
0.74	0.80	0.75	0.83	0.56

Table 3.1: Composition and phase fraction of NiO-$NiFe_2O_4$ films in Figure 3.3. [a]NiO mole and volume fractions are balanced by $NiFe_2O_4$.

from multiple grains, verifying that the film is a biphasic, polycrystalline material with 50-200 nm grain sizes. An energy dispersive x-ray spectroscopy (EDX) elemental map was also performed on the $X_{Ni} = 0.74$ film for further analysis of the local morphology and phase fractions (Figure 3.6). The length scale of porosity has clearly increased after heat treatment, as evidenced by infiltration of Pt (dark gray, from TEM sample preparation) deep into the film and larger voids (bright white). The EDX elemental map shows that nickel and oxygen are found everywhere in the film (excluding voids) with ∼50-100 nm iron-rich regions distributed throughout. Comparing the Fe and Ni maps, one can see that ∼ 50-100 nm $NiFe_2O_4$ crystals are dispersed in a matrix of larger ∼100-200 nm NiO grains.

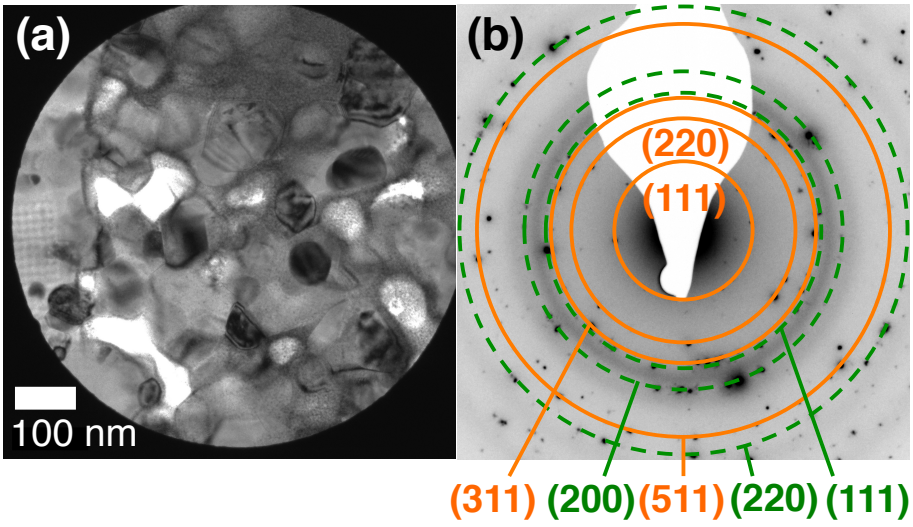

Figure 3.5: (a) Bright field TEM micrograph and (b) corresponding electron diffraction pattern of the annealed $X_{Ni} = 0.74$ film. The diffraction pattern clearly shows the presence of both $NiFe_2O_4$ (solid orange circles) and NiO (dashed green circles) in agreement with XRD data (Figure 3.4).

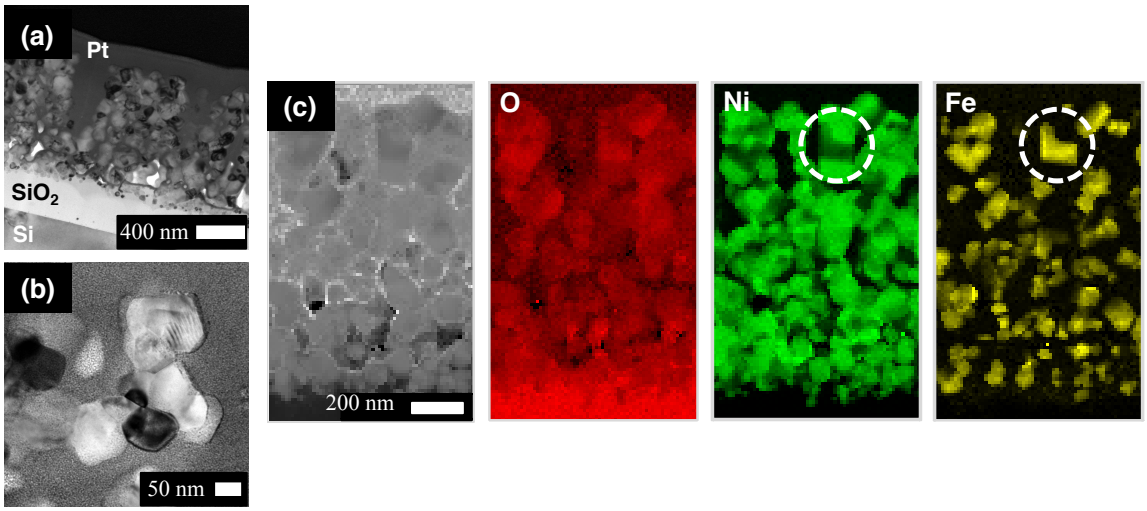

Figure 3.6: (a, b) Cross-sectional TEM images and (c) STEM HAADF image and EDX elemental maps of the heat-treated $X_{Ni} = 0.74$ film. The circled region in the Ni and Fe maps exemplify an Fe-rich area where Ni and O both occur, signifying the presence of the $NiFe_2O_4$ phase imbedded in NiO.

3.3.3 Magnetic measurements

M-H sweeps from -20 kOe to +20 kOe were measured at 20 K after both ZFC and FC (20 kOe) procedures for all films (Figures 3.7(a)-(d)). The ZFC M-H hysteresis loops (filled circles, black line) are symmetric about the origin in all cases, marking the absence of exchange bias. The coercivity (i.e., width of M-H loop), however, increases monotonically with Ni content. The increase in H_C from ~300 Oe for the NiO-absent film ($X_{Ni} = 0.26$) to ~520 Oe for the NiO rich film ($X_{Ni} = 0.74$) implies an exchange interaction at the interface between the $NiFe_2O_4$ and NiO phases where AFM spins are dragged with the FiM spins upon field reversal. The extra energy needed to create an irreversible twist in the AFM is macroscopically manifested as an increase in coercivity of the bare FiM.

The FC M-H loops in Figures 3.7(a)-(d) ('+' markers, red line) are shifted along the applied field axis for films containing NiO (i.e., $X_{Ni} > 0.26$). The FC procedure has enabled NiO spins to order into a low energy configuration that effectively pins the FiM

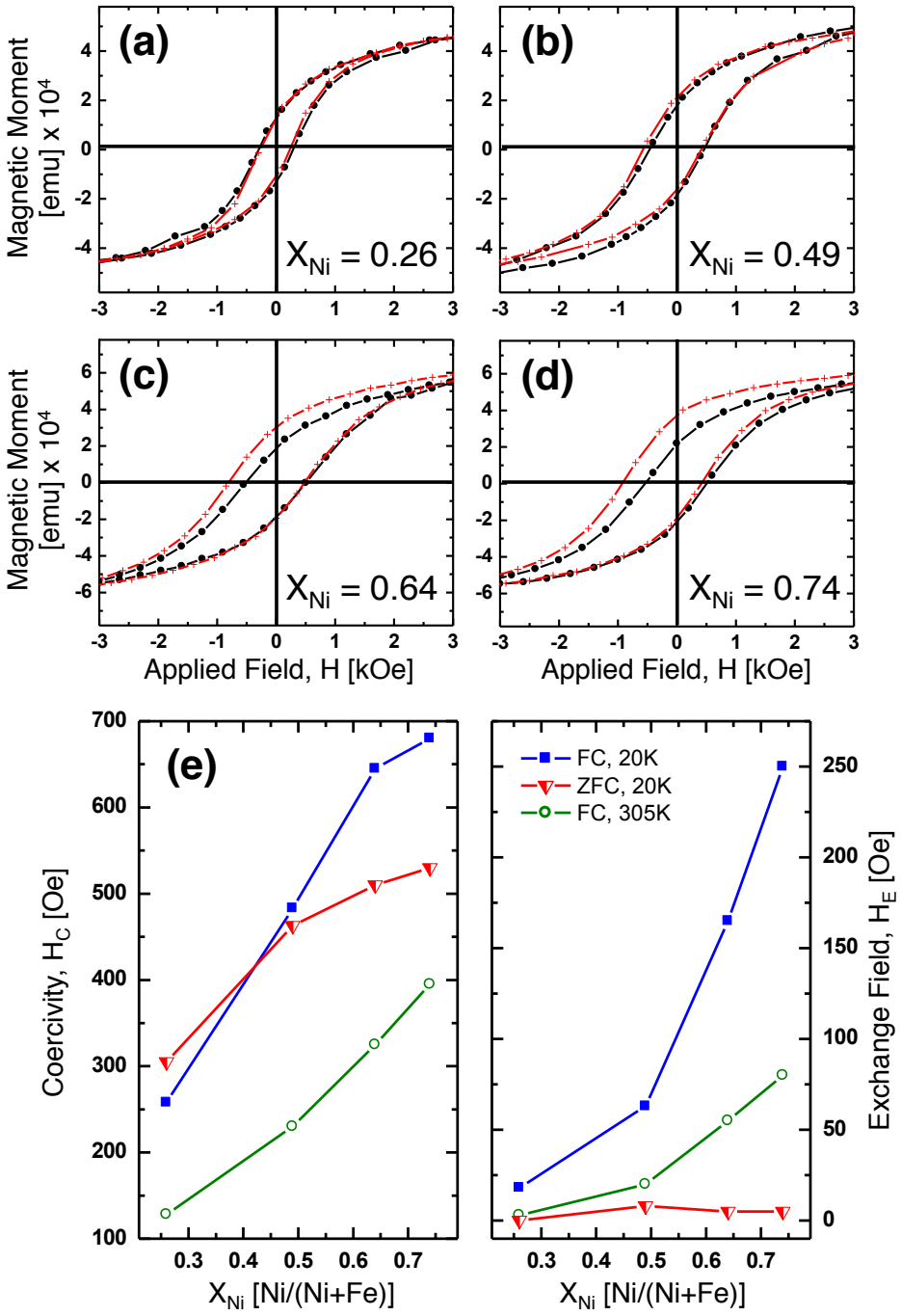

Figure 3.7: Zero field cooled (ZFC; black line, filled circles) and field cooled (FC; red line, '+') M-H loops measured at 20 K for $X_{Ni} = 0.26$ (a), 0.49 (b), 0.64 (c), and 0.74 (d). (e) H_E and H_C for different sample compositions; the FC and ZFC M-H loops were measured at 5 K and FC M-H loops were measured at 305 K.

moment along the field cooled direction. Only the left branch of the M-H loops widen after the FC procedure, while the right branch remains unchanged. This asymmetric behavior indicates that the two branches may be undergoing different mechanisms of spin reversal. Similar behavior has been seen elsewhere for Fe/NiO heterostructures [37], Co/CoO bilayers [38], and $NiFe_2O_4$/NiO fine-particle systems [30, 39] where coherent spin rotation was observed for the right branch, and domain wall nucleation and propagation was observed for the left branch. The loop shift increases with NiO content for the range of compositions studied, with the $X_{Ni} = 0.74$ film exhibiting the largest shift (H_E ~250 Oe). It is known that EB properties are strongly dependent on the interfacial density between the FM/AFM, which may explain the difference in H_E for the morphologically similar $X_{Ni} = 0.64$ and 0.74 films (see Figures 3.3(g)-(h)). The higher Fe content of the $X_{Ni} = 0.64$ film may have led to formation of larger $NiFe_2O_4$ particles during annealing, effectively reducing the number of interfacial pinning sites compared to the $X_{Ni} = 0.74$ film. Moreover, an increase in hysteresis loop squareness, M_R/M_S, was observed for all films exhibiting exchange bias (i.e., $X_{Ni} > 0.26$). The M_R/M_S values for the FC M-H loops measured at 20 K were 0.22, 0.36, 0.42, and 0.56 for the $X_{Ni} = 0.26$, 0.49, 0.64 and 0.74 films, respectively.

Figure 3.7(e) compares H_E and H_C as a function of film composition for the ZFC M-H loops recorded at 20 K and the FC M-H loops recorded at 20 K and 305 K. H_E and H_C increase with Ni composition in all cases, except for the ZFC curves, where H_E is negligible for all compositions. H_E as high as ~80 Oe was observed at 305 K for the $X_{Ni} = 0.74$ film, which compares well with $NiFe_2O_4$/NiO bilayers, where H_E of ~100 Oe at 300 K has been reported [40]. Nanogranular nickel oxide-ferrite systems synthesized via co-precipitation have not demonstrated exchange bias above ~250 K due to exchange coupling between $NiFe_2O_4$ nanoparticles and a spin glass phase that formed at the disordered $NiFe_2O_4$/NiO interface [15, 41]. Additional M-H loops measured at

5 K, after being field-cooled from 400 K, showed H_C enhancement but no H_E. This suggests that exchange coupling between $NiFe_2O_4$ and a spin glass phase, which can act as the AFM with a blocking temperature far below room temperature, is not responsible for the exchange bias observed in this work. The absence of a large vertical shift in the hysteresis curve [15, 39], and unsaturated and open M-H loops at high fields [42, 43] further reinforce this conclusion.

The values measured in this work at 20 K (H_E ~250 Oe and H_C ~680 Oe) are lower than those measured in the co-precipitated $NiFe_2O_4$/NiO nanogranular system (H_E ~2.2 kOe and H_C ~2.9 kOe at 10 K) [15]. A direct comparison between these two works is difficult because of the different interfacial exchange coupling mechanism at play, grain size and composition, and interfacial density. As mentioned earlier, the exchange bias effect in the co-precipitated $NiFe_2O_4$/NiO system occurs due to exchange coupling between $NiFe_2O_4$ and a spin glass phase, where the pinning strength of the spin glass may be higher than NiO, resulting in larger EB. Additionally, the phase composition in the co-precipitated system was 5 mol% $NiFe_2O_4$ balanced by NiO, whereas, all films studied here are $>$ 17 mol% $NiFe_2O_4$. Moreover, the size distribution of the precipitated FiM $NiFe_2O_4$ nanoparticles was narrow and centered at ~8 nm [15], much smaller than the ~50-100 nm $NiFe_2O_4$ grains seen here. In general, EB scales inversely with FiM particle size due to a concomitant increase in the interfacial exchange energy and decrease in the magnetic anisotropy of the FiM; this trend has been observed in $NiFe_2O_4$/NiO when the FiM size is $<$ 55 nm [41]. As such, microplasma-deposited materials should show large increases in EB if particle sizes can be decreased. Finally, the annealed films in this work are highly porous, leading to many $NiFe_2O_4$ 'free surfaces' where FiM spins would not be pinned by a nearby AFM phase, resulting in weaker EB. Increasing film density will no doubt increase EB even further for microplasma-deposited films.

3.4 Conclusions

In this chapter, we demonstrated the ability to synthesize thin, nanostructured $NiFe_2O_4$ and NiO films with varying composition and morphology using high-pressure microplasma jets. A directed flux of nickel and iron growth species were created via electron impact dissociation of organometallic precursors in an oxidizing environment. Film nucleation and growth was characteristic of ballistic aggregation phenomena, where high growth flux and low adatom mobility are prevalent. After heat treatment of the as-deposited films, exchange bias effects were observed at both low and room temperature for films with compositions $X_{Ni} > 0.26$. H_E and H_C increased with NiO content and may be explained by an increase in interfacial densities between the $NiFe_2O_4$ and NiO phases. For FC M-H loops measured at 20 K, the highest H_E (∼250 Oe) and H_C (∼700 Oe) were observed for the $X_{Ni} = 0.74$ film. Exchange bias effects persisted at high temperatures (305 K) where the measured H_E ∼80 Oe and H_C ∼400 Oe are comparable to reported values for $NiFe_2O_4$/NiO bilayers. The relatively high values measured at both low and high temperatures are encouraging considering the high porosity of the films. Exchange bias phenomena are directly dependent on interfacial density; as such, future work will focus on varying microplasma operating parameters (e.g., scanning speed, precursor flux, and substrate temperature) as well as post-deposition heat treatments to increase film density, and enhance exchange bias. Then, a more systematic study of FiM/AFM particle size and phase fraction can ensue. Finally, this work shows that microplasmas are an interesting and versatile route to synthesize a variety of nanoscale, biphasic materials to investigate exchange bias and magnetic hardening phenomena.

References

[1] T. Seto, H. Akinaga, F. Takano, K. Koga, T. Orii, and M. Hirasawa, "Magnetic properties of monodispersed Ni/NiO core-shell nanoparticles," *J. Phys. Chem. B*, vol. 109, no. 28, pp. 13403–13405, 2005.

[2] G. Ennas, A. Falqui, S. Marras, C. Sangregorio, and G. Marongiu, "Influence of metal content on size, dispersion, and magnetic properties of iron-cobalt alloy nanoparticles embedded in silica matrix," *Chem. Mater.*, vol. 16, no. 26, pp. 5659–5663, 2004.

[3] J. Greiner, I. Croll, and M. Sulich, "Ferromagnetic-antiferromagnetic interaction in Fe-FeS," *J. Appl. Phys.*, vol. 31, no. 12, pp. 2316–2317, 1960.

[4] H.-M. Lin, C. Hsu, Y. Yao, Y. Cben, T. Kuan, F. Yang, and C. Tung, "Magnetic study of both nitrided and oxidized Co particles," *Nanostruct. Mater.*, vol. 6, no. 5, pp. 977–980, 1995.

[5] W. H. Meiklejohn and C. P. Bean, "New magnetic anisotropy," *Phys. Rev.*, vol. 102, no. 5, p. 1413, 1956.

[6] C. Prados, M. Multigner, A. Hernando, J. Sanchez, A. Fernandez, C. Conde, and A. Conde, "Dependence of exchange anisotropy and coercivity on the Fe–oxide structure in oxygen-passivated Fe nanoparticles," *J. Appl. Phys.*, vol. 85, no. 8, pp. 6118–6120, 1999.

[7] L. T. Kuhn, A. Bojesen, L. Timmermann, K. Fauth, E. Goering, E. Johnson, M. M. Nielsen, and S. Mørup, "Core-shell iron–iron oxide nanoparticles: Magnetic properties and interactions," *J. Magn. Magn. Mater.*, vol. 272, pp. 1485–1486, 2004.

[8] T. Miyahara and K. Kawakami, "Fine iron particles having super high coercivity," *IEEE Trans. Magn.*, vol. 23, no. 5, pp. 2877–2879, 1987.

[9] J. Sort, J. Nogués, X. Amils, S. Suriñach, J. Munoz, and M. Baró, "Room-temperature coercivity enhancement in mechanically alloyed antiferromagnetic-ferromagnetic powders," *Appl. Phys. Lett.*, vol. 75, no. 20, pp. 3177–3179, 1999.

[10] L. Del Bianco, F. Boscherini, M. Tamisari, F. Spizzo, M. V. Antisari, and E. Piscopiello, "Exchange bias and interface structure in the Ni/NiO nanogranular system," *J. Phys. D: Appl. Phys.*, vol. 41, no. 13, p. 134008, 2008.

[11] S. Doppiu, V. Langlais, J. Sort, S. Suriñach, M. Baro, Y. Zhang, G. Hadjipanayis, and J. Nogués, "Controlled reduction of NiO using reactive ball milling under hydrogen atmosphere leading to Ni-NiO nanocomposites," *Chem. Mater.*, vol. 16, no. 26, pp. 5664–5669, 2004.

[12] S. Mishra, I. Dubenko, J. Losby, S. Roy, N. Ali, and K. Marasinghe, "Magnetic behavior of mechanically milled FeNi-CoO nanocomposites," *IEEE Trans. Magn.*, vol. 40, no. 4, pp. 2716–2720, 2004.

[13] V. Skumryev, S. Stoyanov, Y. Zhang, G. Hadjipanayis, D. Givord, and J. Nogués, "Beating the superparamagnetic limit with exchange bias," *Nature*, vol. 423, no. 6942, pp. 850–853, 2003.

[14] M. Artus, S. Ammar, L. Sicard, J.-Y. Piquemal, F. Herbst, M.-J. Vaulay, F. Fiévet, and V. Richard, "Synthesis and magnetic properties of ferrimagnetic $CoFe_2O_4$ nanoparticles embedded in an antiferromagnetic NiO matrix," *Chem. Mater.*, vol. 20, no. 15, pp. 4861–4872, 2008.

[15] Z. Tian, S. Yuan, S. Yin, L. Liu, J. He, H. Duan, P. Li, and C. Wang, "Exchange bias effect in a granular system of $NiFe_2O_4$ nanoparticles embedded in an antiferromagnetic NiO matrix," *Appl. Phys. Lett.*, vol. 93, no. 22, p. 222505, 2008.

[16] B. D. Cullity and C. D. Graham, *Introduction to magnetic materials, 2nd ed.* Hoboken, NJ: John Wiley & Sons, Inc., 2009.

[17] T. L. Koh, E. C. O'Hara, and M. J. Gordon, "Microplasma-based synthesis of vertically aligned metal oxide nanostructures," *Nanotechnology*, vol. 23, no. 42, p. 425603, 2012.

[18] R. M. Sankaran, D. Holunga, R. C. Flagan, and K. P. Giapis, "Synthesis of blue luminescent Si nanoparticles using atmospheric-pressure microdischarges," *Nano Lett.*, vol. 5, no. 3, pp. 537–541, 2005.

[19] R. M. Sankaran and K. P. Giapis, "Hollow cathode sustained plasma microjets: Characterization and application to diamond deposition," *J. Appl. Phys.*, vol. 92, no. 5, pp. 2406–2411, 2002.

[20] W.-H. Chiang and R. M. Sankaran, "Linking catalyst composition to chirality distributions of as-grown single-walled carbon nanotubes by tuning Ni_xFe_{1-x} nanoparticles," *Nat. Mater.*, vol. 8, no. 11, pp. 882–886, 2009.

[21] T. L. Koh and M. J. Gordon, "Spray deposition of nanostructured metal films using hydrodynamically stabilized, high pressure microplasmas," *J. Vac. Sci. Technol. A*, vol. 31, no. 6, p. 061312, 2013.

[22] T. Koh, E. O'Hara, and M. Gordon, "Growth of nanostructured CuO thin films via microplasma-assisted, reactive chemical vapor deposition at high pressures," *J. Cryst. Growth*, vol. 363, pp. 69–75, 2013.

[23] T. Koh, I. Chiles, and M. Gordon, "Slit-based supersonic microplasma jets: Scalable sources for nanostructured thin film deposition," *Appl. Phys. Lett.*, vol. 103, no. 16, p. 163115, 2013.

[24] D. Mariotti, H. Lindström, A. C. Bose, and K. K. Ostrikov, "Monoclinic β-MoO_3 nanosheets produced by atmospheric microplasma: application to lithium-ion batteries," *Nanotechnology*, vol. 19, no. 49, p. 495302, 2008.

[25] F. E. Kruis, H. Fissan, and A. Peled, "Synthesis of nanoparticles in the gas phase for electronic, optical and magnetic applications—a review," *J. Aerosol Sci.*, vol. 29, no. 5, pp. 511–535, 1998.

[26] D. Mariotti and R. M. Sankaran, "Microplasmas for nanomaterials synthesis," *J. Phys. D: Appl. Phys.*, vol. 43, no. 32, p. 323001, 2010.

[27] D. Mariotti and R. M. Sankaran, "Perspectives on atmospheric-pressure plasmas for nanofabrication," *J. Phys. D: Appl. Phys.*, vol. 44, no. 17, p. 174023, 2011.

[28] M. Rhamdhani, P. Hayes, and E. Jak, "Subsolidus phase equilibria of the Fe-Ni-O system," *Metall. Mater. Trans. B*, vol. 39, no. 5, pp. 690–701, 2008.

[29] T. Koh and M. Gordon, "Thin-film deposition with high pressure capillary microdischarges under different supersonic flow and shock regimes," *J. Phys. D: Appl. Phys.*, vol. 46, no. 49, p. 495204, 2013.

[30] Z. Tian, S. Yuan, L. Liu, S. Yin, L. Jia, P. Li, S. Huo, and J. Li, "Exchange bias training effect in $NiFe_2O_4$/NiO nanocomposites," *J. Phys. D: Appl. Phys.*, vol. 42, no. 3, p. 035008, 2009.

[31] P. Hartman, "The effect of surface relaxation on crystal habit: cases of corundum (α-Al_2O_3) and hematite (α-Fe_2O_3)," *J. Cryst. Growth*, vol. 96, no. 3, pp. 667–672, 1989.

[32] I. Sunagawa, *Crystals: Growth, morphology, & perfection*. Cambridge, U.K.: Cambridge University Press, 2005.

[33] J. Gunjakar, A. More, K. Gurav, and C. Lokhande, "Chemical synthesis of spinel nickel ferrite ($NiFe_2O_4$) nano-sheets," *Appl. Surf. Sci.*, vol. 254, no. 18, pp. 5844–5848, 2008.

[34] D. Bensimon, B. Shraiman, and S. Liang, "On the ballistic model of aggregation," *Phys. Lett. A*, vol. 102, no. 5, pp. 238–240, 1984.

[35] P. Ramanlal and L. Sander, "Theory of ballistic aggregation," *Phys. Rev. Lett.*, vol. 54, no. 16, p. 1828, 1985.

[36] D.-X. Ye and T.-M. Lu, "Fanlike aggregations on seeds by parallel ballistic flux: Experimental results and monte carlo simulations of the growth of three-dimensional Si structures," *Phys. Rev. B*, vol. 75, no. 11, p. 115420, 2007.

[37] A. Hochstrat, C. Binek, and W. Kleemann, "Training of the exchange-bias effect in NiO-Fe heterostructures," *Phys. Rev. B*, vol. 66, no. 9, p. 092409, 2002.

[38] F. Radu, M. Etzkorn, T. Schmitte, R. Siebrecht, A. Schreyer, K. Westerholt, and H. Zabel, "Asymmetric magnetization reversal on exchange biased CoO/Co bilayers," *J. Magn. Magn. Mater.*, vol. 240, no. 1, pp. 251–253, 2002.

[39] Z. Tian, J. Chen, S. Yuan, Y. Zhang, Z. Ma, H. Duan, and C. Lu, "Cooling field and temperature dependence on training effect in $NiFe_2O_4$-NiO nanogranular system," *J. Appl. Phys.*, vol. 110, no. 10, p. 103902, 2011.

[40] B. Negulescu, L. Thomas, Y. Dumont, M. Tessier, N. Keller, and M. Guyot, "Exchange biasing in NiO/$NiFe_2O_4$ bilayers," *J. Magn. Magn. Mater.*, vol. 242, pp. 529–531, 2002.

[41] Z. Tian, S. Huang, Y. Qiu, S. Yuan, Y. Wu, and L. Li, "Size-dependent scaling of exchange bias in $NiFe_2O_4$/NiO nanogranular systems synthesized by a phase separation method," *J. Appl. Phys.*, vol. 113, no. 14, p. 143906, 2013.

[42] R. H. Kodama, A. E. Berkowitz, E. McNiff Jr, and S. Foner, "Surface spin disorder in $NiFe_2O_4$ nanoparticles," *Phys. Rev. Lett.*, vol. 77, no. 2, p. 394, 1996.

[43] Y.-k. Tang, Y. Sun, and Z.-h. Cheng, "Exchange bias associated with phase separation in the perovskite cobaltite $La_{1-x}Sr_xCoO_3$," *Phys. Rev. B*, vol. 73, no. 17, p. 174419, 2006.

Chapter 4

Exchange bias and spin glass behavior in biphasic $NiFe_2O_4$/NiO thin films

This chapter has been adapted from: A. C. Pebley, P. E. Fuks, T. M. Pollock, and M. J. Gordon, "Exchange bias and spin glass behavior in biphasic $NiFe_2O_4$/NiO thin films," *J. Magn. Magn. Mater.*, vol. 419, p. 29, 2016.

4.1 Introduction

Promising EB results have been obtained with FiM nanoparticles dispersed in an AFM matrix, where the connectivity (continuity) of the AFM phase has been shown to enhance exchange coupling at FiM/AFM interfaces [1–4]. The strength of this coupling is quite complex and has been shown to depend on several variables, including particle size, chemical intermixing, and interfacial strain, contact and structure. Moreover, the situation becomes more complicated if a spin glass-like (SG) phase is present, which is

often the case in nanoparticle or nanogranular EB systems synthesized by mechanical [5, 6] (ball milling) or wet-chemical methods [7, 8]. In these cases, spin disorder in the spin glass phase can couple to the reversible phase at low temperatures, yielding EB and anomalous vertical shifts of hysteresis loops. Generally speaking, formation of the SG phase is due to atomic rearrangement at surfaces, or from finite size effects where the increase in surface/volume ratio induces structural disorder at the particle surface. For example, the EB effect has been seen separately in oxide spinels (e.g., $NiFe_2O_4$ [9, 10] and $CoCr_2O_4$ [11]) and AFM (e.g., NiO [12]) nanoparticles where the structural disorder at the surface leads to the formation of random, non-collinear surface spins, which either couple to or change the magnetic order of the particle at low temperatures. Although the EB effect is rather profound in SG systems, the effect does not persist up to room temperature, making these systems undesirable for data storage. As such, it is of great technological interest to find new approaches to engineer the magnetic behavior of nanogranular EB systems.

This chapter further investigates how high-pressure microplasma (MP) jets can be used [13–21] to synthesize nanogranular EB films and how annealing influences morphology, structure, and exchange bias coupling characteristics. Specifically, biphasic $NiFe_2O_4$/NiO films, deposited at 175 °C using MPs, were annealed at 400, 500, 600, and 850 °C, and were studied under field cooled (FC) and zero field cooled (ZFC) conditions. Results showed that exchange bias (H_{EB}) in as-deposited and low temperature annealed films ($\leq$ 600 °C) was due to exchange coupling involving a structurally disordered spin glass (SG) phase, while at higher temperatures (850 °C), H_{EB} appears to originate from direct coupling between $NiFe_2O_4$ and NiO crystalline phases.

4.2 Experimental Procedure

4.2.1 Microplasma deposition

Nanogranular $NiFe_2O_4$/NiO thin films were spray deposited onto 300 nm thick SiO_2 layers on (100) Si substrates using the DC microplasma (MP) deposition system shown in Figure 2.4. Organometallic precursors (nickelocene, $Ni(Cp)_2$, and ferrocene, $Fe(Cp)_2$; STREM) were sublimed in separate temperature-controlled cells (T_{cell} = 25 °C), mixed with 9:1 Ar:O_2 gas flow and delivered to the hollow-cathode discharge (I = 8 mA, V = –500 V) with a total flow rate of 200 sccm. Nickel-iron oxide nanoparticles/clusters formed in the hollow-cathode region of the plasma were spray-deposited onto SiO_2/Si substrates at 175 °C; the substrate was raster-scanned in a serpentine fashion at 0.3 mm/s underneath the jet to create large area films (∼cm^2). Argon makeup gas (100 sccm) was also introduced into the chamber background, and the chamber was regulated at 20 Torr for the duration of the experiment. After deposition, the large area $NiFe_2O_4$/NiO film (X_{Ni} = 0.76, metals basis) was cut into multiple pieces, with each piece separately heat-treated at 400, 500, 600, or 850 °C for 4 hours in air. The samples obtained are denoted as AsDep, S400, S500, S600, and S850, respectively.

4.2.2 Materials Characterization

Film morphology and atomic composition (i.e., X_{Ni}, metals basis) was analyzed using an FEI XL30 SEM equipped with an EDX detector. A PANalytical Empyrean X-ray diffractometer (Cu Kα radiation) was used to obtain ω-2θ scans, with a -4° offset to suppress the (004) Si peak of the underlying substrate at ∼69° 2θ. Rietveld refinement of the resulting XRD spectra in the 33-40° 2θ range was performed using HighScore Plus software to calculate $NiFe_2O_4$/NiO phase fractions and grain sizes from the (311)

$NiFe_2O_4$ and (111) NiO reflections. Because the x-ray beam length is a function of 2θ and the films are substantially thinner (∼400 nm) than the penetration depth of the x-ray source (> 10 μm), the volume of material irradiated changes with 2θ, and phase fractions cannot be obtained. As such, the narrow 2θ region for Rietveld analysis was carefully chosen to estimate the $NiFe_2O_4$ and NiO phase fractions from the (311) $NiFe_2O_4$ and (111) NiO peaks at ∼36 and 37.6°, respectively, which are close enough in 2θ to maintain the constant irradiated volume approximation. This analysis would break down if the films had a preferred orientation; however, the (111):(200) NiO and (220):(311) $NiFe_2O_4$ peak ratios of 0.61 and 0.30 (JCPDS file nos. 00-047-1049 and 01-086-2267), respectively, obtained using grazing-incidence XRD on a Rigaku diffractometer, suggest the films were indeed randomly oriented. The Scherrer equation [22] was used for grain size calculation after calibrating the diffractometer with a sintered alumina plate standard (SRM 1976a; NIST) to account for instrument broadening and measurement geometry.

A Quantum Design MPMS 5XL SQUID magnetometer was used to characterize the temperature and field-dependent magnetic behaviors of the films. Specifically, field cooled (FC) and zero field cooled (ZFC) M-T curves were measured in a 20 kOe field from 300 to 5 K. Hysteresis loops were measured across a range of temperatures between 300 and 5 K, where each measurement was preceded by field cooling in a 20 kOe field from 300 K to suppress the training effect [23]. ZFC hysteresis loops were also measured at 5 K.

4.3 Results and Discussion

4.3.1 Morphology and Structure

XRD spectra for the as-deposited and annealed samples are shown in Figure 4.1(a). All samples have reflections that can be indexed to both rocksalt NiO (Fm3m) and inverse

spinel $NiFe_2O_4$ (Fd-3m), confirming their biphasic nature. The broad hump centered at $\sim 69^\circ$ 2θ is due to the underlying Si substrate and measurement geometry. The data suggest a substantial change in the $NiFe_2O_4$/NiO phase distribution with annealing, as can be seen from the ratio between the (311) $NiFe_2O_4$ and (111) NiO intensities (Figure 4.1(b)). The phase fraction and grain size of the $NiFe_2O_4$ and NiO phases were extracted using Rietveld refinement analysis (fits are represented as the bold black lines in Figure 4.1(b)) and are summarized in Figures 4.1(c) and (d), respectively. The phase fraction for the AsDep film was estimated at 28/72 mol% $NiFe_2O_4$/NiO, which deviates from the expected value [24] of 16/84 mol% for the $NiFe_2O_4$/NiO system with a composition of $X_{Ni} = 0.76$ (metals basis, balanced by Fe). Based on the x-ray data, we hypothesize that this modest discrepancy may be due to the formation of Ni-rich amorphous regions during deposition, resulting in an 'observed' enrichment of $NiFe_2O_4$ compared to NiO in the film. Nonetheless, we would still expect the relative phase fraction of NiO to be much larger than $NiFe_2O_4$, given the high Ni composition and the varying complexities of the two structures. That is, generally speaking, metal cations can more easily diffuse into the interstitial sites of the simple rocksalt structure of NiO (i.e., FCC packing of O^{2-} anions with the Ni^{2+} cations occupying the octahedral interstitial sites) than for the more complex inverse spinel [25] structure of $NiFe_2O_4$ (i.e., FCC packing of O^{2-} anions with all the Ni^{2+} and half of the Fe^{3+} cations situated in octahedral interstitial sites, and the remaining Fe^{3+} ions located in the tetrahedral sites).

The relative phase fraction changes substantially from 28/72 to 9/91 mol% $NiFe_2O_4$/ NiO after annealing at 400 °C for 4 hours. The data imply that the aforementioned Ni-rich amorphous regions are crystallizing into NiO and $NiFe_2O_4$, with NiO forming at a more rapid rate due to the simplicity of the rocksalt structure compared to spinel. As the annealing temperature increases, there is a concomitant increase in the rate of crystallization and we observe an increase in the relative amount of $NiFe_2O_4$ to NiO com-

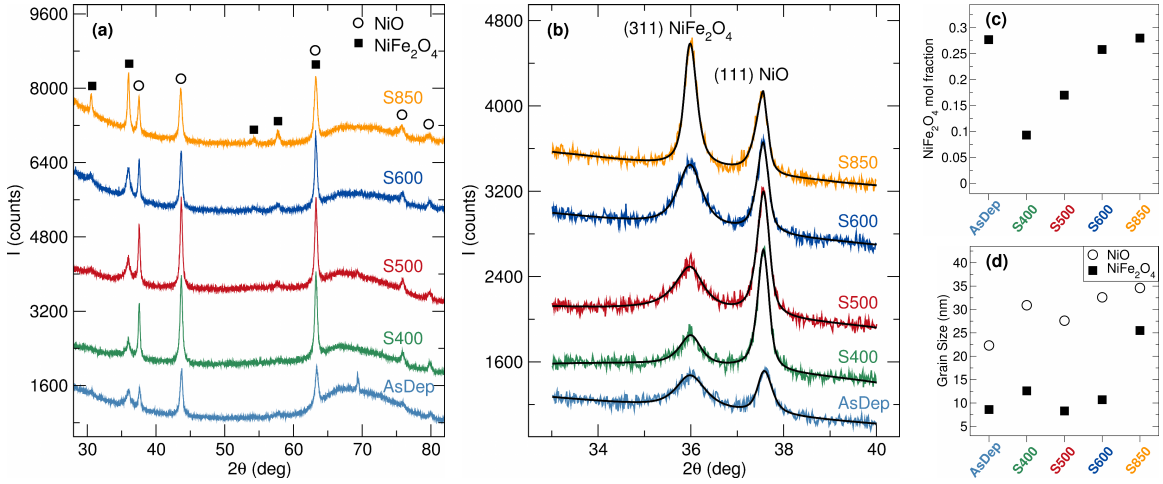

Figure 4.1: (a) X-ray diffraction spectra of as-deposited and annealed $NiFe_2O_4$/NiO films measured using Bragg–Brentano geometry with a -4° offset. (b) Overlay of raw x-ray data and the corresponding Rietveld refinement fits (black lines) in the 33–40° 2θ range. (c) $NiFe_2O_4$ mole fraction (balanced by NiO), and (d) NiO and $NiFe_2O_4$ grain sizes obtained from Rietveld refinement of data presented in panel (b). AsDep, S400, S500, S600, and S850 refer to samples deposited at 175 °C (AsDep) and subsequently annealed at 400, 500, 600, and 850 °C for 4 h in air, respectively.

pared to the S400 sample (Figure 4.1(c)). This result may be interpreted in a multistep process: (i) in the early stages of heat treatment, Ni-rich amorphous regions crystallize to preferentially form NiO, and (ii) as crystallization proceeds, the amorphous regions become progressively more Fe-rich with the $NiFe_2O_4$ phase forming more rapidly than NiO at later times during annealing, leading to a relative increase in the $NiFe_2O_4$ phase.

Plan and cross-sectional SEM micrographs for the AsDep sample indicate that the film is comprised of dense columnar structures where each individual column is composed of a fine distribution of particles that are < 50 nm (Figures 4.2(a) and (b)). We hypothesize that during the initial stages of thin film growth, a directed flux of activated species (e.g., Ar, Ni, Fe and O), clusters and/or nanoparticles of nickel-iron oxides impinge on the substrate surface, resulting in the nucleation and growth of small, randomly oriented oxide fibrils (∼5-10 nm). The evolution of these fibrils into tapered polycrystalline columns with faceted tops is characteristic of frequent renucleation and diffusion-driven growth

where the incoming adatoms and/or nanoparticles from the gas phase deposit onto the growing film and locally rearrange along surfaces and grain boundaries to form crystalline phases. Interestingly, the as-deposited morphology appears to remain unchanged after annealing up to 600 °C (Figure 4.2(c)). However, after annealing at 850 °C, $NiFe_2O_4$ and NiO grains appear to sinter, as seen in Figure 4.2(d). The $NiFe_2O_4$ and NiO grain sizes were obtained from the (311) $NiFe_2O_4$ and (111) NiO reflections using the Scherrer equation [22]. As shown in Figure 4.2(d), the $NiFe_2O_4$ grain size remained relatively constant at ∼8-10 nm; however, at 850 °C, grain size increased substantially to 26 nm, in agreement with SEM. Conversely, the average grain size of NiO increased monotonically with anneal temperature from 22 nm for the AsDep sample to 35 nm for the S850 sample.

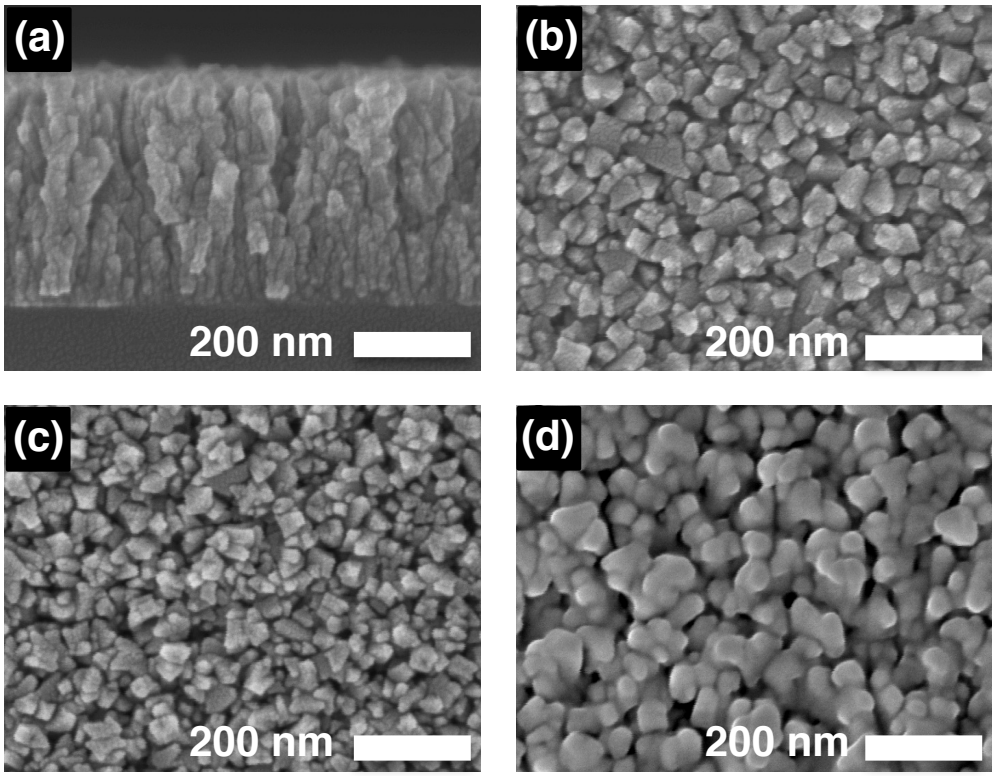

Figure 4.2: Cross-sectional and plan SEM images of as-deposited and annealed (600–850 °C, 4 h in air) $NiFe_2O_4$/NiO films grown via microplasma at 20 Torr: (a) cross-sectional view of the AsDep film, and plan views of the (b) AsDep, (c) S600, and (d) S850 films.

4.3.2 Growth Mechanism

Although a detailed study of microplasma growth dynamics is outside the scope of the present study, it is highly likely that 'activated' Ni and Fe species (e.g., ions, neutrals, etc.) formed in the hollow cathode region of the jet result in the formation of aerosolized clusters and/or small nanoparticles that are ultimately spray deposited on the substrate. Evidence for this stems from previous work with microplasmas operating at higher pressures (100's of Torr), where aerosolized nanoparticles in the 2-10 nm size range can be formed [14, 20]. Although pressures are lower in our case, it is still very likely that small clusters do form in the jet because gas phase collision frequencies are very high ($\sim 10^{10}$ – 10^{11} s^{-1}) at 20 Torr. Also, given that O_2 injected in the jet or chamber background results in oxide species and films would suggest that Ni/Fe species and/or aerosolized clusters/nanoparticles could react with active oxygen species both enroute to and at the substrate surface. Bombardment of the surface by charged species, which could enhance surface diffusion, may also assist in the formation of crystalline films at such low substrate temperatures [26]. Systematic studies are currently underway to investigate the importance of these underlying effects, i.e., deconvoluting the role of gas-phase nucleation/growth versus surface diffusion-mediated processes, charged particle bombardment of the substrate, and determining the fundamental 'species' (e.g., ions/atoms, clusters, or nanoparticles) responsible for film growth at various pressures.

4.3.3 Magnetic measurements

A magnetic hysteresis curve of the AsDep sample was obtained at 5 K after field cooling from 300 K in a 20 kOe field (Figure 4.3). The salient features of the M-H curve are the apparent negative shift of the hysteresis curve along the applied field axis, which is suggestive of the EB effect (H_{EB}), and the large vertical shift of the loop (i.e., |M(+20

kOe)| $\neq$ |M(-20 kOe)|) in the field cool direction, where ΔM is twice the shift, as defined in Figure 4.3. The EB effect corresponding to an exchange interaction between crystalline $NiFe_2O_4$ and NiO is only expected to appear if the sample is field cooled through the Néel temperature of NiO (T_N ~525 K). In the present case however, EB was observed after the sample was field cooled through a much lower temperature of 300 K, and it is rather large (H_{EB} = 2 kOe), suggesting that another magnetic phase is coupling to the reversible spins of $NiFe_2O_4$. Furthermore, the openness of the M-H loop and the unsaturated behavior at relatively high fields of 20 kOe are characteristic of coupling from a spin disordered or spin glass (SG)-like phase [27]. It is well known that the surface layers of ferrites, when confined to the nanoscale, show SG behavior at low temperatures due to finite size effects and/or structural disorder at the surface [9, 10]. Notwithstanding, we cannot discard the possibility that some portion of the large vertical and horizontal shifts may be attributed to minor loop effects that arise when the magnetic sample is not sufficiently saturated during the measurement (see discussion below) [12].

The FC and ZFC M-H loops measured at 5 K for samples annealed at different temperatures are displayed in Figure 4.4. The important features to note are: (i) the ZFC curves are symmetric and centered about the origin (i.e., H_{EB} = ΔM = 0), (ii) enhancement of coercivity (H_C) and the appearance of a horizontal shift (H_{EB}) of the M-H loops after FC, (iii) presence of a small vertical shift of the hysteresis loop after FC for all but the S850 sample, (iv) significantly larger magnetic moments at higher fields compared to the AsDep film, which attests to the crystallization of $NiFe_2O_4$ from amorphous regions in the film, and finally (v) only the left branches of hysteresis curves widen after FC, indicating that exchange coupling only influences moment reversal in the negative field direction.

It has recently been demonstrated [28], and mentioned elsewhere [12, 29–31], that the same characteristics invariably associated with exchange bias (e.g., observations i, ii,

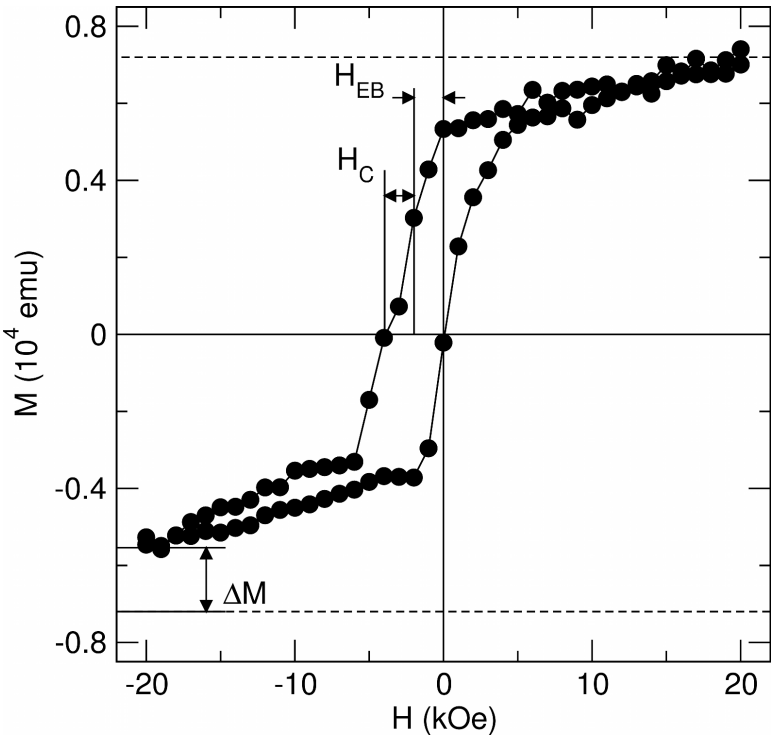

Figure 4.3: Magnetic hysteresis loop of the $NiFe_2O_4$/NiO AsDep film measured at 5 K after field cooling in a 20 kOe field from 300 K.

and iii above), can also be consequences of minor loop phenomena, which manifest when the range of fields used in an M-H measurement are insufficient to effectively saturate the ferro- or ferrimagnetic phase. As such, it is imperative when studying exchange bias, or any other magnetic phenomenon that requires evaluation of magnetization curve parameters, to ensure formation of a major loop to unequivocally rule out minor loop effects. As proposed by Harres *et al.* [28], one method to identify a major vs. minor loop is to analyze the derivatives of both the descending and ascending branches of the hysteresis loop. If the derivatives of these branches coincide and overlap before the maximum field value of the measurement is obtained, then moment reversal has become a reversible process, and magnetic saturation achieved. This analysis was performed on the hysteresis loops shown in the insets of Figure 4.4, confirming that the curves are major, and that the horizontal and vertical shifts in the hysteresis loops are in fact due

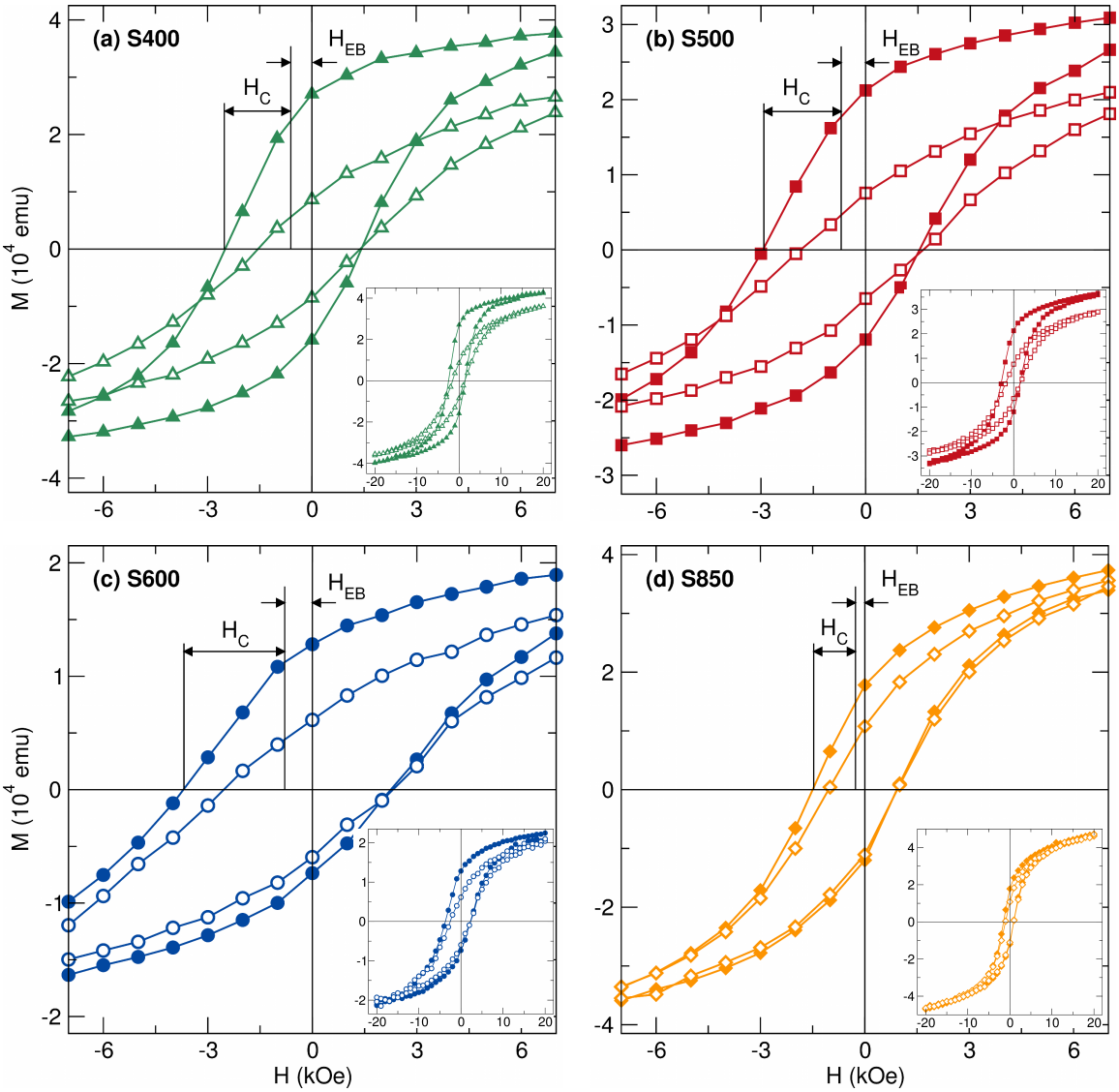

Figure 4.4: Magnetic hysteresis loops measured at 5 K after ZFC (open symbols) and after FC in a 20 kOe field (closed symbols) from 300 K for the (a) S400, (b) S500, (c) S600, and (d) S850 $NiFe_2O_4$/NiO annealed films. Insets show hysteresis curves over the full ± 20 kOe field range

to exchange coupling (Figure 4.5). The analysis was inconclusive for the as-deposited sample (Figure 4.3) because of the low signal-to-noise ratio of the measurement, which can be attributed to relatively low magnetization from high structural disorder in the sample (i.e., when comparing the magnitude of magnetization between the AsDep and annealed samples in Figures 4.3 and 4.4, respectively). Because exchange bias persists

in the annealed samples, and minor loop effects are ruled out, it is reasonable to assume that exchange bias is likely responsible for the loop shifts in the as-deposited sample as well.

The existence of a horizontal shift after FC through a temperature (300 K) less than T_N (525 K) suggests that the T_N of NiO has been suppressed below 300 K due to finite size effects and/or there is an exchange interaction other than that between $NiFe_2O_4$/NiO. The EB phenomenon requires two exchange-coupled phases where one phase has a reversible magnetic moment and the other is fixed over fields used in the M-H measurement. Spin glasses have been reported in many cases to act as the fixed moment phase in core@shell nanoparticles [32], as well as in mechanically-synthesized [5, 6] and co-precipitated nanogranular systems (e.g., FiM/SG) [8]. The non-collinear magnetic structure inherent in ferrite SG layers, due to finite size effects and broken exchange bonds at the FiM surface, can be biased using a magnetic field and frozen in this configuration upon cooling through its transition temperature (i.e., blocking temperature, T_B). The strong unidirectional anisotropy of the blocked SG phase effectively pins the moment of the reversible phase along the field cool direction, resulting in the EB effect (H_{EB}). In the present case, the unexpected horizontal loop shift, combined with small $NiFe_2O_4$ grains sizes (∼8-10 nm), supports the idea that SG phases may be present at $NiFe_2O_4$ surfaces, $NiFe_2O_4$/NiO interfaces, and $NiFe_2O_4$ grain boundaries due to structural imperfections from grain refinement.

Anomalous vertical displacement of the hysteresis curves towards higher positive moments also accompanies the EB shift in all samples except S850; that is, the magnitude of the magnetic moment measured at the largest field in the FC direction is not equal to the moment measured in the opposite direction (i.e., $|M(+20\text{ kOe})| \neq |M(-20\text{ kOe})|$). This indicates that a fraction of the magnetic moments biased along the FC direction do not rotate with a reversing field. This simultaneous occurrence of both horizontal and

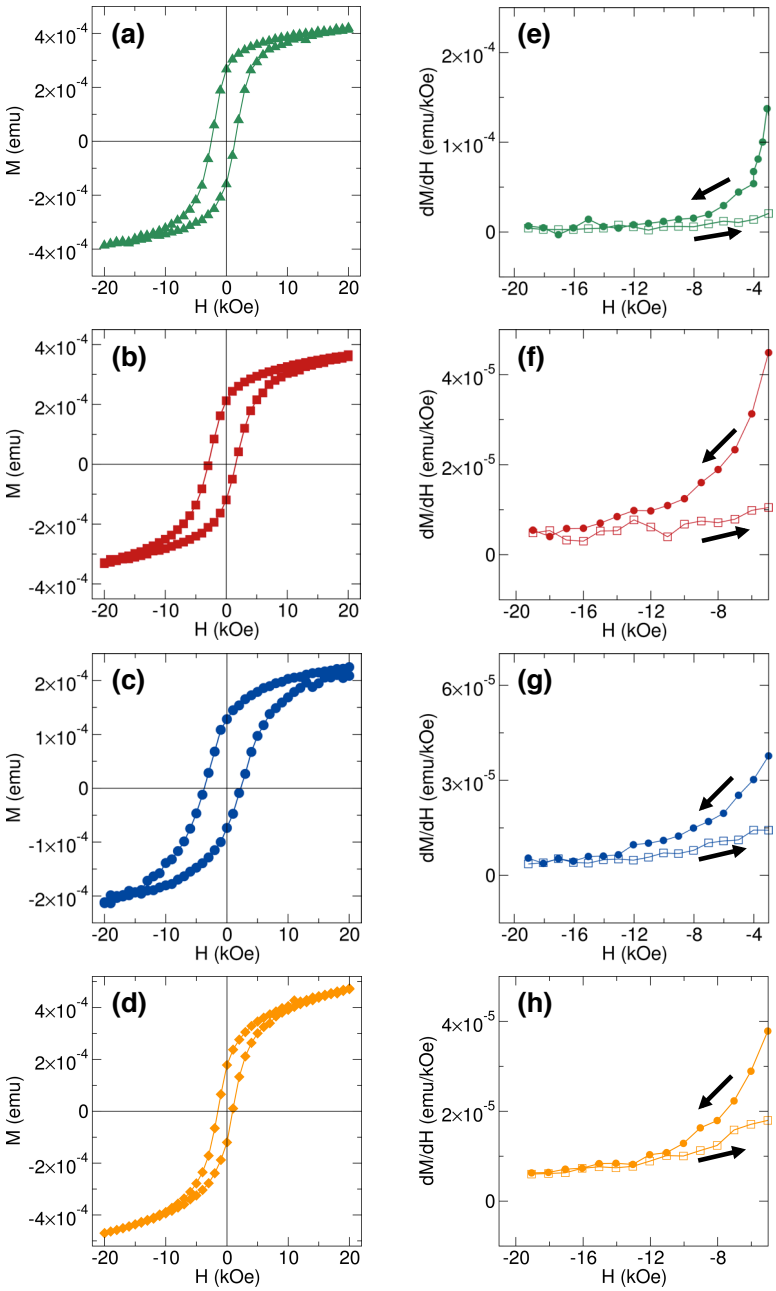

Figure 4.5: Magnetic hysteresis loops measured at 5 K after FC in a 20 kOe field from 300 K as shown in the insets of Figure 4.4 (a-d), and the first derivative of the descending and ascending regions of the hysteresis loops at high negative field (e-h) for the (a, e) S400, (b, f) S500, (c, g) S600, and (d, h) S850 $NiFe_2O_4$/NiO annealed films. Given that the derivatives coincide and become identical before reaching the maximum negative field of the measurement, the samples have attained an effective saturation and are in fact major hysteresis loops (see Ref. [28]).

vertical shifts of M-H loops at low temperatures is a reoccurring theme in spin glass systems [6, 8, 32]. Here, the strong unidirectional anisotropy of the frozen spins (responsible for the EB effect) are pinned along the FC direction and do not rotate when the field is reversed, resulting in a larger magnetization in the FC direction [33]. Even with the strong evidence of SG coupling, we cannot discount the possibility that there is also direct coupling between $NiFe_2O_4$ and NiO in this sample, where the Néel temperature (T_N) of NiO has been suppressed below 300 K due to finite size effects. The extent to which T_N is reduced has been debated in the literature and the large variance in degree appears to stem from measurement technique (i.e., electron spin resonance [34], low field ZFC magnetic susceptibility [35], neutron diffraction [36] and muon spin relaxation/rotation [37]), identity of the antiferromagnet, and particle size and shape [37].

To investigate the origin of this EB effect, the temperature dependence of the magnetic moment was measured for both ZFC and FC cases in a 20 kOe field (Figure 4.6). The ZFC M-T curves for all annealed samples diverge from the FC curves at a characteristic "irreversibility" temperature, T_{irr}, defined as the temperature where $\Delta m = M_{FC} - M_{ZFC} \neq 0$ (denoted by arrows in Figure 4.6). This divergence hints at the existence of exchange coupling in spin disordered systems [6]. The peak of the ZFC curve is the magnetic transition temperature (i.e., blocking temperature, T_B), below which the uncompensated spins in the SG layer are frozen into a glassy, metastable state. The broad ZFC curve indicates a wide distribution of transition temperatures, i.e., a broad energy barrier distribution between metastable spin configurations in the system that may be explained by varying SG layer thickness and exchange coupling energies. The irreversibility and blocking temperatures tend to lower temperatures when increasing the anneal temperature, which can be associated with a reduction of structural/magnetic disorder at interfaces. This conclusion is further supported by the reduction of the difference in moment at 5 K between the FC and ZFC curves (normalized by the ZFC moment) with

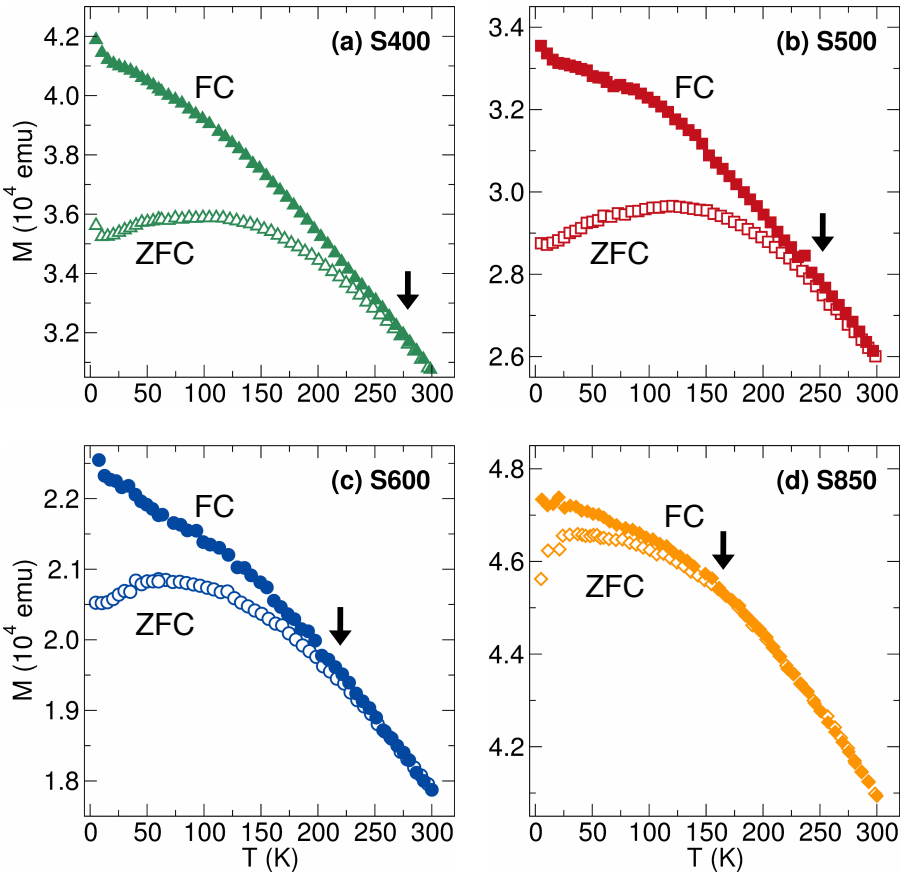

Figure 4.6: Temperature dependent ZFC (open symbols) and FC (closed symbols) magnetic moments measured in a 20 kOe field for the (a) S400, (b) S500, (c) S600, and (d) S850 $NiFe_2O_4$/NiO annealed films. Arrows denote the temperature at which the ZFC and FC curves diverge.

annealing temperature (i.e., $(\Delta m/\ M_{ZFC})_{5K} = 0.18$, 0.17, 0.10, and 0.04 for S400, S500, S600, and S850 samples, respectively).

The temperature dependence of EB was studied by extracting H_{EB} from FC M-H curves measured at multiple temperatures between 300 K and 5 K (Figure 4.7). The EB effect is absent at higher temperatures, becomes observable at some lower temperature and then increases monotonically with decreasing temperature. The temperature at which the EB effect emerges for each annealed sample appears to correlate with the irreversibility temperature defined above, except for the S850 sample (indicated by arrows in Figures 4.6 and 4.7). This result implies that the EB phenomenon in the S400 to S600

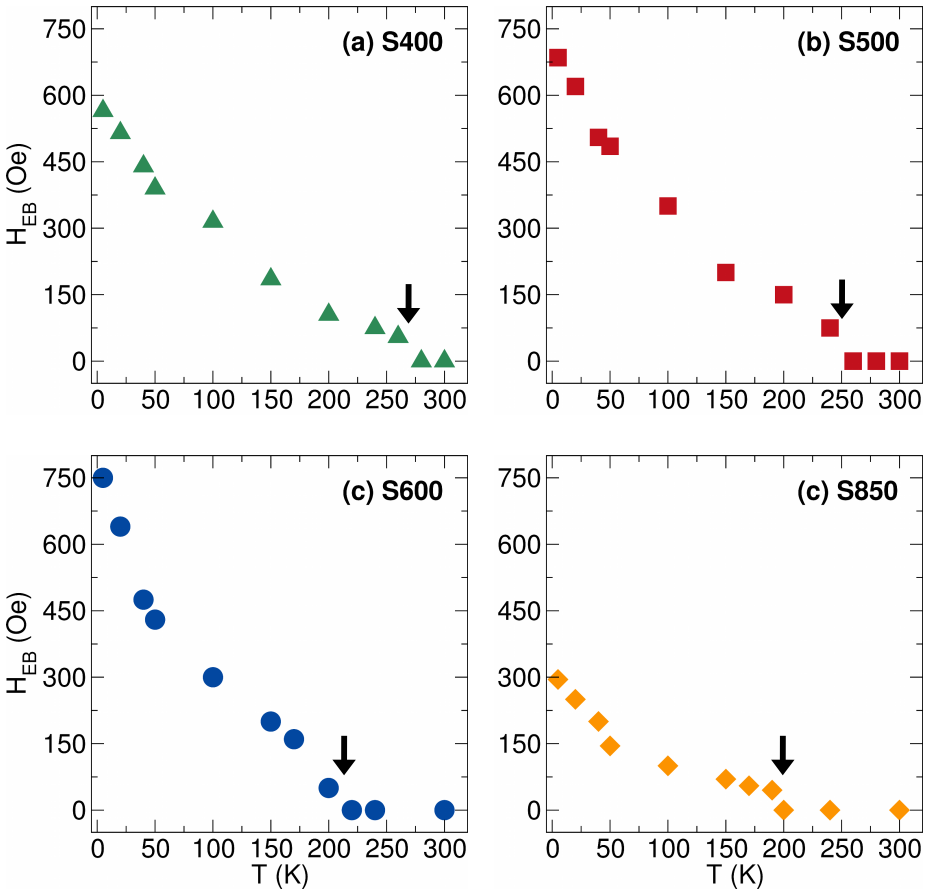

Figure 4.7: Temperature dependence of exchange bias (H_{EB}) in the (a) S400, (b) S500, (c) S600, and (d) S850 $NiFe_2O_4$/NiO annealed films after FC from 300 K in a 20 kOe field. Arrows indicate the temperature at which H_{EB} becomes observable.

annealed samples can be explained by coupling between FiM $NiFe_2O_4$ grains and a SG layer at the interface. Multiple metastable configurations of the non-collinear magnetic structure of the SG phase can be accessed at higher temperatures where thermal energies are comparable to metastable energy barriers. This non-robust magnetic structure results in weak coupling between the FiM and SG. Once T_{irr} is reached, some of the uncompensated spins become frozen along the FC direction and couple to the reversible moment of the FiM, resulting in the EB effect. As the number of frozen spins along the FC direction increase with decreasing temperature, there will be more FiM/SG coupling interactions at the interface, resulting in a larger loop shift.

Moreover, a small vertical displacement of the FC hysteresis curves appears for the S400 to S600 annealed samples at temperatures below their respective T_{irr}. This observation is common in spin glass systems and suggests that there exists a relationship between EB and the vertical displacement of the loop [6, 8]. Zheng *et al.* have proposed a simple model to explain this relationship where H_{EB} is related to the pinning energy in the system and is given by $H_{EB} = \Delta E/2M_R$ [32]. Here, M_R is the saturation magnetization of the reversible spins, and ΔE is the energy barrier to overcome when M_R reverses with applied field. The magnitude of ΔE is dependent on the coupling strength between the frozen SG spins and those of the reversible phase, which increases with the number of exchange interactions. As such, ΔE scales with the number of frozen SG spins at the interface and can be directly measured by the vertical shift of the hysteresis loop, ΔM. Therefore, H_{EB} should be related to ΔM as $H_{EB} \propto \Delta M/M_R$. To test this, H_{EB} and ΔM were extracted from FC loops measured below T_{irr} for each annealed sample, and plotted against each other (Figure 4.8). The observed linear relationship demonstrates that the SG spins pinned along the FC direction are likely responsible for both the horizontal and vertical shifts observed for the hysteresis curves measured below T_{irr}.

Conversely, the EB witnessed in the S850 sample does not appear to be from FiM/SG coupling, as evidenced by the lack of a vertical shift of the FC hysteresis loops and the lack of correlation between T_{irr} (Figure 4.6(d)) and the onset of EB (Figure 4.7(d)). The apparent disappearance of the SG phase after 850 °C may be reasoned by the following: (i) all amorphous regions in the film crystallized, eliminating any spin-disordered phase, and/or (ii) the substantial size increase of $NiFe_2O_4$ grains from ∼8 nm to 26 nm, which results in a large increase of the particle volume/surface ratio, effectively drowns out the effects of the interfacial FiM/SG coupling. As such, the origin of the EB effect in this case is most likely due to coupling between $NiFe_2O_4$ (FiM) and NiO (AFM). EB is unlikely to appear in a bulk system where NiO is the AFM without FC through T_N of

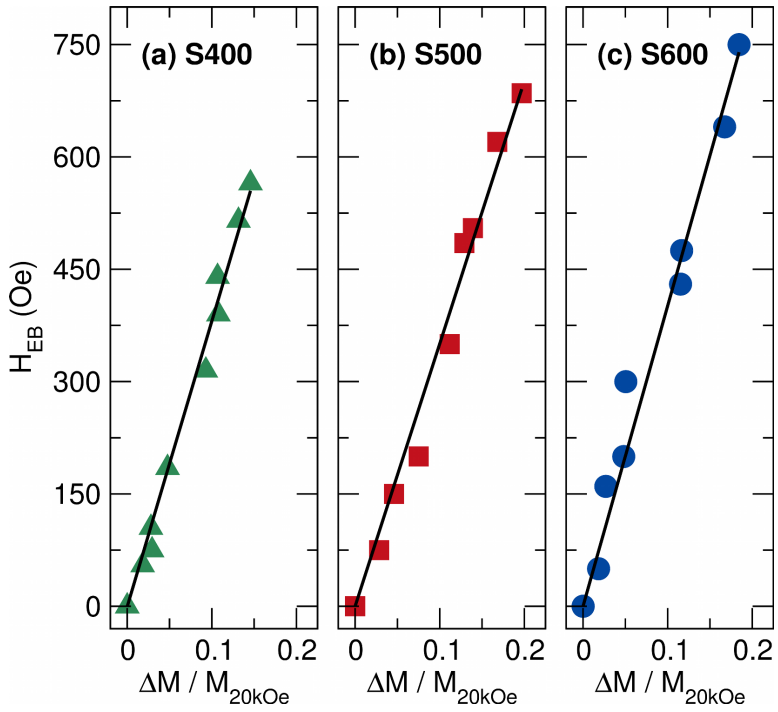

Figure 4.8: Correlation of horizontal (H_{EB}) and vertical (ΔM) hysteresis loop shifts for the (a) S400, (b) S500, and (c) S600 $NiFe_2O_4$/NiO annealed samples, where H_{EB} and ΔM were obtained for each sample from the corresponding set of FC hysteresis loops measured at multiple temperatures. The solid lines demonstrate the linear dependence of H_{EB} with ΔM.

NiO (525 K); however, when the NiO grains are confined to the nanoscale, a reduction in T_N may be observed [36, 38].

Variations in exchange bias (H_{EB}) and coercivity (H_C) at 300 and 5 K for all samples are summarized in Figure 4.9. The large decrease in H_{EB} from the AsDep to S400 samples indicates a substantial improvement in crystallinity, diminishing the amount of spin disorder at $NiFe_2O_4$/NiO interfaces and surfaces. Meanwhile, the drastic change in phase fraction with annealing seems to play a significant role in the amount of spin coupling at $NiFe_2O_4$ interfaces. Interestingly, H_{EB} and H_C increased with higher annealing temperature from 400 to 600 °C. It was found that the EB in these films was due to FiM/SG coupling, and that the thickness of the glassy layer decreased with higher annealing temperatures, which would instead suggest a trend opposing the one seen here.

This surprising result may be due to more crystalline and smoother interfaces with higher heat treatment, where there is better connection between the SG and $NiFe_2O_4$ spins, resulting in stronger coupling at the interface with more FiM/SG spins participating in EB. Upon increasing the annealing temperature to 850 °C, EB becomes dominated by $NiFe_2O_4$/NiO interactions (i.e., FiM/AFM) where the anisotropy, and thus the coupling, of the AFM is weaker than the SG phase. Furthermore, the much larger $NiFe_2O_4$ grain size in the S850 sample would tend to increase the FiM anisotropy energy, which requires higher pinning energy from interfacial exchange coupling to oppose moment reversal with field, effectively lowering the observed H_{EB}. The H_C measured at both 300 and 5 K fol-

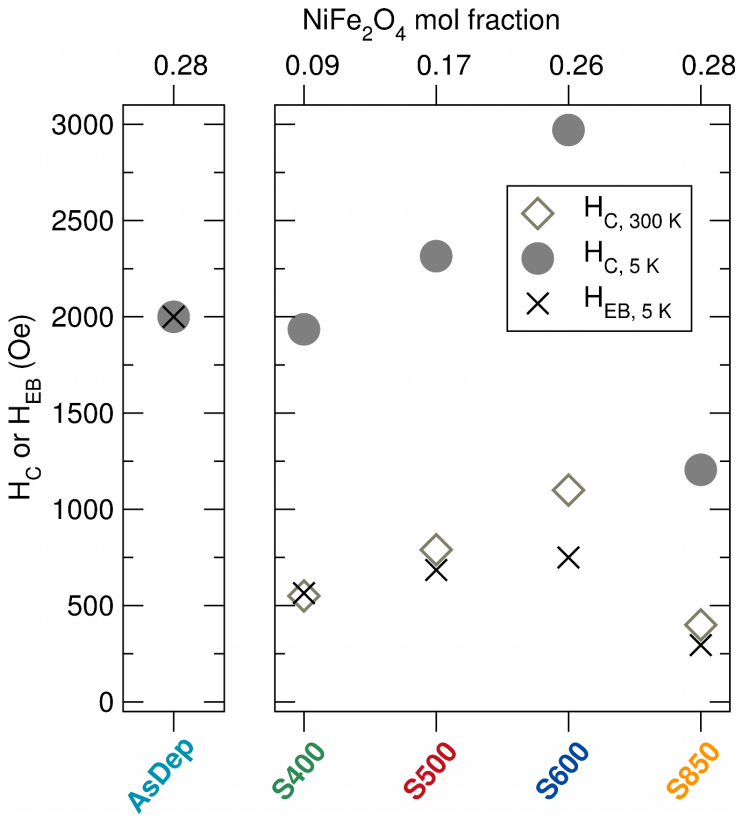

Figure 4.9: Coercivity (H_C) and exchange bias (H_{EB}) for the as-deposited and annealed $NiFe_2O_4$/NiO films; H_C was measured at 300 and 5 K, and H_{EB} was measured at 5 K. Note: The signal-to-noise ratio of the AsDep sample at 300 K was extremely low and H_C could not be determined, suggesting that the AsDep film has structural and magnetic disorder.

low the same trend as H_{EB} measured at 5 K (Figure 4.9), and can be interpreted using similar arguments as used for H_{EB}. Room temperature coercivity as high as 1100 Oe was realized for the S600 sample, which is significantly higher than what has been reported for the $NiFe_2O_4$/NiO nanogranular or bilayer systems (see Refs. [8, 39]). These results demonstrate the viability of using MPs as a deposition source to fashion biphasic, nanogranular films exhibiting EB and room temperature stability of nanoscale magnetic materials (< 20 nm) for potential data storage technologies.

4.4 Conclusions

In this chapter, we presented a detailed study of the EB effect in biphasic $NiFe_2O_4$/NiO nanogranular films synthesized with high-pressure MPs and post-deposition annealing. The EB seen in the as-deposited and low-temperature annealed (≤ 600 °C) films was found to originate from coupling between nanocrystalline $NiFe_2O_4$ and a structurally-disordered SG-like phase. The EB effect became observable at and below the temperature where the ZFC and FC M-T curves diverge, i.e., the temperature where SG spins begin to freeze along the FC direction and pin the reversible $NiFe_2O_4$ spins, resulting in a horizontal shift of hysteresis loops. Furthermore, a concomitant vertical shift (ΔM) of the hysteresis loop was observed and found to be directly proportional to the magnitude of H_{EB}, indicating that the same SG-like spins are likely responsible. At higher annealing temperatures (850 °C), the observed EB was not accompanied by a vertical loop shift and is believed to be from direct exchange coupling between $NiFe_2O_4$ and NiO, where the SG-like phase is no longer present. The significant decrease in H_C and H_{EB} from the S600 to S850 samples was attributed to SG versus AFM pinning of FiM spins and a large increase in $NiFe_2O_4$ grain size ($\sim$10 to 26 nm). The large room temperature H_C observed for samples S400 to S600 are noteworthy for applications requiring magnetic stability of

magnetic nanostructures (∼10 nm) at room temperature. Moreover, this work demonstrates the feasibility of using MP-based deposition to fashion a wider range of biphasic, nanogranular films to study exchange bias phenomena.

References

[1] J. Nogués, J. Sort, V. Langlais, S. Doppiu, B. Dieny, J. Munoz, S. Surinach, M. Baró, S. Stoyanov, and Y. Zhang, "Exchange bias in ferromagnetic nanoparticles embedded in an antiferromagnetic matrix," *Int. J. Nanotechnol.*, vol. 2, no. 1-2, pp. 23–42, 2005.

[2] M. Artus, S. Ammar, L. Sicard, J.-Y. Piquemal, F. Herbst, M.-J. Vaulay, F. Fiévet, and V. Richard, "Synthesis and magnetic properties of ferrimagnetic $CoFe_2O_4$ nanoparticles embedded in an antiferromagnetic NiO matrix," *Chem. Mater.*, vol. 20, no. 15, pp. 4861–4872, 2008.

[3] Z. Tian, S. Yuan, S. Yin, L. Liu, J. He, H. Duan, P. Li, and C. Wang, "Exchange bias effect in a granular system of $NiFe_2O_4$ nanoparticles embedded in an antiferromagnetic NiO matrix," *Appl. Phys. Lett.*, vol. 93, no. 22, p. 222505, 2008.

[4] L. Del Bianco, D. Fiorani, A. M. Testa, E. Bonetti, and L. Signorini, "Field-cooling dependence of exchange bias in a granular system of Fe nanoparticles embedded in an Fe oxide matrix," *Phys. Rev. B*, vol. 70, no. 5, p. 052401, 2004.

[5] L. Del Bianco, F. Boscherini, M. Tamisari, F. Spizzo, M. V. Antisari, and E. Piscopiello, "Exchange bias and interface structure in the Ni/NiO nanogranular system," *J. Phys. D: Appl. Phys.*, vol. 41, no. 13, p. 134008, 2008.

[6] E. Passamani, C. Larica, C. Marques, J. Proveti, A. Takeuchi, and F. Sanchez, "Exchange bias and anomalous vertical shift of the hysteresis loops in milled Fe/MnO_2 material," *J. Magn. Magn. Mater.*, vol. 299, no. 1, pp. 11–20, 2006.

[7] L. Wang, C. Zhu, D. Bao, Z. Tian, and S. Yuan, "Giant exchange bias behavior and training effect in spin-glass-like $NiCr_2O_4$/NiO ceramics," *J. Mater. Sci.*, vol. 50, no. 17, pp. 5904–5911, 2015.

[8] Z. Tian, S. Huang, Y. Qiu, S. Yuan, Y. Wu, and L. Li, "Size-dependent scaling of exchange bias in $NiFe_2O_4$/NiO nanogranular systems synthesized by a phase separation method," *J. Appl. Phys.*, vol. 113, no. 14, p. 143906, 2013.

[9] J. M. D. Coey, "Noncollinear spin arrangement in ultrafine ferrimagnetic crystallites," *Phys. Rev. Lett.*, vol. 27, no. 17, p. 1140, 1971.

[10] R. H. Kodama, A. E. Berkowitz, E. McNiff Jr, and S. Foner, "Surface spin disorder in $NiFe_2O_4$ nanoparticles," *Phys. Rev. Lett.*, vol. 77, no. 2, p. 394, 1996.

[11] C. Zhu, Z. Tian, L. Wang, and S. Yuan, "Exchange bias effect in spin glass $CoCr_2O_4$ nanoparticles," *J. Magn. Magn. Mater.*, vol. 393, pp. 116–120, 2015.

[12] R. H. Kodama, S. A. Makhlouf, and A. E. Berkowitz, "Finite size effects in antiferromagnetic NiO nanoparticles," *Phys. Rev. Lett.*, vol. 79, no. 7, p. 1393, 1997.

[13] A. C. Bose, Y. Shimizu, D. Mariotti, T. Sasaki, K. Terashima, and N. Koshizaki, "Flow rate effect on the structure and morphology of molybdenum oxide nanoparticles deposited by atmospheric-pressure microplasma processing," *Nanotechnology*, vol. 17, no. 24, p. 5976, 2006.

[14] R. M. Sankaran, D. Holunga, R. C. Flagan, and K. P. Giapis, "Synthesis of blue luminescent Si nanoparticles using atmospheric-pressure microdischarges," *Nano Lett.*, vol. 5, no. 3, pp. 537–541, 2005.

[15] W.-H. Chiang, C. Richmonds, and R. M. Sankaran, "Continuous-flow, atmospheric-pressure microplasmas: a versatile source for metal nanoparticle synthesis in the gas or liquid phase," *Plasma Sources Sci. Technol.*, vol. 19, no. 3, p. 034011, 2010.

[16] T. L. Koh, E. C. O'Hara, and M. J. Gordon, "Microplasma-based synthesis of vertically aligned metal oxide nanostructures," *Nanotechnology*, vol. 23, no. 42, p. 425603, 2012.

[17] T. Koh, E. O'Hara, and M. Gordon, "Growth of nanostructured CuO thin films via microplasma-assisted, reactive chemical vapor deposition at high pressures," *J. Cryst. Growth*, vol. 363, pp. 69–75, 2013.

[18] D. Mariotti, H. Lindström, A. C. Bose, and K. K. Ostrikov, "Monoclinic β-MoO_3 nanosheets produced by atmospheric microplasma: application to lithium-ion batteries," *Nanotechnology*, vol. 19, no. 49, p. 495302, 2008.

[19] D. Mariotti and R. M. Sankaran, "Microplasmas for nanomaterials synthesis," *J. Phys. D: Appl. Phys.*, vol. 43, no. 32, p. 323001, 2010.

[20] D. Mariotti and R. M. Sankaran, "Perspectives on atmospheric-pressure plasmas for nanofabrication," *J. Phys. D: Appl. Phys.*, vol. 44, no. 17, p. 174023, 2011.

[21] A. C. Pebley, A. Peek, T. M. Pollock, and M. J. Gordon, "Microplasma-based growth of biphasic $NiFe_2O_4$/NiO nanogranular films for exchange bias applications," *Chem. Mater.*, vol. 26, no. 20, pp. 6026–6032, 2014.

[22] P. Scherrer, "Bestimmung der grösse und der inneren struktur von kolloidteilchen mittels röntgenstrahlen," *Nachr. Ges. Wiss. Gött.*, vol. 2, p. 98, 1918.

[23] Z. Tian, S. Yuan, L. Liu, S. Yin, L. Jia, P. Li, S. Huo, and J. Li, "Exchange bias training effect in $NiFe_2O_4$/NiO nanocomposites," *J. Phys. D: Appl. Phys.*, vol. 42, no. 3, p. 035008, 2009.

[24] M. Rhamdhani, P. Hayes, and E. Jak, "Subsolidus phase equilibria of the Fe-Ni-O system," *Metall. Mater. Trans. B*, vol. 39, no. 5, pp. 690–701, 2008.

[25] K. E. Sickafus, J. M. Wills, and N. W. Grimes, "Structure of spinel," *J. Am. Ceram. Soc.*, vol. 82, no. 12, pp. 3279–3292, 1999.

[26] R. Messier, A. Giri, and R. Roy, "Revised structure zone model for thin film physical structure," *J. Vac. Sci. Technol. A*, vol. 2, no. 2, pp. 500–503, 1984.

[27] S. Lin, D. Shao, J. Lin, L. Zu, X. Kan, B. Wang, Y. Huang, W. Song, W. Lu, P. Tong, *et al.*, "Spin-glass behavior and zero-field-cooled exchange bias in a Cr-based antiperovskite compound $PdNCr_3$," *J. Mater. Chem. C*, vol. 3, no. 22, pp. 5683–5696, 2015.

[28] A. Harres, M. Mikhov, V. Skumryev, A. de Andrade, J. Schmidt, and J. Geshev, "Criteria for saturated magnetization loop," *J. Magn. Magn. Mater.*, vol. 402, pp. 76–82, 2016.

[29] J. Nogués, J. Sort, V. Langlais, V. Skumryev, S. Surinach, J. Munoz, and M. Baró, "Exchange bias in nanostructures," *Phys. Rep.*, vol. 422, no. 3, pp. 65–117, 2005.

[30] G. Salazar-Alvarez, J. Sort, S. Surinach, M. D. Baró, and J. Nogués, "Synthesis and size-dependent exchange bias in inverted core-shell MnO — Mn_3O_4 nanoparticles," *J. Am. Chem. Soc.*, vol. 129, no. 29, pp. 9102–9108, 2007.

[31] J. Geshev, "Comment on: "exchange bias and vertical shift in $CoFe_2O_4$ nanoparticles" [J. Magn. Magn. Mater. 313 (2007) 266]," *J. Magn. Magn. Mater.*, vol. 320, no. 3, pp. 600–602, 2008.

[32] R. Zheng, G. Wen, K. Fung, and X. Zhang, "Giant exchange bias and the vertical shifts of hysteresis loops in γ-Fe_2O_3-coated Fe nanoparticles," *J. Appl. Phys.*, vol. 95, no. 9, pp. 5244–5246, 2004.

[33] H. Ohldag, A. Scholl, F. Nolting, E. Arenholz, S. Maat, A. Young, M. Carey, and J. Stöhr, "Correlation between exchange bias and pinned interfacial spins," *Phys. Rev. Lett.*, vol. 91, no. 1, p. 017203, 2003.

[34] S. Sako and K. Ohshima, "Antiferromagnetic transition temperature of MnO ultrafine particle," *J. Phys. Soc. Jpn.*, vol. 64, no. 3, pp. 944–950, 1995.

[35] T. Ambrose and C. Chien, "Finite-size effects and uncompensated magnetization in thin antiferromagnetic CoO layers," *Phys. Rev. Lett.*, vol. 76, no. 10, p. 1743, 1996.

[36] S. N. Klausen, P.-A. Lindgård, K. Lefmann, F. Bødker, and S. Mørup, "Temperature dependence of the magnetization of disc shaped NiO nanoparticles," *Phys. Status Solidi A*, vol. 189, no. 3, pp. 1039–1042, 2002.

[37] X. Zheng, C. Xu, K. Nishikubo, K. Nishiyama, W. Higemoto, W. Moon, E. Tanaka, and E. S. Otabe, "Finite-size effect on Néel temperature in antiferromagnetic nanoparticles," *Phys. Rev. B*, vol. 72, no. 1, p. 014464, 2005.

[38] D. Alders, L. Tjeng, F. Voogt, T. Hibma, G. Sawatzky, C. Chen, J. Vogel, M. Sacchi, and S. Iacobucci, "Temperature and thickness dependence of magnetic moments in NiO epitaxial films," *Phys. Rev. B*, vol. 57, no. 18, p. 11623, 1998.

[39] B. Negulescu, L. Thomas, Y. Dumont, M. Tessier, N. Keller, and M. Guyot, "Exchange biasing in $NiO/NiFe_2O_4$ bilayers," *J. Magn. Magn. Mater.*, vol. 242, pp. 529–531, 2002.

Chapter 5

Oxygen evolution on Fe-doped NiO electrocatalysts deposited via microplasma

5.1 Introduction

Comparing the performance of heterogeneous catalysts against different material classes and synthesis techniques has been difficult due to the large variation in electrochemical measurement conditions used among research groups. McCrory *et al.* have outlined an approach to standardize the evaluation of the catalyst activity where the overpotential required to generate 10 mA of O_2 production per cm^2 of geometric area of catalyst is the primary figure of merit [1]. One such way to decrease the 'apparent' overpotential is to increase the number of active sites (surface area) exposed to the electrolyte for a given geometric area. Approaches used to synthesize heterogeneous electrocatalysts include solid-state [2], solvothermal [3–5], and hydrothermal methods [6]. These techniques often require many steps and long processing times, and the resulting catalysts

are typically powders that are either spin-cast onto a substrate or anchored down using a polymer binder such as Nafion. The resulting thin films are dense with low roughness 'factor' (i.e., ratio of the true-to-geometric surface area), with a correspondingly low number of catalytically active sites exposed to the electrolyte for oxygen evolution. Additionally, the use of polymer binders generally results in poor mechanical stability of the catalyst, and can lead to peeling or flaking of the catalyst when operated for long times at OER potentials [7].

In this chapter, the use flow-through microplasma (MP) jets [8, 9] to synthesize Ni-Fe oxide films with large surface areas exhibiting high activity and excellent stability for OER is discussed. MP jets show great potential for direct spray deposition of conformal coatings of Ni-Fe and other oxide catalysts on a variety of substrates with unique architectures, such as Ni foams, graphene, and carbon nanotubes, which have all been shown to greatly enhance activity and charge transfer efficiency from catalyst to substrate [18–22]. Specifically, the study of microplasma-based deposition of Fe_2O_3, NiO and $Ni_{1-x}Fe_xO$ (x=0.05–0.19) thin film catalysts on ITO for OER was explored. Film morphology, structure, and surface chemical state as a function of Fe loading were investigated to understand the catalytic activity for oxygen evolution in basic media. It was found that incorporating Fe into the rocksalt NiO structure results in a significant decrease in overpotential compared to both mono-oxide phases (i.e., 320 vs. 360 mV @ 10 mA/cm^2 for $Ni_{0.95}Fe_{0.05}O$ and NiO, respectively). Interestingly, overpotentials were found to not vary considerably (310 to 325 mV) with Fe doping in $Ni_{1-x}Fe_xO$, so long as the Fe content was above x=0.05. This result was attributed to a simultaneous change in morphology and reduced crystallinity of the films with higher Fe content, as well as from mass transport phenomena and variations in electrical conductivity among different $Ni_{1-x}Fe_xO$ films. Catalyst stability at OER-relevant conditions was tested using chronopotentiometry, and its effect on the structural and chemical properties of the cat-

alyst surface were assessed using scanning electron microscopy (SEM) and ex-situ X-ray photoelectron spectroscopy (XPS), respectively. Finally, this chapter demonstrates that microplasmas offer a general synthesis route for mono and mixed metal oxide catalysts for OER and other electrochemical applications.

5.2 Experimental Procedure

5.2.1 Microplasma-based deposition of electrocatalysts

Figure 2.4 shows a schematic of the microplasma reactor used to deposit Fe_2O_3, NiO and $Ni_{1-x}Fe_xO$ (x=0.05–0.19) thin films on ITO substrates as OER catalysts. Nickelocene ($Ni(Cp)_2$) and ferrocene ($Fe(Cp)_2$) (Strem Chemicals, Inc.) vapors were entrained in an Ar gas stream with trace amounts of O_2 (0.154 vol%) and delivered to the hollow-cathode (200 sccm), where the feedstock was dissociated via electron impact to form small Ni-Fe oxide clusters/nanoparticles. The gas-phase nanoparticles were subsequently spray-deposited onto unheated ITO substrates ($\sim$ 70 °C due to local heating from plasma afterglow) located 1 cm downstream of the capillary exit to form nanostructured $Ni_{1-x}Fe_xO$ or Fe_2O_3 films as OER catalysts. The substrate stage was raster scanned during growth (serpentine pattern at 0.17 mm/s) to deposit larger area films (4×4 mm^2), and the chamber was held at a constant pressure of 20 Torr. All samples were deposited on both ITO and <100> Si substrates, the latter being used for materials characterization studies. Finally, the composition of the resulting films was controlled by varying the Ar flow rate through the individually sealed $Ni(Cp)_2$ and $Fe(Cp)_2$ precursor cells, which were held at constant temperatures of 20 °C and 7 °C, respectively.

5.2.2 Physical characterization

An FEI XL30 Sirion FEG scanning electron microscope (SEM) equipped with an EDAX Si-drift energy dispersive X-ray (EDX) detector was used to measure bulk compositions of $Ni_{1-x}Fe_xO$ films on ITO using a 20 kV accelerating voltage. High-resolution images were obtained using an FEI Nova Nano 650 FEG SEM with 5 kV accelerating voltage. Plan-view and cross-sectional images were taken from films deposited on ITO and Si, respectively.

Bragg-Brentano X-ray diffraction (XRD) was performed on films deposited on Si substrates using a PANalytical Empyrean X-ray diffractometer outfitted with monochromatic Cu-Kα (λ=1.54056 Å) radiation and a high-resolution PIXcel 1D detector. The diffraction geometry was offset by -4° to eliminate the high intensity <004> Si peak at ∼69° 2θ from the underlying substrate. All patterns of the $Ni_{1-x}Fe_xO$ (x=0–0.19) films were collected in a 2θ range from 28 to 82° with a step size of 0.013° and a scan rate of 0.627 s/step, whereas the Fe_2O_3 film was scanned from 20-58° 2θ with a step size of 0.013° and 0.855 s/step scan rate. Grain size was calculated from the most intense reflection using the Scherrer equation after calibrating the diffractometer with a sintered alumina plate (SRM 1976a; NIST) to account for instrument broadening and measurement geometry.

A Kratos Axis Ultra X-ray photoelectron spectroscopy (XPS) system with a monochromated Al source (1486.6 eV) was used to measure the surface composition as well as to assess the chemical surface states of all $Ni_{1-x}Fe_xO$ films deposited on ITO. Since the Ni (LMM) Auger peaks overlap with the Fe 2p photoelectron line when using monochromated Al X-rays, surface compositions were determined from the Ni 3s and Fe 3p peaks, where the relative sensitivity factors were calibrated beforehand using NiO and Fe_2O_3 standards, respectively. Survey scans were obtained using a pass energy of 160 eV with

a 0.5 eV step size and 150 ms dwell time; high-resolution scans were obtained using a 20 eV pass energy with a 0.1 eV step size and 500 ms dwell time. All data was collected using charge compensation and corrected by setting the true position of the adventitious C 1s line to 285.0 eV.

5.2.3 DFT electronic structure calculations

Spin-polarized density functional theory (DFT) calculations were carried out using the Vienna *Ab Initio* Software Package [23–26] (VASP) version 5.4.1, using the PBESol [27] functional, which provides superior accuracy for equilibrium properties calculated in dense solids. Projector-augmented wave [28, 29] (PAW) pseudo-potentials treating the 4s electrons as valence states for Fe and Ni were chosen from the GW PAW set provided with VASP.

To understand if Fe substitutes Ni in NiO, and how this impacts the lattice parameter, we utilized the CASM [30–33] software package to enumerate several hundred (> 800) symmetrically distinct supercells of the cubic rocksalt primitive cell. To ensure proper breaking of the magnetic symmetry, and to avoid local magnetic minima and a potentially inaccurately calculated lattice parameter via magnetostriction, we considered both the chemical (Ni/Fe) and magnetic (Up/Down) degrees of freedom when performing our enumerations. In the case where two or more configurations with identical chemistry (Ni/Fe placement) but different starting magnetic configurations relaxed onto the same final magnetic state, the calculation resulting in the lowest relaxed energy was used.

5.2.4 Electrochemical measurements

Electrochemical measurements were carried out in a three-electrode setup housed in a glass round bottom flask using a Gamry Series G 300 potentiostat. All measurements

were performed in 0.5 M KOH electrolyte solution (pH=13.7), made from certified ACS grade KOH pellets (Fisher Scientific) and ultra-high purity H_2O (17.9 MΩ·cm). Pt mesh was used as the counter electrode. $Ni_{1-x}Fe_xO$ or Fe_2O_3 films on conductive ITO substrates were used as the working electrode (WE). Recorded potentials were measured against a Ag/AgCl/sat'd KCl reference electrode, which was positioned ∼1 cm from the WE using a Luggin capillary. Electrochemical data were corrected for uncompensated resistance, R_S (i.e., solution resistance between reference and working electrodes), using electrochemical impedance spectroscopy. R_S was attributed to the total impedance measured at 170 kHz using an open circuit potential of 0.1 V vs Ag/AgCl/sat'd KCl, where no Faradaic processes took place. Typical R_S values ranged from 20–30 Ω and were sensitive to the exact position of the Luggin capillary with respect to the WE. Positive feedback correction was used during cyclic voltammetry measurements to compensate 90% of R_S, and the remaining resistance was compensated manually on the collected data when necessary for precise evaluation of catalyst activity. Current densities were calculated using the geometric area of the deposited square films (16 mm^2).

Preconditioning was achieved by allowing the catalysts to soak for 10 min in a magnetically stirred 0.5 M KOH electrolyte under constant aeration with N_2 followed by cyclic voltammetry (CV). All catalysts were cycled between -0.1 to 0.6 V (or 0.7 V for less active catalysts) vs. Ag/AgCl/sat'd KCl electrode at a scan rate of 20 mV/s until OER currents reached stable values. The number of cycles varied between 20 and 40, where films with higher Fe content stabilized more quickly. After preconditioning, CV scans from -0.1 to 0.6 or 0.7 V vs. Ag/AgCl/sat'd KCl at a scan rate of 10 mV/s were obtained for analysis of overpotentials (η) and the turnover frequency (TOF) on a per Ni atom basis. Finally, chronopotentiometry measurements were conducted at a constant current of 10 mA/cm^2 for a duration of 2 hours to test the structural and chemical stability of the catalysts during OER. XPS, SEM and CV were used post-run to assess

changes in surface chemistry, morphology, and electrochemical behavior, respectively.

The overpotential, η, was evaluated using the equation $\eta = V_{meas} - [V_{meas}^{NHE} - V_{Ag/AgCl}^{NHE} - 0.059 \times pH] - iR_S$, where V_{meas} is the measured potential vs. the Ag/AgCl/sat'd KCl reference electrode. The quantity in brackets represents the reversible potential of the OER vs. Ag/AgCl/sat'd KCl (0.225 V at a pH of 13.7), where V_{OER}^{NHE} is the thermodynamic potential of OER vs. NHE (1.23 V), $V_{Ag/AgCl}^{NHE}$ is the potential of Ag/AgCl/sat'd KCl vs. NHE (0.197 V), and the final term is the pH dependence of the potential obtained from the Nernst equation. Finally, i is the current and iR_S is the voltage drop due to the uncompensated resistance.

The turnover frequency (TOF) was calculated as the number of O_2 molecules generated per electrochemically accessible Ni site per second at η=300 and 350 mV. The number of O_2 molecules produced per second was obtained by measuring the current at η=300 or 350 mV, where we assumed the evolution of oxygen ($4OH^-_{(aq)} \longrightarrow 2H_2O_{(l)} + O_{2(g)} + 4e^-$) had a 100% Faradaic efficiency so that every 4 electrons collected equated to the formation of one O_2 molecule. The number of electrochemically accessible Ni sites was estimated by integrating the cathodic peak ($NiOOH + H_2O + e^- \longrightarrow Ni(OH)_2 + OH^-$) to obtain the total charge transferred. One electron transferred per Ni atom was assumed, which may overestimate the total number of Ni sites giving a lower bound for the TOF [34].

5.3 Results and discussion

5.3.1 Structure and morphology

The surface and bulk compositions of Fe_2O_3, NiO, and $Ni_{1-x}Fe_xO$ (x=0.05–0.19) nanostructured thin films on ITO were obtained using XPS and EDX, respectively. Figure 5.1(a) clearly demonstrates that the surface and bulk compositions of the $Ni_{1-x}Fe_xO$ films

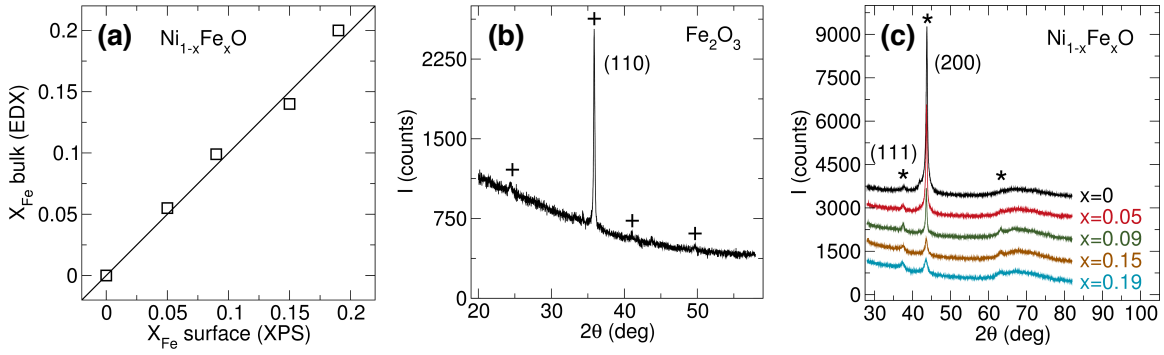

Figure 5.1: (a) Comparison of surface and bulk compositions of $Ni_{1-x}Fe_xO$ films obtained via XPS and EDX, respectively, where x has been measured on a metals basis (x=Fe/Fe+Ni). XRD spectra of as-deposited (b) Fe_2O_3 and (c) $Ni_{1-x}Fe_xO$ films, respectively. Plus (+) and star (*) symbols correspond to peak locations of hematite Fe_2O_3 and rocksalt NiO, respectively. The broad hump centered at ~69° 2θ is due to the underlying Si substrate and measurement geometry (-4° offset).

are in good agreement, where x has been measured on a metals basis (i.e., x=Fe/Fe+Ni). All as-deposited $Ni_{1-x}Fe_xO$ films are denoted in this chapter by their surface composition measured via XPS (i.e., x=0, 0.05, 0.09, 0.15, and 0.19). Figures 5.1(b) and (c) display the powder XRD spectra for the Fe-oxide and $Ni_{1-x}Fe_xO$ films, respectively. The Fe-oxide film was indexed as corundum Fe_2O_3 (R-3c), where the only high intensity peak was from (110) lattice planes, suggesting a highly textured <110> growth direction composed of crystals with an average grain size of 63 nm (calculated from the line broadening of the (110) reflection). The pure Ni oxide film and all mixed $Ni_{1-x}Fe_xO$ films were indexed to the cubic rocksalt structure (Fm3m). The large 25:1 ratio of the (200):(111) reflections for the as-deposited, pure NiO film is much greater than expected from a polycrystalline powder pattern (i.e., (200):(111) = 5:3; ICDD ref. pattern: Bunsenite, syn, 00-047-1049), implying that, like the Fe_2O_3 film, NiO is strongly textured with growth along the <100> direction and perpendicular to the substrate surface. Interestingly, the (200):(111) ratio progressively decreases with increasing Fe content in $Ni_{1-x}Fe_xO$ films with the smallest ratio of 2:1 seen in the x=0.19 sample, indicating that Fe incorporation reduces the preferred growth orientation of NiO.

Additionally, there is a continuous shift in the (200) rocksalt reflection to lower 2θ and a decreasing peak intensity with increasing Fe content, as can be seen in Figure 5.2(a). A shift to lower 2θ suggests that Fe^{2+} dopants are incorporating into the rocksalt NiO structure, resulting in an expansion of the lattice (ionic radius: Fe^{2+} (0.78 Å) > Ni^{2+} (0.69 Å) [35]). Electronic structure calculations were performed to verify this hypothesis and are displayed in Figure 5.2(b). The relative change in the rocksalt lattice parameter obtained both from XRD data and DFT calculations at 0 K ($\sim$ 6 and 7% dilation for x=0.19, respectively) are in good agreement and follow a Vegard's law dependence. Charge localization (as projected onto each atom) in the DFT calculations shows no abrupt changes in the charge distribution as Ni is replaced with Fe; that is, both species are consistently in the 2+ oxidation state.

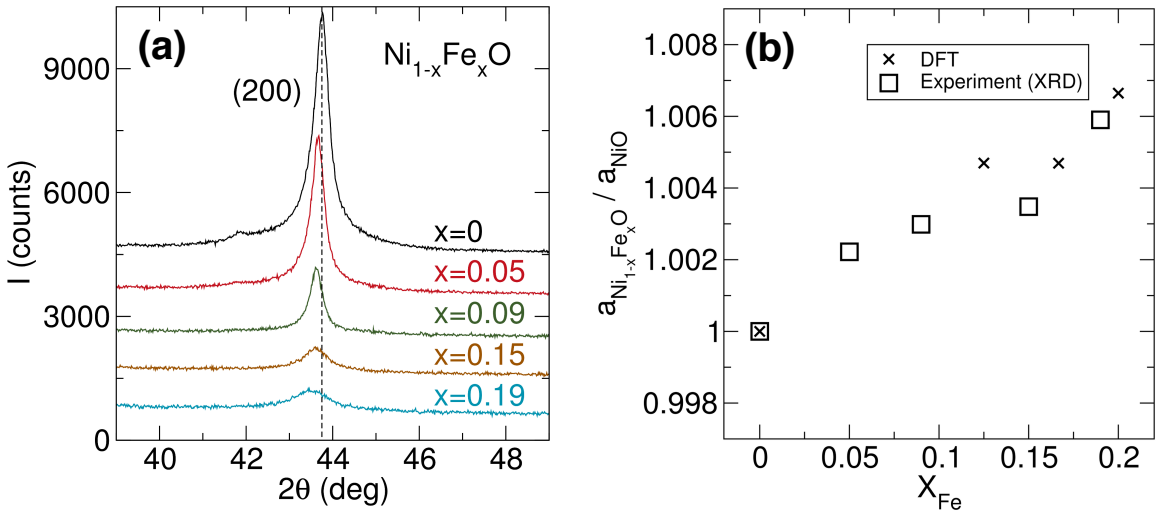

Figure 5.2: (a) Magnified view of (200) NiO reflection of $Ni_{1-x}Fe_xO$ films from Figure 5.1(c), demonstrating expansion of the NiO lattice with Fe incorporation (i.e., peak shift to lower 2θ with Fe). (b) Lattice parameter of rocksalt $Ni_{1-x}Fe_xO$ films normalized by pure NiO measured from XRD data, panel (a), and calculated from DFT assuming Fe^{2+} dopants. The good agreement between experiment and theory suggest that Fe^{2+} and not Fe^{3+} (Fe^{2+} > Ni^{2+} > Fe^{3+}) incorporates into the rocksalt NiO lattice during microplasma deposition.

The agreement between DFT and XRD, and investigation of the precise electronic structure, highly suggest that the lattice expansion is due to Fe^{2+} incorporation and not Fe^{3+}. Furthermore, the corresponding decrease in peak intensity with higher Fe content can be attributed to reduced crystallinity and/or smaller grain sizes. The average grain sizes for $Ni_{1-x}Fe_xO$ films were calculated from the (200) reflection. Films with lower Fe content ($x \leq 0.09$) had relatively large crystal sizes of ∼16–18 nm, whereas, smaller grain sizes of 9 and 6.5 nm were seen in the x=0.15 and 0.19 films, respectively. Finally, the formation of any Fe-rich phases in mixed $Ni_{1-x}Fe_xO$ films was not observed, implying complete incorporation of the Fe cations into the NiO lattice.

High-resolution SEM micrographs of the deposited Fe_2O_3 and $Ni_{1-x}Fe_xO$ films are presented in Figure 5.3. Plan and cross-sectional views of pure NiO (Figures 5.3(a) and (b), respectively) reveal that the film is composed of a dense packing of highly crystalline pyramidal columns ($d < 100$ nm), indicative of a cubic <100> growth direction in agreement with the corresponding XRD spectrum (Figure 5.1(c)). This structure is maintained at small Fe doping levels (i.e., x=0.05 shown in Figure 5.3(c)), but the columns and crystalline features become much smaller and appear to have a reduced texture at the intermediate composition of x=0.09 (Figure 5.3(d)). As shown in Figures 5.3(e)-(g), the morphological identity of the $Ni_{1-x}Fe_xO$ films changes significantly for $x > 0.09$, where the films are now dense and comprised of small, randomly-oriented grains. The observed reduction in crystallinity, grain size, and preferred growth direction for $Ni_{1-x}Fe_xO$ films with increasing Fe loading corroborates with the respective XRD data (Figures 5.1(c) and 5.2(a)). Similar to pure NiO, the as-deposited Fe_2O_3 film shown in Figure 5.3(h) is composed of relatively large, crystalline columns with highly faceted tops, indicative of a rhombohedral (110) texture. Finally, all deposited films were between 650 and 900 nm thick, where the variation in height can be attributed to slightly different total precursor fluxes used during growth and film packing densities.

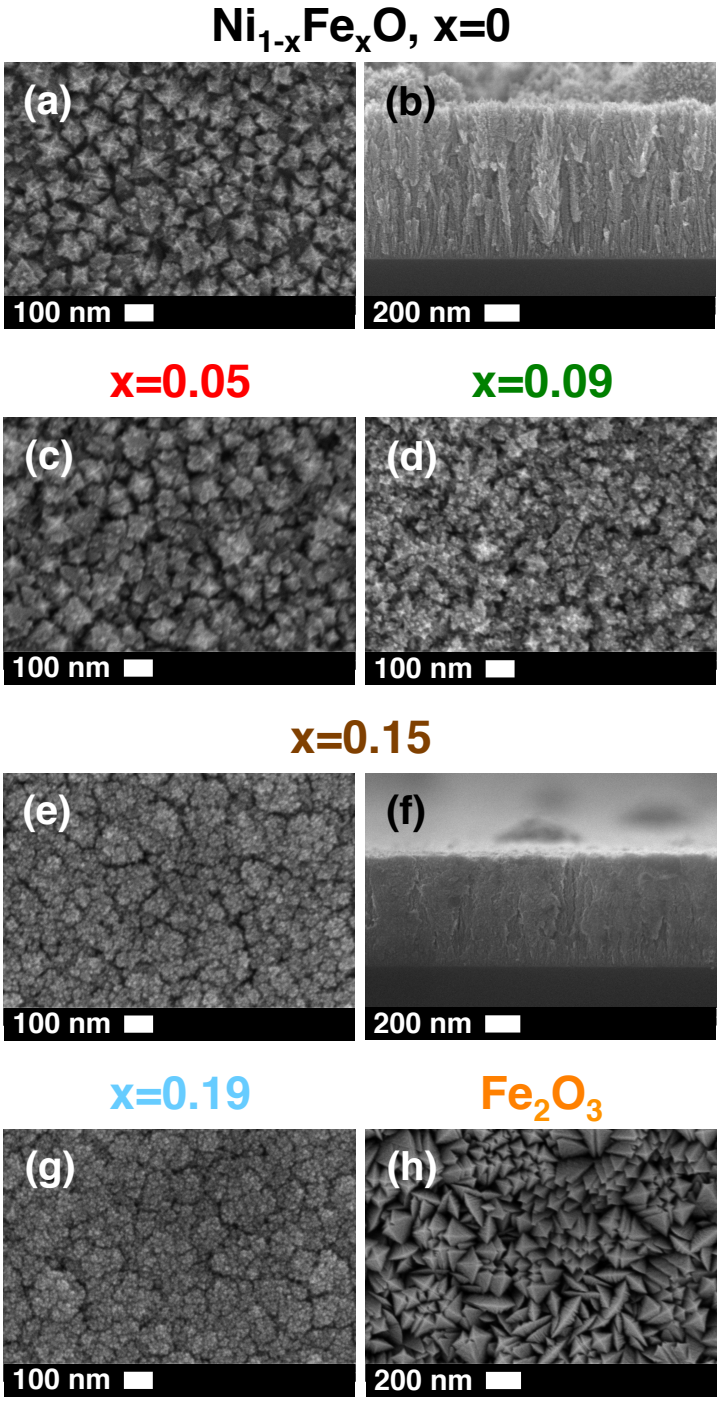

Figure 5.3: High-resolution SEM micrographs of microplasma jet-deposited $Ni_{1-x}Fe_xO$ and Fe_2O_3 films: (a,b) x=0, (c) x=0.05, (d) x=0.09, (e,f) x=0.15, (g) x=0.19, and (h) Fe_2O_3.

Thorough investigations of phase equilibria in the Ni-Fe-O system by Rhamdhani *et al.* revealed that the Fe solubility limit in rocksalt NiO is < 1 at% at temperatures < 600 K [36]. The ability to realize crystalline and metastable Fe-doped NiO rocksalt with a high solubility of Fe (up to 20% on a metals basis) on cold substrates using MP jets, where the temperature of the gas is close to room temperature, may be explained by selective heating of the nanoparticles in the hollow-cathode region of the plasma above their crystallization threshold temperature [36]. Recently, it has been shown that nanoparticles formed in low-temperature plasmas can achieve temperatures significantly higher than the overall gas temperature due to a number of energetic surface processes that include ion/e^- collisional heating, ion/e^- recombination, and association of atoms on the growing nanoparticle surface [37–40]. For example, Askari *et al.* demonstrated that Si nanoparticles < 10 nm formed in atmospheric-pressure microplasmas ($T_{gas} \sim 490$ K) can reach temperatures of ∼780 K from collisional heating [41]. The same mechanism is most likely at play here for the formation of crystalline and metastable rocksalt $Ni_{1-x}Fe_xO$ particles in the hollow-cathode. Additionally, bombardment of the growing film surface with charged species from the plasma jet afterglow could enhance surface diffusion explaining the formation of highly textured, crystalline films for pure NiO and Fe_2O_3. Interestingly, the film morphology of mixed $Ni_{1-x}Fe_xO$ films with $x > 0.09$ is reminiscent of ballistic aggregation, where nanoparticles or clusters from the gas phase hit and stick to the substrate surface due to low surface mobility, resulting in tapered columns with random crystallographic orientations (Figures 5.3(e)-(g)) [42–44]. This suggests that the incorporation of Fe into the crystalline NiO nanoparticles formed in the gas phase significantly influences film growth dynamics, where arriving $Ni_{1-x}Fe_xO$ nanoclusters and/or particles are unable to rearrange on the film surface to form long range crystalline grains.

5.3.2 Cyclic voltammetry measurements

Cyclic voltammetry (CV) measurements on pure NiO and Fe_2O_3 films were performed in 0.5 M KOH and are displayed in Figure 5.4(a). The NiO film shows behavior characteristic of NiO with cathodic and anodic peaks centered at about 0.3 and 0.4 V vs. Ag/AgCl using a 10 mV/s scan rate, respectively, followed by a large increase in current density from the evolution of oxygen with an onset potential of ∼0.51 V (η_{onset}=0.29). Although the as-deposited film is crystalline rocksalt NiO, it is well known that $Ni(OH)_2$ surface layers spontaneously form when NiO is exposed to alkaline electrolytes. As such, the measured anodic peak at 0.4 V vs. Ag/AgCl can be attributed to the oxidation of $Ni(OH)_2$ to NiOOH, and the corresponding cathodic peak at ∼0.3 V to the reduction of NiOOH back to $Ni(OH)_2$. In contrast, there were no Faradaic reactions on the Fe_2O_3 film for the potential range of the measurement, and the onset of oxygen evolution occurs at ∼0.6 V vs. Ag/AgCl (η_{onset}=0.38), significantly higher than NiO. The overpotential (η) measured at 10 mA/cm^2, which is the generally accepted figure of merit of OER catalysts, for the as-deposited NiO and Fe_2O_3 films was 360 and 470 mV, respectively. The relatively low overpotential measured here for NiO compares favorably with the literature [1, 4, 45].

Recently, Trotochaud *et al.* showed that the low intrinsic overpotentials of NiO measured in alkaline media are most likely due to the incorporation of Fe dopants from impure electrolytes [46]. They discovered that no significant OER currents were witnessed until $>$ 400 mV overpotential for $Ni(OH)_2$ catalysts cycled in purified KOH electrolytes, demonstrating that NiOOH is a poor catalyst for OER. Similar findings from other groups have verified that undoped NiO catalysts would become contaminated with trace quantities of Fe from unpurified electrolytes, resulting in a large enhancement in activity [47, 48]. To test if trace Fe impurities from the 0.5 M KOH electrolyte were incorporated

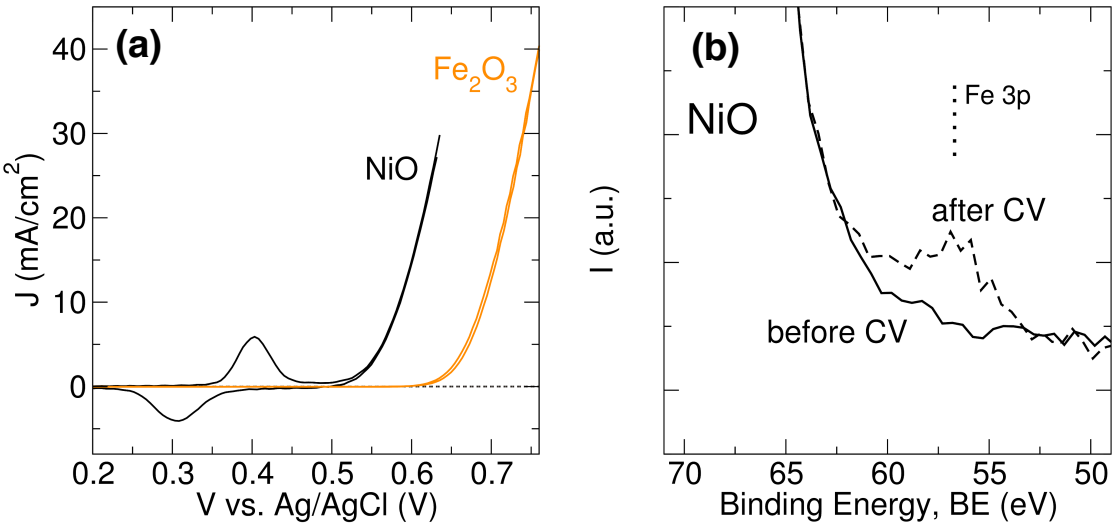

Figure 5.4: (a) Cyclic voltammograms (CV) of undoped NiO and Fe_2O_3 films on ITO in 0.5 M KOH at a 10 mV/s scan rate. The dotted line represents the CV scan of a blank ITO substrate. The anodic and cathodic peaks of NiO can be attributed to the $Ni(OH)_2 \longleftrightarrow NiOOH$ redox reaction. Current density based on geometric area (4×4 mm^2). (b) High resolution XPS scans of the Fe 3p peak show an increase in Fe on the NiO surface during electrochemical cycling in unpurified KOH.

into our NiO film during electrochemical testing, XPS scans of the Fe 3p photoelectron peak were taken both before and after electrochemical cycling and are shown in Figure 5.4(b). There was no detectable Fe signal in the as-deposited NiO film, but a small Fe 3p signal emerged after cycling in 0.5 M KOH, with an approximate surface Fe composition of 2% on a metals basis (i.e., Fe/Fe+Ni). As such, we cannot discount that the relatively low overpotentials seen here in the pure NiO film are influenced by the presence of Fe impurities on the catalyst surface.

CV curves of the $Ni_{1-x}Fe_xO$ films are plotted in Figure 5.5(a). As with the pure NiO film, only the redox reactions associated with $Ni(OH)_2 \longleftrightarrow NiOOH$ were observed, but the redox pair shifts to more anodic potentials with increasing Fe dopant concentrations. Additionally, the integrated area of the redox peaks, which is a measure of the total charge transferred, decreases with higher Fe loadings. These results suggest that the presence of Fe suppresses the oxidation of $Ni(OH)_2$ to NiOOH, and that the Fe dopants are displacing

Ni surface sites in the rocksalt structure, resulting in fewer electrochemically exposed Ni atoms to undergo oxidation and reduction reactions. Figure 5.5(b) summarizes the measured η at 10 mA/cm^2 for $Ni_{1-x}Fe_xO$ films. There is a significant decrease in η from 360 mV for the as-deposited, undoped NiO film to 320 mV for $Ni_{0.95}Fe_{0.05}O$, but the overpotential remains relatively constant for Fe compositions between 5 and 19% (i.e., between 310 and 325 mV). Louie and Bell saw a similar result in their electrodeposited Ni-Fe catalysts, albeit at a different composition range, where catalytic activity increased with Fe composition up to about 20% (on a metals basis), remained relatively constant up to 50% Fe, and then decreased again with even higher Fe concentrations [49].

The turnover frequency (TOF) was calculated at η=300 and 350 mV to assess the catalytic activity of the $Ni_{1-x}Fe_xO$ films normalized by the number of electrochemically accessible Ni atoms. Although the catalytically active center may be Fe in our $Ni_{1-x}Fe_xO$ films, it is still worthwhile to scale against Ni, as it allows for direct comparison between

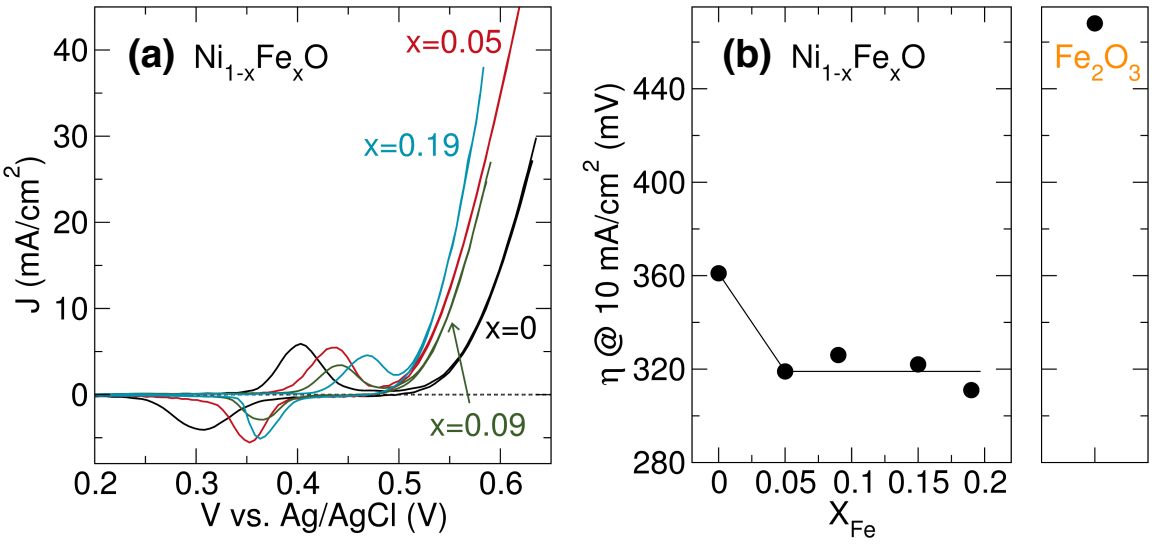

Figure 5.5: (a) Cyclic voltammograms (CV) of $Ni_{1-x}Fe_xO$ films on ITO in 0.5 M KOH at a 10 mV/s scan rate. The dotted line represents the CV scan of a blank ITO substrate. The anodic and cathodic peaks of $Ni_{1-x}Fe_xO$ films can be attributed to the $Ni(OH)_2 \longleftrightarrow NiOOH$ redox reaction. (b) Overpotential (η) measured at 10 mA/cm^2 for different $Ni_{1-x}Fe_xO$ films. Lines are only meant to guide the eye.

catalysts and of the effectiveness of the NiO surface at catalyzing OER. More specifically, the TOFs of the $Ni_{1-x}Fe_xO$ films displayed in Figure 5.6(a) were calculated as the number of O_2 molecules generated per electrochemically accessible Ni site, where the number of Ni sites was estimated from the charge obtained from integration of the cathodic going reduction peak assuming a $1e^-$ transfer per Ni site. The TOFs for pure NiO were calculated as 0.01 and 0.07 s^{-1} at η=300 and 350 mV, respectively, which is comparable to and often better than other reported NiO electrocatalysts [45, 48, 50]. The TOF increased with Fe doping levels, with the x=0.19 sample having the highest values of 0.10 and 0.48 s^{-1} at η=300 and 350 mV, respectively. Published TOF values for Ni-Fe catalysts have been shown to range anywhere from ∼0.01 to 90, and depend strongly on the method used to estimate the number of catalytically active Ni sites, which has been discussed in great detail in the literature [3, 49]. As such, this measurement should be taken with great care when comparing to other experimental efforts, but is well suited for comparing activity trends between similar catalysts in a single study. As seen in Figure 5.6(a), the TOF measured at η=350 mV increases sharply for Fe levels up to x=0.1, followed by a marginal improvement from x=0.1 to 0.19. Although the measured overpotentials do not vary much for the Fe containing NiO films, the incorporation of Fe up to 19% improves the catalytic activity of the NiO surface. Figure 5.6(b) displays the Tafel plots for all $Ni_{1-x}Fe_xO$ films. The Tafel slopes obtained at low current densities (<1 mA/cm^2) for Fe-doped samples (20–25 mV/dec) were slightly lower than that for the undoped NiO film (30 mV/dec), and compare well with other Ni-Fe oxide electrocatalysts, where Tafel slopes of 30–40 mV/dec are commonly observed [3, 18, 48, 49, 51–53].

There are a few important points to take into consideration when assessing the catalytic activity of our $Ni_{1-x}Fe_xO$ films. First, there is a significant change in film morphology and a decrease in grain size and crystallinity with increasing Fe concentration, making it difficult to completely isolate the effects of Fe dopants on activity. Moreover, all

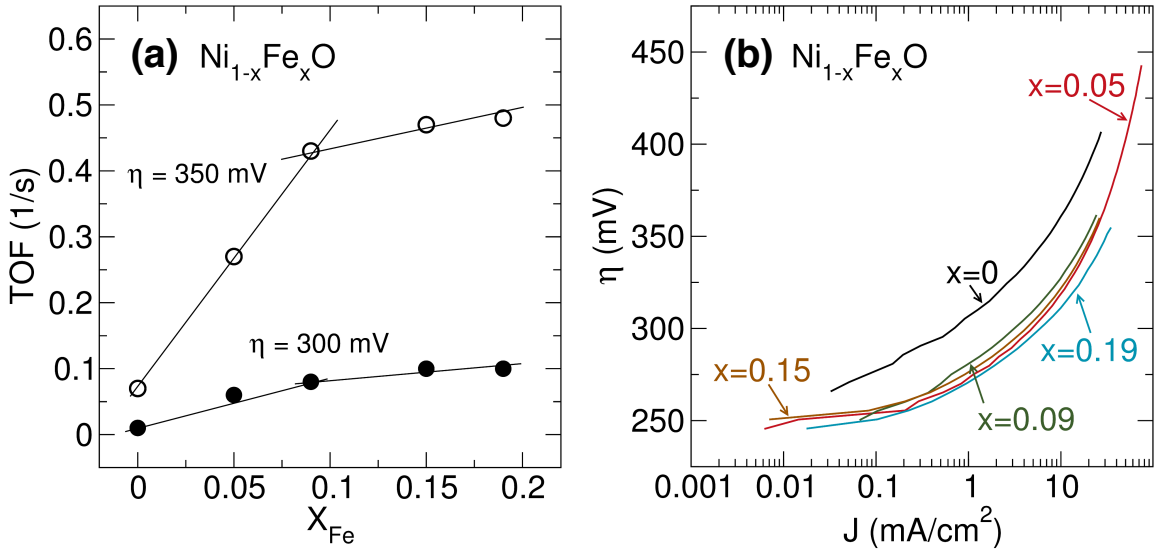

Figure 5.6: Kinetic analysis of $Ni_{1-x}Fe_xO$ films from the CV scans in Figure 5.5(a): (a) turnover frequency (TOF) calculated at η=300 and 350 mV, where the lines are only meant to guide the eye, and (b) Tafel plots, where both NiO (∼30 mV/dec) and $Ni_{1-x}Fe_xO$ (∼20-25 mV/dec) display relatively low Tafel slopes at low current densities.

CV measurements were performed with a static working electrode where mass-transport phenomena are certainly influencing the observed activity, which would *underrepresent* the actual activity of our catalysts. To exacerbate the problem, higher activity catalysts would be more impacted than lower activity catalysts as was shown by Louie and Bell for electrodeposited Ni-Fe thin films using a rotating working electrode [49]. Finally, the film thicknesses presented here of ∼600–950 nm are much thicker than what is usual for OER catalysts (< 100 nm), which could lead to a non negligible voltage drop across the thickness of the oxide films and a corresponding increase in measured overpotentials. The magnitude of this voltage drop is not expected to be constant among all films due to differing film thicknesses and Fe concentrations, where it has been shown that higher Fe loadings lead to better electrical conductivity in Ni-Fe oxide electrodes [46]. It is worth noting that our oxide films are relatively conductive as evidenced by the high-resolution SEM images obtained without coating the surface with a conductive contact.

5.3.3 Catalyst stability testing

The electrochemical stability of $Ni_{1-x}Fe_xO$ films was tested using chronopotentiometry at OER relevant conditions (i.e., 2 hrs @ 10 mA/cm^2), which is shown in Figure 5.7(a). The potential needed to maintain a constant current density of 10 mA/cm^2 decreased with time for the pure NiO film, and increased slightly for all Fe-doped NiO samples. The decrease in potential signifies an improvement in catalytic activity for the NiO film, where in the literature, this has been attributed to the transformation of the surface γ-NiOOH phase to the more crystalline and catalytically active β-phase when aged in alkaline electrolytes [54–56]. However, Trotochaud *et al.* and Klaus *et al.* have recently shown that β-NiOOH, when cycled in purified electrolytes, is less active than γ-NiOOH, and that previous reports of highly active β-NiOOH may be rationalized by the incorporation of trace Fe impurities from the electrolyte [46, 47]. As discussed above and shown in Figure 5.4(b), Fe uptake onto the pristine NiO surface from the KOH electrolyte may explain the improvement in catalytic activity seen here. For the Fe-doped NiO films, the slight increase in potential with time may be due to mass-transport phenomena, where oxygen bubbles forming on the catalyst surface during OER block catalytically active sites, requiring higher potentials to realize a constant current density. This hypothesis was tested on the x=0.09 and 0.15 samples by stopping the measurement after 1 hour to remove any accumulated oxygen bubbles before continuing the chronopotentiometry test. After interruption, the voltage drops down to its original value from the start of the measurement (Figure 5.7(a)), confirming that the increasing voltage with time is due to blocked catalytic sites and not from catalyst deactivation. CV curves after OER polarization were obtained to assess changes in the electrochemical behavior of the catalysts. Figure 5.7(b) displays CV curves measured both before and after chronopotentiometry testing for pure NiO and for the x=0.15 film. The redox peak area increases for both

samples, which is most likely due to an increase in surface area from restructuring of the film surface and/or conversion of the underlying $Ni_{1-x}Fe_xO$ film to $Ni_{1-x}Fe_x(OH)_2$. The increase in activity of the pure NiO film after OER polarization can be rationalized from the incorporation of trace Fe from the electrolyte, as opposed to an increase in surface area from restructuring. Conversely, the x=0.15 sample has a negligible change in activity. Finally, the structural stability of the catalysts after OER polarization was assessed via SEM, and the images for the x=0 and 0.15 samples are shown in Figures 5.7(c) and (d), respectively. There is evidence of local ripening of surfaces from electrochemical cycling, resulting in smooth facets, but the macroscopic morphology of the films was unaltered. Moreover, there was no flaking or peeling of the $Ni_{1-x}Fe_xO$ films from the ITO substrate. These results demonstrate that Fe-doped NiO films deposited via microplasmas are mechanically and electrochemically robust for OER.

High-resolution XPS spectra of the Ni 2p and O 1s photoelectron lines were collected before and after chronopotentiometry measurements to assess any chemical changes on the $Ni_{1-x}Fe_xO$ film surface. Figure 5.8(a) displays the Ni 2p photoelectron lines and the corresponding shake-up peaks from unpaired electrons for the as-deposited $Ni_{1-x}Fe_xO$ films. Quantitative analysis of the Ni 2p envelope in this case is complex because of the overlap between Ni 3d and O 2p electrons, resulting in many multiplet structures and shakeup satellites [57]. An NiO powder sample (Sigma Aldrich) was used as a reference for the Ni^{2+} oxidation state, and has been presented in Figure 5.8(a). The Ni $2p^{3/2}$ portion of the Ni 2p spectrum for the NiO powder is manifested as a doublet at a BE of ~853.8 and 855.8 eV, with the former having a higher peak intensity. This same doublet structure appears in all microplasma deposited $Ni_{1-x}Fe_xO$ films, but the relative peak intensity of the higher BE peak with respect to the lower BE peak is greater than that for the NiO reference sample. It is likely that the increase in intensity at 855.8 eV is from the presence of $Ni_{1-x}Fe_x(OH)_2$, which has been shown to have its largest peak contribution

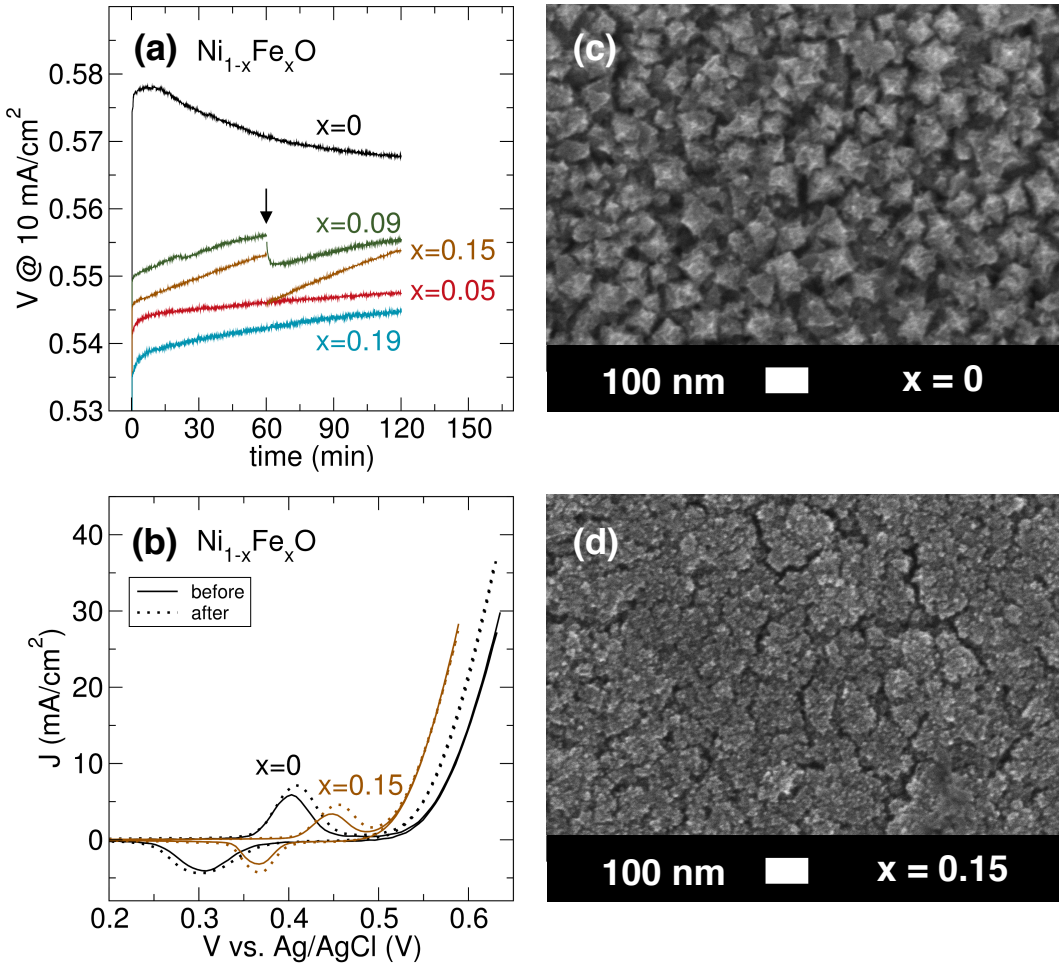

Figure 5.7: (a) Chronopotentiometry results where the $Ni_{1-x}Fe_xO$ films were held at a constant current density of 10 mA/cm^2 for 2 hours. The discontinuity for the x=0.09 and 0.15 films (arrow) is from current interrupt, where oxygen bubbles were removed from the film surface after 1 hour to verify that the voltage creep was due to blocked catalytic sites and not from catalyst deactivation. (b) CV curves for the x=0 and 0.15 films measured before and after OER polarization, illustrating that Fe-doped NiO films are electrochemically stable. (c) and (d) High-resolution SEM micrographs of x=0 and 0.15 films after chronopotentiometry measurements, respectively, demonstrating structural and mechanical stability at OER conditions. Compare with pristine film morphology in Figures 5.3(e) and (f).

at 855.7 eV [58]. Moreover, the absence of the major Ni^{3+} peak signature at ~856.5 eV, suggests that there are no $Ni_{1-x}Fe_xOOH$ or Ni_2O_3 phases present [58]. Finally, doping Fe into the NiO structure appears to have no effect on the shape of the Ni 2p photoelectron line.

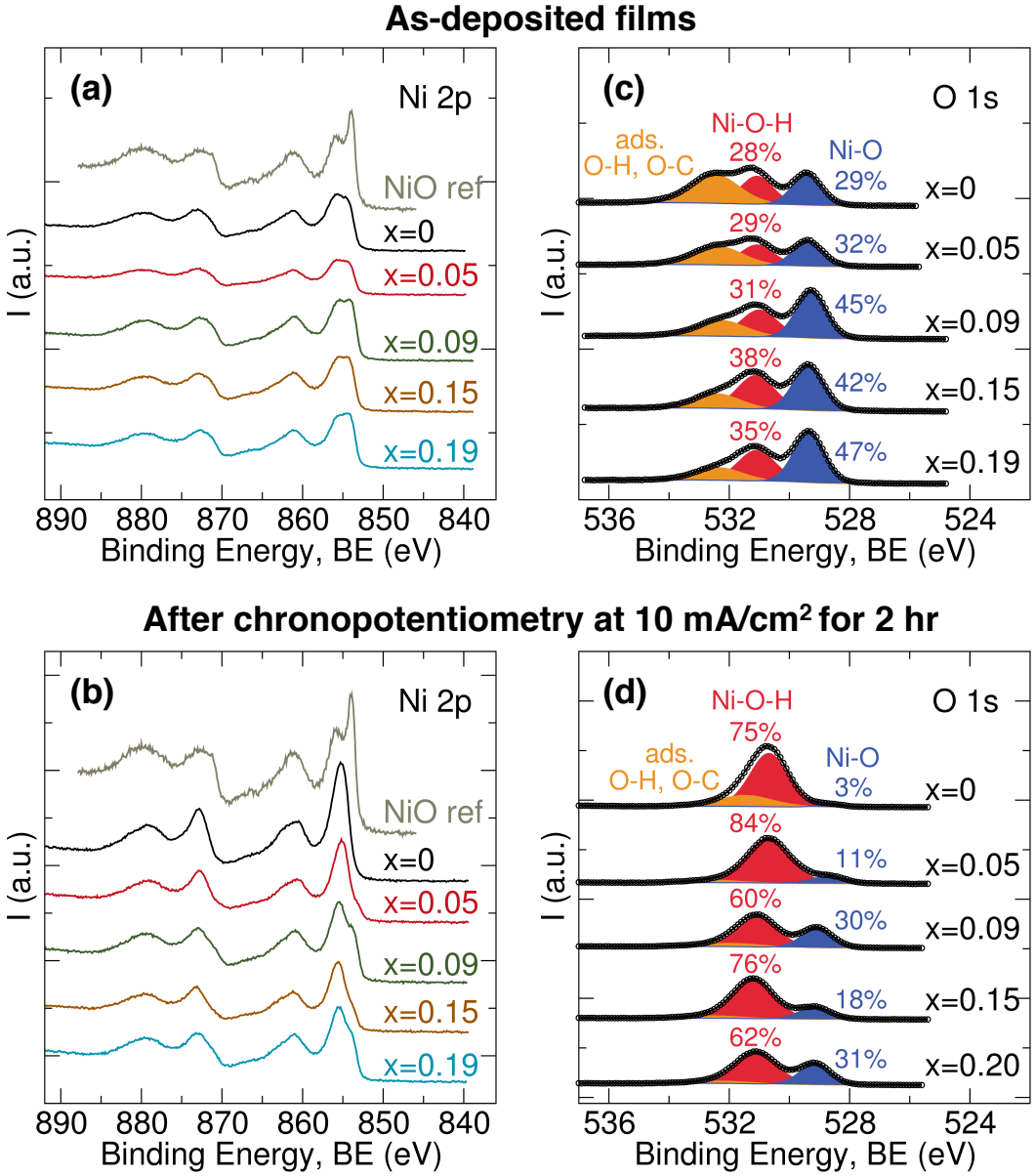

Figure 5.8: High-resolution XPS spectra of the (a,c) pristine, as-deposited $Ni_{1-x}Fe_xO$ films and (b,d) after polarization at OER conditions (10 mA/cm^2 for 2 hours): (a,b) Ni 2p photoelectron line, where an NiO powder was used as a reference (grey, top curve), and (c,d) O 1s photoelectron line, where the fitted peaks at 529.3 (blue), 531 (red), and 532.5 (orange) correspond to the Ni-O, Ni-O-H, and adsorbed O-H and O-C bonding states, respectively. The relative quantities of these chemical states are labeled above each peak.

Figure 5.8(b) shows the Ni 2p spectra for the $Ni_{1-x}Fe_xO$ films after exposure to OER conditions (i.e., 2 hours @ 10 mA/cm^2). The Ni $2p^{3/2}$ peak of the pure NiO film is dominated by $Ni(OH)_2$ character, with a single peak at 855.8 eV, and no indication of the NiO feature at 853.8 eV, suggesting that the entire NiO surface has transformed to $Ni(OH)_2$ during electrochemical testing in KOH electrolyte. Interestingly, the peak structure at 853.8 eV is observed in all of the Fe-doped NiO samples, and its intensity, relative to the higher BE feature, increases with Fe. Moreover, the intensity ratio of the higher-to-lower BE peaks is much greater than that for the pristine, as-deposited films. The latter two observations imply that the $Ni_{1-x}Fe_xO$ films are more hydrated after OER polarization with the degree of hydration dependent on Fe composition, where higher Fe content hampers the hydration of $Ni_{1-x}Fe_xO$ to $Ni_{1-x}Fe_x(OH)_2$. Additionally, the characteristic signatures of Ni^{3+} at higher BE ($\sim$856.5 eV) are not present, implying that the $Ni_{1-x}Fe_xOOH$ surface phase present at OER potentials reduces entirely to $Ni_{1-x}Fe_x(OH)_2$ when the potential is removed.

High resolution scans of the O 1s peak can give further insight into the bonding environment of the $Ni_{1-x}Fe_xO$ film surfaces, as well as the degree of hydration. Figure 5.8(c) clearly shows three distinct bonding states of O in the as-deposited films, where the fitted peaks at 529.3 (blue), 531 (red), and 532.5 eV (yellow) correspond to the Ni-O, Ni-O-H, and adsorbed O-H and O-C bonding states. In all films, the surface is composed of Ni-O from NiO, and to a lesser extent, Ni-O-H from $Ni(OH)_2$, in good agreement with the Ni 2p spectra. After OER polarization, the O 1s peak is dominated by Ni-O-H at 531 eV, with a small contribution from Ni-O at 529.3, and negligible signal from adsorbed species at 532.5 eV (Figure 5.8(d)). In the case of pure NiO, there is a negligible signal of the Ni-O phase, verifying that the film surface has become entirely hydrated $Ni(OH)_2$. Incorporation of Fe into the NiO structure appears to suppress the hydration of NiO to $Ni(OH)_2$ (Figure 5.8(d)). This was also observed by Nardi *et al.* in atomic layer

deposited NiO films tested in Fe-rich KOH electrolyte [48]. Both the Ni 2p and O 1s XPS spectra reveal that the surface of the as-deposited $Ni_{1-x}Fe_xO$ films is a mixture of both $Ni_{1-x}Fe_xO$ and $Ni_{1-x}Fe_x(OH)_2$ phases, which become predominately $Ni_{1-x}Fe_x(OH)_2$ with small quantities of $Ni_{1-x}Fe_xO$ upon exposure to OER potentials. The increasing Fe content in the NiO films acts to suppress the hydration of $Ni_{1-x}Fe_xO$ to $Ni_{1-x}Fe_x(OH)_2$.

5.4 Conclusions

Nanostructured Fe_2O_3, NiO, and $Ni_{1-x}Fe_xO$ films with high-surface area and electrochemical OER activity were deposited on ITO substrates using flow-stabilized microplasma jets. Pure Fe_2O_3 and NiO films formed as a dense packing of highly crystalline and textured columnar structures with relatively large crystal sizes (63 and 16 nm, respectively). For the as-deposited $Ni_{1-x}Fe_xO$ films, Fe^{2+} was observed to fully incorporate into the rocksalt lattice, resulting in a lattice dilation of $\sim 6\%$ with 20 at% measured on a metals basis. The crystallinity and grain size decreased with increasing Fe content, where the film morphology transitioned from oriented crystalline columns to a dense packing of small, randomly oriented grains (< 10 nm) at $x > 0.09$. The relatively low overpotentials measured for the undoped NiO sample may be due to incorporation of trace amounts of Fe from the unpurified KOH electrolyte. It was seen that intentionally doping NiO with Fe resulted in lower overpotentials; however, the level of Fe doping (5-19%) did not appear to have a significant effect. This finding may be due to mass transport phenomena, variations in electrical conductivity in the different $Ni_{1-x}Fe_xO$ films, as well as a change in morphology and reduction in crystallinity and grain size with increasing Fe incorporation into the NiO lattice. In contrast, the TOF of the $Ni_{1-x}Fe_xO$ catalysts increased with Fe content from 0.07 s^{-1} for NiO to 0.48 s^{-1} for $Ni_{0.81}Fe_{0.19}O$ at η=350 mV, leading to an improvement in catalytic activity of the NiO surface. XPS and SEM anal-

ysis after chronopotentiometry and electrochemical cycling verified that the catalysts are chemically and mechanically stable during operation at OER conditions. Moreover, this chapter demonstrates that microplasmas offer a general, one-step approach to deposit conformal coatings of oxide-based catalysts with high activities for OER.

References

[1] C. C. McCrory, S. Jung, J. C. Peters, and T. F. Jaramillo, "Benchmarking heterogeneous electrocatalysts for the oxygen evolution reaction," *J. Am. Chem. Soc.*, vol. 135, no. 45, pp. 16977–16987, 2013.

[2] J. Y. Chen, J. T. Miller, J. B. Gerken, and S. S. Stahl, "Inverse spinel $NiFeAlO_4$ as a highly active oxygen evolution electrocatalyst: promotion of activity by a redox-inert metal ion," *Energy Environ. Sci.*, vol. 7, no. 4, pp. 1382–1386, 2014.

[3] K. Fominykh, P. Chernev, I. Zaharieva, J. Sicklinger, G. Stefanic, M. Döblinger, A. Müller, A. Pokharel, S. Böcklein, C. Scheu, *et al.*, "Iron-doped nickel oxide nanocrystals as highly efficient electrocatalysts for alkaline water splitting," *ACS Nano*, vol. 9, no. 5, pp. 5180–5188, 2015.

[4] K. Fominykh, J. M. Feckl, J. Sicklinger, M. Döblinger, S. Böcklein, J. Ziegler, L. Peter, J. Rathousky, E.-W. Scheidt, T. Bein, *et al.*, "Ultrasmall dispersible crystalline nickel oxide nanoparticles as high-performance catalysts for electrochemical water splitting," *Adv. Funct. Mater.*, vol. 24, no. 21, pp. 3123–3129, 2014.

[5] M. Görlin, M. Gliech, J. F. de Araújo, S. Dresp, A. Bergmann, and P. Strasser, "Dynamical changes of a Ni-Fe oxide water splitting catalyst investigated at different pH," *Catal. Today*, vol. 262, pp. 65–73, 2016.

[6] J. Qi, W. Zhang, R. Xiang, K. Liu, H.-Y. Wang, M. Chen, Y. Han, and R. Cao, "Porous nickel–iron oxide as a highly efficient electrocatalyst for oxygen evolution reaction," *Adv. Sci.*, vol. 2, no. 10, p. 1500199, 2015.

[7] J. Ji, L. L. Zhang, H. Ji, Y. Li, X. Zhao, X. Bai, X. Fan, F. Zhang, and R. S. Ruoff, "Nanoporous $Ni(OH)_2$ thin film on 3D ultrathin-graphite foam for asymmetric supercapacitor," *ACS Nano*, vol. 7, no. 7, pp. 6237–6243, 2013.

[8] D. Mariotti and R. M. Sankaran, "Microplasmas for nanomaterials synthesis," *J. Phys. D: Appl. Phys.*, vol. 43, no. 32, p. 323001, 2010.

[9] D. Mariotti and R. M. Sankaran, "Perspectives on atmospheric-pressure plasmas for nanofabrication," *J. Phys. D: Appl. Phys.*, vol. 44, no. 17, p. 174023, 2011.

[10] T. L. Koh, E. C. O'Hara, and M. J. Gordon, "Microplasma-based synthesis of vertically aligned metal oxide nanostructures," *Nanotechnology*, vol. 23, no. 42, p. 425603, 2012.

[11] T. Koh, E. O'Hara, and M. Gordon, "Growth of nanostructured CuO thin films via microplasma-assisted, reactive chemical vapor deposition at high pressures," *J. Cryst. Growth*, vol. 363, pp. 69–75, 2013.

[12] T. L. Koh and M. J. Gordon, "Spray deposition of nanostructured metal films using hydrodynamically stabilized, high pressure microplasmas," *J. Vac. Sci. Technol. A*, vol. 31, no. 6, p. 061312, 2013.

[13] A. C. Pebley, A. Peek, T. M. Pollock, and M. J. Gordon, "Microplasma-based growth of biphasic $NiFe_2O_4$/NiO nanogranular films for exchange bias applications," *Chem. Mater.*, vol. 26, no. 20, pp. 6026–6032, 2014.

[14] A. C. Pebley, P. E. Fuks, T. M. Pollock, and M. J. Gordon, "Exchange bias and spin glass behavior in biphasic $NiFe_2O_4$/NiO thin films," *J. Magn. Magn. Mater.*, vol. 419, pp. 29–36, 2016.

[15] K. E. Mackie, A. C. Pebley, M. M. Butala, J. Zhang, G. D. Stucky, and M. J. Gordon, "Microplasmas for direct, substrate-independent deposition of nanostructured metal oxides," *Appl. Phys. Lett.*, vol. 109, no. 3, p. 033110, 2016.

[16] A. Kumar, P. A. Lin, A. Xue, B. Hao, Y. K. Yap, and R. M. Sankaran, "Formation of nanodiamonds at near-ambient conditions via microplasma dissociation of ethanol vapour," *Nat. Commun.*, vol. 4, p. 2618, 2013.

[17] D. Mariotti, S. Mitra, and V. Švrček, "Surface-engineered silicon nanocrystals," *Nanoscale*, vol. 5, no. 4, pp. 1385–1398, 2013.

[18] M. Gong, Y. Li, H. Wang, Y. Liang, J. Z. Wu, J. Zhou, J. Wang, T. Regier, F. Wei, H. Dai, *et al.*, "An advanced Ni-Fe layered double hydroxide electrocatalyst for water oxidation," *J. Am. Chem. Soc.*, vol. 135, no. 23, pp. 8452–8455, 2013.

[19] J. Luo, J.-H. Im, M. T. Mayer, M. Schreier, M. K. Nazeeruddin, N.-G. Park, S. D. Tilley, H. J. Fan, and M. Grätzel, "Water photolysis at 12.3% efficiency via perovskite photovoltaics and earth-abundant catalysts," *Science*, vol. 345, no. 6204, pp. 1593–1596, 2014.

[20] Q. Luo, M. Peng, X. Sun, Y. Luo, and A. M. Asiri, "Efficient electrochemical water splitting catalyzed by electrodeposited NiFe nanosheets film," *Int. J. Hydrogen Energy*, vol. 41, no. 21, pp. 8785–8792, 2016.

[21] X. Cui, P. Ren, D. Deng, J. Deng, and X. Bao, "Single layer graphene encapsulating non-precious metals as high-performance electrocatalysts for water oxidation," *Energy Environ. Sci.*, vol. 9, no. 1, pp. 123–129, 2016.

[22] D. Wang, F. Watanabe, and W. Zhao, "One-pot growth of 3D reduced graphene oxide foams embedded with NiFe oxide nanocatalysts for oxygen evolution reaction," *J. Electrochem. Soc.*, vol. 163, no. 11, pp. F3158–F3163, 2016.

[23] G. Kresse and J. Hafner, "Ab initio molecular dynamics for liquid metals," *Phys. Rev. B*, vol. 47, no. 1, p. 558, 1993.

[24] G. Kresse and J. Furthmüller, "Efficient iterative schemes for ab initio total-energy calculations using a plane-wave basis set," *Phys. Rev. B*, vol. 54, no. 16, p. 11169, 1996.

[25] G. Kresse and J. Furthmüller, "Efficiency of ab-initio total energy calculations for metals and semiconductors using a plane-wave basis set," *Comput. Mater. Sci.*, vol. 6, no. 1, pp. 15–50, 1996.

[26] G. Kresse and J. Hafner, "Ab initio molecular-dynamics simulation of the liquid-metal–amorphous-semiconductor transition in germanium," *Phys. Rev. B*, vol. 49, no. 20, p. 14251, 1994.

[27] J. P. Perdew, A. Ruzsinszky, G. I. Csonka, O. A. Vydrov, G. E. Scuseria, L. A. Constantin, X. Zhou, and K. Burke, "Restoring the density-gradient expansion for exchange in solids and surfaces," *Phys. Rev. Lett.*, vol. 100, no. 13, p. 136406, 2008.

[28] P. E. Blöchl, "Projector augmented-wave method," *Phys. Rev. B*, vol. 50, no. 24, p. 17953, 1994.

[29] G. Kresse and D. Joubert, "From ultrasoft pseudopotentials to the projector augmented-wave method," *Phys. Rev. B*, vol. 59, no. 3, p. 1758, 1999.

[30] B. Puchala and A. Van der Ven, "Thermodynamics of the Zr-O system from first-principles calculations," *Phys. Rev. B*, vol. 88, no. 9, p. 094108, 2013.

[31] J. C. Thomas and A. Van der Ven, "Finite-temperature properties of strongly anharmonic and mechanically unstable crystal phases from first principles," *Phys. Rev. B*, vol. 88, no. 21, p. 214111, 2013.

[32] A. Van der Ven, J. Thomas, Q. Xu, and J. Bhattacharya, "Linking the electronic structure of solids to their thermodynamic and kinetic properties," *Math. Comput. Simul.*, vol. 80, no. 7, pp. 1393–1410, 2010.

[33] B. Puchala, M. Radin, N. S. H. Gunda, J. Goiri, E. Decolvenaere, A. R. Natarajan, and J. C. Thomas, "Casmcode: v0.2.0," 2016.

[34] D. A. Corrigan and S. L. Knight, "Electrochemical and spectroscopic evidence on the participation of quadrivalent nickel in the nickel hydroxide redox reaction," *J. Electrochem. Soc.*, vol. 136, no. 3, pp. 613–619, 1989.

[35] R. t. Shannon, "Revised effective ionic radii and systematic studies of interatomic distances in halides and chalcogenides," *Acta Cryst. A*, vol. 32, no. 5, pp. 751–767, 1976.

[36] M. Rhamdhani, P. Hayes, and E. Jak, "Subsolidus phase equilibria of the Fe-Ni-O system," *Metall. Mater. Trans. B*, vol. 39, no. 5, pp. 690–701, 2008.

[37] L. Mangolini and U. Kortshagen, "Selective nanoparticle heating: another form of nonequilibrium in dusty plasmas," *Phys. Rev. E*, vol. 79, no. 2, p. 026405, 2009.

[38] N. Kramer, E. Aydil, and U. Kortshagen, "Requirements for plasma synthesis of nanocrystals at atmospheric pressures," *J. Phys. D: Appl. Phys.*, vol. 48, no. 3, p. 035205, 2015.

[39] T. Lopez and L. Mangolini, "On the nucleation and crystallization of nanoparticles in continuous-flow nonthermal plasma reactors," *J. Vac. Sci. Technol. B*, vol. 32, no. 6, p. 061802, 2014.

[40] H. Maurer and H. Kersten, "On the heating of nano-and microparticles in process plasmas," *J. Phys. D: Appl. Phys.*, vol. 44, no. 17, p. 174029, 2011.

[41] S. Askari, I. Levchenko, K. Ostrikov, P. Maguire, and D. Mariotti, "Crystalline Si nanoparticles below crystallization threshold: effects of collisional heating in non-thermal atmospheric-pressure microplasmas," *Appl. Phys. Lett.*, vol. 104, no. 16, p. 163103, 2014.

[42] D. Bensimon, B. Shraiman, and S. Liang, "On the ballistic model of aggregation," *Phys. Lett. A*, vol. 102, no. 5, pp. 238–240, 1984.

[43] P. Ramanlal and L. Sander, "Theory of ballistic aggregation," *Phys. Rev. Lett.*, vol. 54, no. 16, p. 1828, 1985.

[44] D.-X. Ye and T.-M. Lu, "Fanlike aggregations on seeds by parallel ballistic flux: Experimental results and monte carlo simulations of the growth of three-dimensional si structures," *Phys. Rev. B*, vol. 75, no. 11, p. 115420, 2007.

[45] M. S. Burke, S. Zou, L. J. Enman, J. E. Kellon, C. A. Gabor, E. Pledger, and S. W. Boettcher, "Revised oxygen evolution reaction activity trends for first-row transition-metal (oxy) hydroxides in alkaline media," *J. Phys. Chem. Lett.*, vol. 6, no. 18, pp. 3737–3742, 2015.

[46] L. Trotochaud, S. L. Young, J. K. Ranney, and S. W. Boettcher, "Nickel–iron oxyhydroxide oxygen-evolution electrocatalysts: the role of intentional and incidental iron incorporation," *J. Am. Chem. Soc.*, vol. 136, no. 18, pp. 6744–6753, 2014.

[47] S. Klaus, Y. Cai, M. W. Louie, L. Trotochaud, and A. T. Bell, "Effects of fe electrolyte impurities on $Ni(OH)_2$/NiOOH structure and oxygen evolution activity," *J. Phys. Chem. C*, vol. 119, no. 13, pp. 7243–7254, 2015.

[48] K. L. Nardi, N. Yang, C. F. Dickens, A. L. Strickler, and S. F. Bent, "Creating highly active atomic layer deposited NiO electrocatalysts for the oxygen evolution reaction," *Adv. Energy Mater.*, vol. 5, no. 17, pp. 1500412–1500421, 2015.

[49] M. W. Louie and A. T. Bell, "An investigation of thin-film Ni–Fe oxide catalysts for the electrochemical evolution of oxygen," *J. Am. Chem. Soc.*, vol. 135, no. 33, pp. 12329–12337, 2013.

[50] I. Godwin and M. Lyons, "Enhanced oxygen evolution at hydrous nickel oxide electrodes via electrochemical ageing in alkaline solution," *Electrochem. Commun.*, vol. 32, pp. 39–42, 2013.

[51] A. S. Batchellor and S. W. Boettcher, "Pulse-electrodeposited Ni–Fe (oxy) hydroxide oxygen evolution electrocatalysts with high geometric and intrinsic activities at large mass loadings," *ACS Catal.*, vol. 5, no. 11, pp. 6680–6689, 2015.

[52] D. A. Corrigan, "The catalysis of the oxygen evolution reaction by iron impurities in thin film nickel oxide electrodes," *J. Electrochem. Soc.*, vol. 134, no. 2, pp. 377–384, 1987.

[53] Y. Qiu, L. Xin, and W. Li, "Electrocatalytic oxygen evolution over supported small amorphous Ni–Fe nanoparticles in alkaline electrolyte," *Langmuir*, vol. 30, no. 26, pp. 7893–7901, 2014.

[54] M. G. De Chialvo and A. Chialvo, "Oxygen evolution reaction on thick hydrous nickel oxide electrodes," *Electrochim. Acta*, vol. 33, no. 6, pp. 825–830, 1988.

[55] A. Singh, S. L. Chang, R. K. Hocking, U. Bach, and L. Spiccia, "Highly active nickel oxide water oxidation catalysts deposited from molecular complexes," *Energy Environ. Sci.*, vol. 6, no. 2, pp. 579–586, 2013.

[56] B. S. Yeo and A. T. Bell, "In situ raman study of nickel oxide and gold-supported nickel oxide catalysts for the electrochemical evolution of oxygen," *J. Phys. Chem. C*, vol. 116, no. 15, pp. 8394–8400, 2012.

[57] A. P. Grosvenor, M. C. Biesinger, R. S. C. Smart, and N. S. McIntyre, "New interpretations of XPS spectra of nickel metal and oxides," *Surf. Sci.*, vol. 600, no. 9, pp. 1771–1779, 2006.

[58] M. C. Biesinger, B. P. Payne, L. W. Lau, A. Gerson, and R. S. C. Smart, "X-ray photoelectron spectroscopic chemical state quantification of mixed nickel metal, oxide and hydroxide systems," *Surf. Interface Anal.*, vol. 41, no. 4, pp. 324–332, 2009.

Chapter 6

Future Work and Conclusions

6.1 Summary

This dissertation focused on microplasma (MP) jet deposition of a variety of Ni-Fe oxides, ranging from biphasic FiM/FM $NiFe_2O_4$/NiO to metastable Fe-doped NiO films for fundamental studies of magnetic exchange bias and electrocatalysis, respectively. The effects of MP operating parameters (i.e., precursor composition, flux, *in-situ* substrate heating, and post-deposition annealing) on film morphology, composition, chemical phase, crystallinity, and interfacial and surface densities were studied in detail. Moreover, how these physiochemical properties influence the resulting magnetic and electrochemical properties of the Ni-Fe oxide films were examined.

In chapter 3, $NiFe_2O_4$/NiO biphasic films of varying composition were realized using MP jet deposition and post-deposition annealing. The exchange bias effect (H_E) and enhanced coercivity (H_C) were seen in all biphasic films at cryogenic (20 K) and room temperatures (300 K) after field cooling through the Néel temperature of NiO. These values increased with Ni composition, and were rationalized as due to increased $NiFe_2O_4$/NiO interfacial density. This is the first time exchange bias has been observed

in the $NiFe_2O_4$/NiO nanogranular system at room temperature. Other groups have witnessed spin glass coupling in solution-based synthesis of $NiFe_2O_4$/NiO, which does not persist at temperatures above ∼250 K. However, the high temperature post-deposition heat treatment (900 °C for 4 hours) of MP deposited films used here in Chapter 3 significantly increased film porosity. As such, many free $NiFe_2O_4$ and NiO surfaces were not in contact with each other, resulting in lower interfacial densities, limiting the magnitude of the exchange bias effect.

Chapter 4 explored heating the substrate during deposition (175 °C) for direct deposition of a biphasic $NiFe_2O_4$/NiO film with inherently high interfacial density. This film exhibited exchange bias phenomenon at low temperatures, but not at room temperature. The disappearance of the exchange bias effect at higher temperatures was attributed to spin glass coupling that arose from structurally disordered regions at $NiFe_2O_4$/NiO interfaces. Systematic post-deposition heat treatments of this film revealed that the structurally disordered regions at the interface disappeared after annealing at a temperature of 850 °C for 4 hours, and that the exchange bias witnessed in this film was due to direct coupling between NiO and $NiFe_2O_4$. The films annealed between 400 and 600 °C showed very high room temperature coercivities ranging from 500 to 1100 Oe, with the latter being the highest reported value for the $NiFe_2O_4$/NiO system. These large room temperature coercivities highlight the feasibility of using microplasma-based deposition of exchange bias materials for ultra-high density storage applications.

MP jets were also utilized to deposit high-surface area, Fe-doped NiO films of different composition (up to 20% Fe on a metals basis) at room temperature on ITO substrates for OER catalysis as discussed in Chapter 5. It was seen that Fe fully incorporated into the NiO rocksalt lattice, resulting in a metastable Fe-doped phase that is not thermodynamically stable (i.e., < 1 at% Fe is the solubility limit in rocksalt NiO below 600 °C [1]). The pure NiO phase formed as a dense packing of highly crystalline and textured pyramidal

columns. Film crystallinity, texture and grain size decreased with an increase in the Fe doping level of the rocksalt NiO. A large decrease in overpotential for OER from the pure-phase NiO film to the Fe-doped samples was seen (i.e., 360 vs. 320 mV @ 10 mA/cm^2 for NiO and $Ni_{0.95}Fe_{0.05}O$ films, respectively). The overpotential did not very considerably with Fe composition between 5–19% (i.e., 310 to 325), but the turn-over-frequency (TOF) increased with Fe content, demonstrating an improvement in the catalytic activity of the NiO surface with doping. Chronopotentiometry and post-run XPS and SEM measurements verified that microplasma deposited Fe-doped NiO electrocatalytsts were mechanically and chemically stable during operation at OER conditions. The results from this chapter demonstrate that MP jet deposition is an attractive synthesis route to realize highly active and robust Fe-doped NiO electrocatalysts for OER.

6.2 Future Work

Investigation of MPs as sources for nanomaterial synthesis is a relatively new research field, and very little effort has been focused on exploring their application for thin film deposition. As such, there are plenty of fruitful research projects focusing on MP deposition of thin films that have yet to be explored. For example, MPs offer a tailor-made synthesis approach to realize high surface area, nanostructured metal oxide electrode materials for application in energy conversion and storage. The following sections discuss further experiments for magnetic exchange bias and electrocatalytic studies to build off the findings from this dissertation, as well as future research projects for MP-based growth of metal oxide thin films for energy storage and conversion.

6.2.1 Exchange bias and magnetic hardening

As discussed in Chapters 3 and 4, the exchange bias effect is a complicated magnetic phenomenon that depends on a number of physical properties, including FM and AFM material, grain size, interface quality, and interfacial density. It was demonstrated that MP jet deposition of biphasic $NiFe_2O_4$/NiO films is possible with substrate heating during deposition. However, the relatively low substrate temperatures used in this work ($\leq$ 175 °C) resulted in disordered $NiFe_2O_4$/NiO interfaces that led to spin glass coupling, which is undesirable for ultra-high density data storage. These findings can be augmented by systematically varying the substrate temperature during growth to assess how temperature affects film morphology, grain size, crystallinity, interfacial structure and density, and magnetic response.

To appropriately characterize the distribution of $NiFe_2O_4$ and NiO phases, and to assess the $NiFe_2O_4$/NiO interfacial density and quality, high-resolution transmission electron microscope (TEM) techniques are needed. Scanning TEM (STEM) can be used to get atomic resolution images, enabling the structure of $NiFe_2O_4$/NiO interfaces to be evaluated. Moreover, electron tomography can be used to generate 3D images with < 10 nm resolution, allowing distribution of $NiFe_2O_4$ and NiO phases, interfaces, porosity and grain size to be visualized. Figure 6.1 highlights the preliminary work we have done using electron tomography to visualize $NiFe_2O_4$/NiO films. By combining these techniques with energy dispersive x-ray spectroscopy (EDX) or electron energy loss spectroscopy (EELS), elemental mapping similar to Figure 3.4 can be realized, and used to distinguish NiO from $NiFe_2O_4$.

In addition to using more advanced characterization tools to study biphasic materials, microplasma jet deposition can be extended to other exchange bias systems. For example, $CoFe_2O_4$ (FiM) / CoO (AFM) is also a spinel/rocksalt system that exhibits

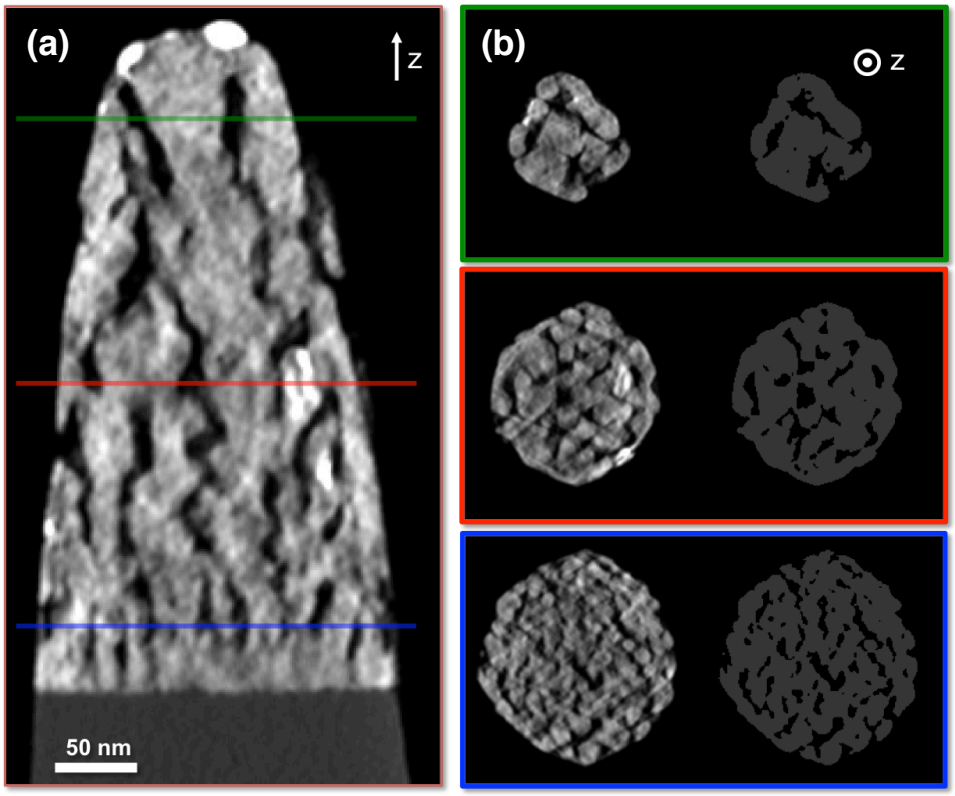

Figure 6.1: (a) Side profile and (b) cross sectional electron tomographs of a focused ion beam (FIB) prepared segment of a $NiFe_2O_4$/NiO film deposited with an Ar/O_2 MP jet.

the exchange bias effect and/or magnetic hardening [2–5]. Interestingly, this system shows more promise for magnetic hardening applications than $NiFe_2O_4$/NiO because the anisotropy energy of the AFM CoO is higher than that of NiO [6], and the magnitude of the exchange bias effect is directly proportional to the AFM anisotropy energy. Seeing that microplasma-deposited $NiFe_2O_4$/NiO films exhibited room temperature exchange bias and the largest reported coercivity for this system, there exists an exciting opportunity to deposit and study $CoFe_2O_4$/CoO for next generation data storage media.

6.2.2 Electrocatalysis

The high catalytic activity of the Fe-doped NiO films for OER discussed in Chapter 5 demonstrates the promise of MP jet deposition for energy conversion technologies. It was shown that by varying precursor composition, the doping levels in NiO films could be controlled, and the activity of the NiO surface improved; however, the overpotential measured at 10 mA/cm^2 did not vary considerably with Fe content. This is partly due to the drastic change in morphology, where the crystallinity and surface area of the film decreased with increasing Fe content. Preliminary results shown in Figure 2.8 suggest that by heating the substrate during deposition, the highly crystalline columnar morphology of pure phase NiO (c.f. Figure 5.3(a) and (b)) can be maintained with high Fe incorporation. However, as presented in Chapter 4, heat from the substrate can assist in the formation of $NiFe_2O_4$ during growth. As such, it would be of utmost importance to determine the range of compositions and substrate temperatures at which Fe-doped NiO and biphasic $NiFe_2O_4$/NiO form.

In addition to a decrease in crystallinity and surface area with Fe composition, the lack of a dependence of overpotential with Fe content in Fe-doped NiO films was attributed to mass transport phenomena and variations in film thickness and electrical conductivity. Performing all electrochemical measurements with a rotating disk electrode (RDE) will help eliminate any mass transport effects that would otherwise *underrepresent* the actual activity of our Fe-doped NiO films [7]. All Fe-doped NiO films studied in Chapter 5 were between 650 and 900 nm thick, which is significantly thicker than what is usual for OER catalysts (< 100 nm). The resistance of the film increases with thickness, and a non-negligible voltage drop across the film could occur, which would also *underrepresent* the actual activity of the film. To exacerbate the problem, increasing Fe content in NiO has been shown to improve the electrical conductivity of the electrode [8], which

means that the voltage drop is not the same among Fe-doped NiO films with different compositions. For this reason, it would be worthwhile to study how film thickness in MP jet deposited Fe-doped NiO films affects the resulting catalytic behavior for OER. This study would focus on how deposition time influences not only film thickness, but also the time-dependent evolution of film morphology, crystallinity, and surface area.

Furthermore, exploring how other MP operating parameters (e.g., gas composition, plasma power, and operating pressure) influence Fe-doped NiO film morphology is an interesting research topic. For example, introducing reactive oxygen gas in the jet vs. the background can lead to drastically different film morphologies, crystallinities and surface areas as shown in Figure 6.2. Supplying the oxygen source directly into the reactive environment of the hollow-cathode is critical for formation of highly crystalline NiO columns (Figures 6.2(a) and (b)). If O_2 is introduced into the background, where it interacts with the plume of the MP jet, columnar structures comprised of small (< 5 nm) nanoparticles form (Figures 6.2(c) and (d)). The crystallinity decreases significantly when O_2 is introduced in the background instead of directly in the hollow cathode jet as shown from the XRD scans in Figure 6.2(e). The CV behavior of these two films, however, is quite similar except for the size of the redox peaks (Figure 6.2(f)). The larger redox peaks for the NiO film deposited with O_2 in the background may be attributed to the thickness of the film, which is greater than that for the film deposited with O_2 in the jet. Consequently, this may result in a larger total surface area of NiO exposed to the electrolyte, and the 'apparent' enhanced reaction rate. A detailed investigation of the effects of O_2 concentration in the MP jet on film morphology and electrochemical response is necessary to further our understanding of the role oxygen plays on thin film growth of NiO and Fe-doped NiO films.

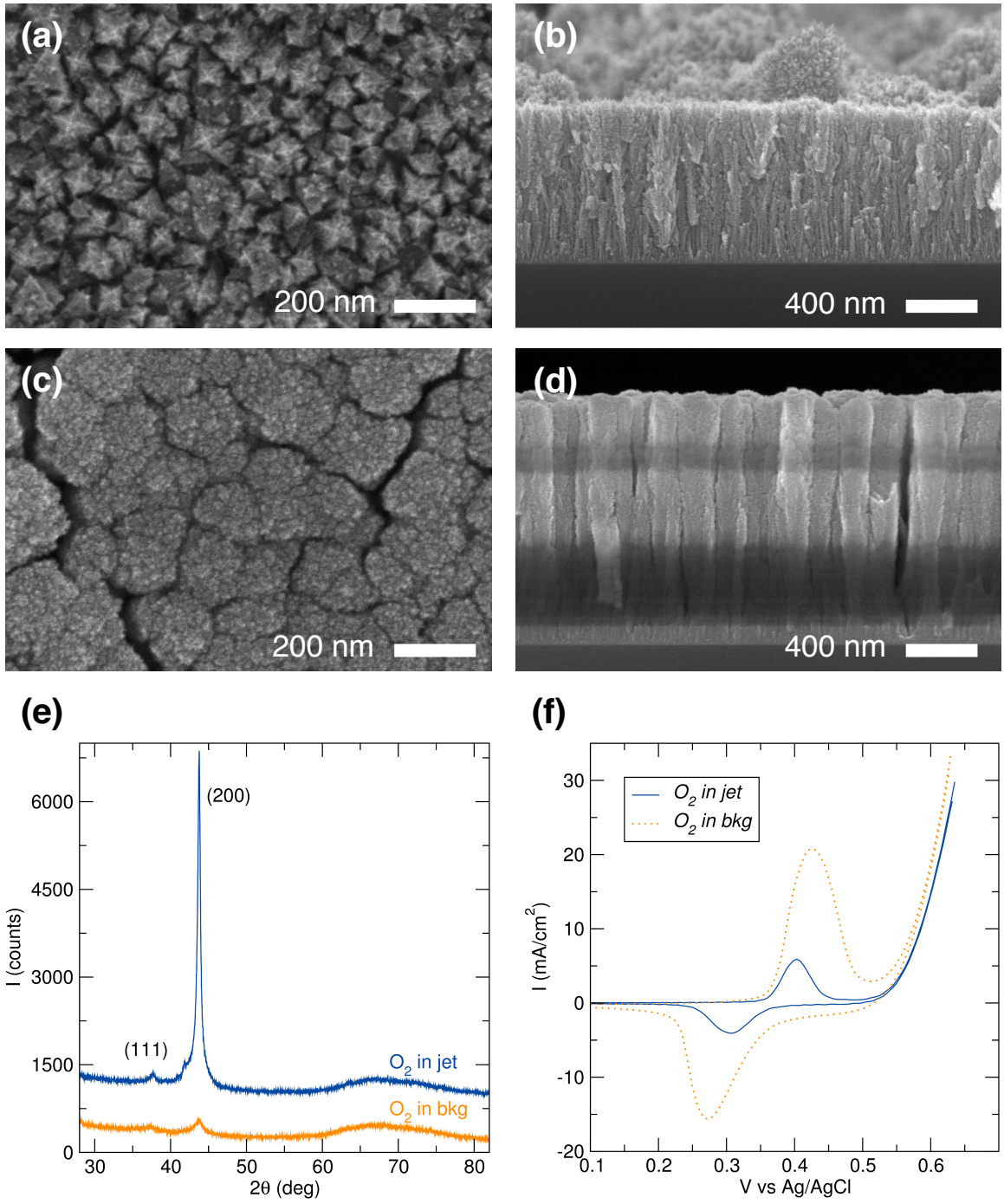

Figure 6.2: Plan and cross-sectional SEM micrographs of NiO films deposited using an Ar microplasma jet with O_2 (a,b) in the jet, and (c,d) in the background. (e) XRD and (f) CV scans of the two NiO films shown in (a)-(d).

6.2.3 NiO electrodes for Li-ion batteries

Li-ion batteries have been extensively investigated for consumer electronics, and for high-energy applications such as storage systems for renewable energy sources and electric vehicles. Traditional Li-ion batteries store charge through the Faradaic process of intercalation of Li^+ ions between layers of the anode material (e.g., $Li(Ni_{0.5}Mn_{0.5})O_2$ and $LiCoO_2$) [9]. Unfortunately, on average, only half an electron is transferred per metal site, and the electrodes require very specific structures and properties [10]. This results in relatively low theoretical specific energy densities, and requires difficult processing to fabricate the complex electrode structure. A potential way to eliminate these drawbacks is to use electrodes that can transfer more than one charge per metal site through metal-oxide redox reactions. This is known as a conversion or displacement type electrode, which has an inherently higher specific energy density than intercalation-based electrodes. Li-ion batteries are inherently limited in how fast they can be charged or discharged due to kinetic limitations from diffusion of Li^+ ions to and from the anode. To improve performance, high-energy densities need to be maintained over faster charging and discharging rates. It has been shown that by creating nanostructured anodes, the rate capability (i.e., maintaining high energy densities over a wide range of charge and discharge rates) can be drastically improved due to short diffusion length and the large surface-to-volume that allows for large area contact between the anode and electrolyte [11].

Nanostructured NiO has been widely studied, and demonstrates very good electrochemical properties to act as the anode in Li-ion based batteries, where the reversible reaction can be summarized by [11–14]:

$$NiO + 2Li^+ + 2e^- \longleftrightarrow Ni + LiO_2 \tag{6.1}$$

Wang *et al.* demonstrated that nanostructured NiO synthesized via thermal oxidation of a porous Ni foam substrate shows high specific capacities of ∼700 mAh/g at a (dis)charge rate of 5 hours/(dis)charge. The capacity remains relatively high at ∼400 mAh/g when the battery is allowed to fully discharge over a much faster rate of 6 minutes/(dis)charge, exhibiting the good rate capability of NiO. More importantly, when the (dis)charge rate is returned to its initial cycle rate of 5 hours/(dis)charge, the original capacity of ∼700 mAh/g is again observed [11]. Unfortunately, using thermal oxidation to form nanostructured NiO makes it an inflexible method for deposition on non-Ni based substrates.

In addition to thermal oxidation of Ni foam substrates, many groups have used hydrothermal synthesis and solid state methods to form NiO and $Ni(OH)_2$ nanoparticles [15, 16]. These approaches generally require binders to adhere the nanostructured particles to the anode (e.g., carbon steel), resulting in a heavier electrode, and therefore, a lower specific energy density. Moreover, doping of NiO with Co has been shown to exhibit exceptional capacities and good cycle life as the anode in Li-ion batteries [17]. The ability to create conformal coatings of highly crystalline NiO and doped NiO films with small grain sizes and high-surface areas on virtually any surface [18] make microplasmas ideal for synthesis of anode materials for Li-ion batteries. As such, there exists an intriguing opportunity to use microplasma jet deposition of nanostructured NiO and Co-doped NiO films on high surface area substrates, such as Ni foams and carbon cloth, for Li-ion battery applications.

6.2.4 Metal oxide films for pseudocapacitors

Pseudocapacitors (or electrochemical supercapacitors) are energy storage devices that exhibit electrochemical behavior similar to both a battery and a supercapacitor [19, 20]. As discussed in the previous section, batteries store charge through Faradaic processes (i.e., ion intercalation or redox reactions), resulting in high specific energy densities. However, the mechanism of energy transfer in batteries is kinetically limited by the diffusion of ions between electrodes, which explains why they exhibit such low specific power densities. Supercapacitors, on the other hand, have large specific power densities because they can be charged and discharged very quickly (< 1 min), but the surface area of the electrode limits the total charge stored, and therefore, high specific energy densities are not achievable. Pseudocapacitors store charge through Faradaic processes like batteries, but are not kinetically limited by ion diffusion, resulting in a device that has both high specific energy *and* power densities. Being able to store and deliver large amounts of energy quickly is highly desirable for regenerative braking, pulse-power in communication devices, and power quality applications in the power grid [21]. Furthermore, shorter charging times would be convenient for portable electronic devices and electric vehicles.

Unfortunately, many publications claim pseudocapacitive behavior of their electrode materials, when they actually behave more like a battery [22]. Figure 6.3 clearly demonstrates the difference between a pseudocapacitor and a battery using galvanostatic methods [23]. A pseudocapacitor will display a linear time-dependent voltage change at a constant current as shown in Figure 6.3(a) for both a bulk and nanoscale electrode. A galvanostatic measurement for a battery will display a plateau region at the redox potential of the electrode (Figure 6.3(b)). Pseudocapacitance can be either intrinsic to the material, or extrinsic, meaning that the electrode architecture and/or morphology can be manipulated in such a way to exhibit pseudocapacitor-like behavior. For example,

the galvanostatic response of a nanostructured $LiCoO_2$ battery electrode behaves like a pseudocapacitor as shown in Figure 6.3(b) [23].

The most well known and studied pseudocapacitors are RuO_2 [24] and MnO_2 [25], but nanostructured NiO, $NiCo_2O_4$, and Ni-Co oxides and hydroxides have recently demonstrated exceptional pseudocapacitive behavior [26–29]. MP jet deposition appears to be an ideal technique for the synthesis of high surface area, nanostructured metal oxide electrodes for these applications.

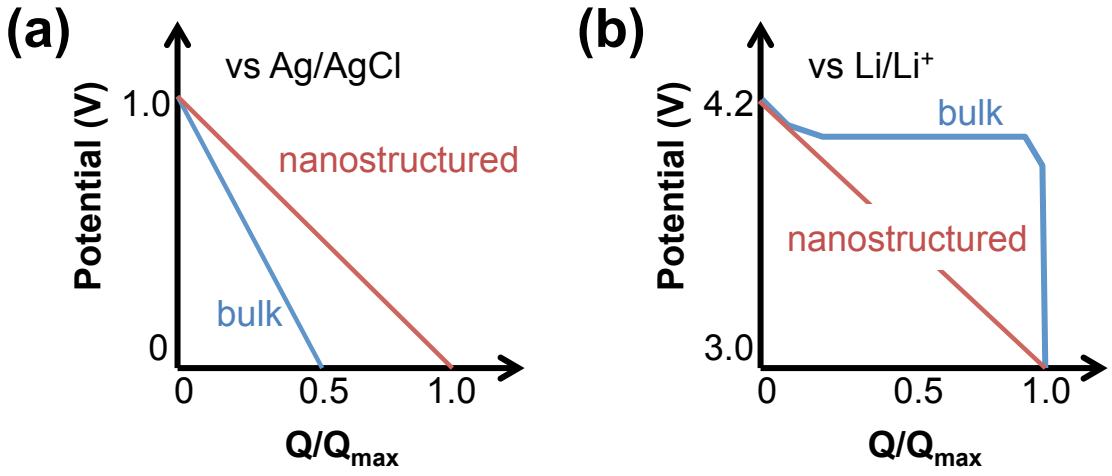

Figure 6.3: Galvanostatic discharge behavior where Q is charge for (a) bulk and nanostructured MnO_2 pseudocapacitor, and (b) bulk and nanostructured $LiCoO_2$ battery electrode. Adapted from Ref. [23].

6.3 Conclusions

The work in this dissertation demonstrated the versatility of MP jet deposition to realize a variety of complex Ni-Fe oxide films, ranging from biphasic $NiFe_2O_4$/NiO and metastable Fe-doped NiO films. A wide range of morphologies, structures, and compositions were realized on many different substrates by varying MP operating conditions, which included precursor composition, flux, substrate temperature, and gas composition. The ability to achieve nanostructured crystalline materials with high interfacial densities and surface areas resulted in exceptional magnetic hardening and electrochemical properties for potential data storage and energy conversion technologies, respectively. Moreover, this work demonstrated that MPs offer a general, one step approach to realize conformal coatings of high surface area oxide materials that should be explored as electrode materials for next generation energy storage devices (i.e., batteries and pseudocapacitors).

The main conclusions drawn from this body of work are:

1. MP jets can be used to deposit biphasic $NiFe_2O_4$/NiO materials at elevated substrate temperatures (175 °) or metastable Fe-doped NiO films at room temperature, where the solubility limit of Fe in rocksalt NiO has been extended up to 19 mol% on a metals basis.

2. Increasing NiO content from 7 to 56 vol% in $NiFe_2O_4$/NiO films created with MP jets and post-deposition annealing results in a larger exchange bias shift and coercivity due to an increase in interfacial contact between the $NiFe_2O_4$ and NiO phases.

3. Spin glass coupling, which forms due to structural disorder at interfaces, is prevalent in MP jet deposited $NiFe_2O_4$/NiO films, resulting in a large exchange bias effect at low temperatures that disappears above 250 K. Post-deposition annealing improves

the crystallinity of interfaces, and at annealing temperatures of 850 °C and higher, the observed exchange bias is from direct coupling between $NiFe_2O_4$ and NiO, where the SG-like phase is no longer present.

4. MP jets can be used to create high surface area, metastable Fe-doped NiO films as active catalysts for OER. Increasing Fe doping levels up to 19 mol% lead to an improvement in the catalytic activity of the NiO surface. Additionally, the crystallinity of the Fe-doped NiO films results in chemically and structurally robust catalysts for extended operation at OER relevant conditions.

References

[1] M. Rhamdhani, P. Hayes, and E. Jak, "Subsolidus phase equilibria of the Fe-Ni-O system," *Metall. Mater. Trans. B*, vol. 39, no. 5, pp. 690–701, 2008.

[2] E. Lima Jr, E. L. Winkler, D. Tobia, H. E. Troiani, R. D. Zysler, E. Agostinelli, and D. Fiorani, "Bimagnetic CoO core/$CoFe_2O_4$ shell nanoparticles: synthesis and magnetic properties," *Chem. Mater.*, vol. 24, no. 3, pp. 512–516, 2012.

[3] X. Zhao, Y. Zhang, S. Xu, X. Lei, and F. Zhang, "Oriented $CoFe_2O_4$/CoO nanocomposite films from layered double hydroxide precursor films by calcination: ferromagnetic nanoparticles embedded in an antiferromagnetic matrix for beating the superparamagnetic limit," *J. Phys. Chem. C*, vol. 116, no. 9, pp. 5288–5294, 2012.

[4] Y. Zhang, F. Dong, Y. Liu, C. Fei, C. Pan, D. Yin, R. Xiong, and J. Shi, "Synthesis and exchange bias effect of $CoFe_2O_4$/CoO composite ceramics," *Mater. Chem. Phys.*, vol. 124, no. 2, pp. 1034–1038, 2010.

[5] G. C. Lavorato, E. Lima Jr, D. Tobia, D. Fiorani, H. E. Troiani, R. D. Zysler, and E. L. Winkler, "Size effects in bimagnetic CoO/$CoFe_2O_4$ core/shell nanoparticles," *Nanotechnology*, vol. 25, no. 35, p. 355704, 2014.

[6] L. Duò, M. Finazzi, and F. Ciccacci, *Magnetic Properties of Antiferromagnetic Oxide Materials: Surfaces, Interfaces, and Thin Films*. John Wiley & Sons, 2010.

[7] M. W. Louie and A. T. Bell, "An investigation of thin-film Ni–Fe oxide catalysts for the electrochemical evolution of oxygen," *J. Am. Chem. Soc.*, vol. 135, no. 33, pp. 12329–12337, 2013.

[8] L. Trotochaud, S. L. Young, J. K. Ranney, and S. W. Boettcher, "Nickel–iron oxyhydroxide oxygen-evolution electrocatalysts: the role of intentional and incidental iron incorporation," *J. Am. Chem. Soc.*, vol. 136, no. 18, pp. 6744–6753, 2014.

[9] K. Kang, Y. S. Meng, J. Bréger, C. P. Grey, and G. Ceder, "Electrodes with high power and high capacity for rechargeable lithium batteries," *Science*, vol. 311, no. 5763, pp. 977–980, 2006.

[10] R. Malini, U. Uma, T. Sheela, M. Ganesan, and N. Renganathan, "Conversion reactions: a new pathway to realise energy in lithium-ion battery—review," *Ionics*, vol. 15, no. 3, pp. 301–307, 2009.

[11] X. Wang, X. Li, X. Sun, F. Li, Q. Liu, Q. Wang, and D. He, "Nanostructured NiO electrode for high rate Li-ion batteries," *J. Mater. Chem.*, vol. 21, no. 11, pp. 3571–3573, 2011.

[12] B. Varghese, M. Reddy, Z. Yanwu, C. S. Lit, T. C. Hoong, G. Subba Rao, B. Chowdari, A. T. S. Wee, C. T. Lim, and C.-H. Sow, "Fabrication of NiO nanowall electrodes for high performance lithium ion battery," *Chem. Mater.*, vol. 20, no. 10, pp. 3360–3367, 2008.

[13] H. Wang, Q. Pan, X. Wang, G. Yin, and J. Zhao, "Improving electrochemical performance of NiO films by electrodeposition on foam nickel substrates," *J. Appl. Electrochem.*, vol. 39, no. 9, pp. 1597–1602, 2009.

[14] X. Li, A. Dhanabalan, K. Bechtold, and C. Wang, "Binder-free porous core–shell structured Ni/NiO configuration for application of high performance lithium ion batteries," *Electrochem. Commun.*, vol. 12, no. 9, pp. 1222–1225, 2010.

[15] M. Freitas, "Nickel hydroxide powder for NiOOH/Ni$(OH)_2$ electrodes of the alkaline batteries," *J. Power Sources*, vol. 93, no. 1, pp. 163–173, 2001.

[16] P. Poizot, S. Laruelle, S. Grugeon, L. Dupont, and J. Tarascon, "Nano-sized transition-metal oxides as negative-electrode materials for lithium-ion batteries," *Nature*, vol. 407, no. 6803, pp. 496–499, 2000.

[17] Y. Mai, J. Tu, X. Xia, C. Gu, and X. Wang, "Co-doped NiO nanoflake arrays toward superior anode materials for lithium ion batteries," *J. Power Sources*, vol. 196, no. 15, pp. 6388–6393, 2011.

[18] K. E. Mackie, A. C. Pebley, M. M. Butala, J. Zhang, G. D. Stucky, and M. J. Gordon, "Microplasmas for direct, substrate-independent deposition of nanostructured metal oxides," *Appl. Phys. Lett.*, vol. 109, no. 3, p. 033110, 2016.

[19] G. Wang, L. Zhang, and J. Zhang, "A review of electrode materials for electrochemical supercapacitors," *Chem. Soc. Rev.*, vol. 41, no. 2, pp. 797–828, 2012.

[20] M. Zhi, C. Xiang, J. Li, M. Li, and N. Wu, "Nanostructured carbon–metal oxide composite electrodes for supercapacitors: a review," *Nanoscale*, vol. 5, no. 1, pp. 72–88, 2013.

[21] V. Augustyn, P. Simon, and B. Dunn, "Pseudocapacitive oxide materials for high-rate electrochemical energy storage," *Energy Environ. Sci.*, vol. 7, no. 5, pp. 1597–1614, 2014.

[22] T. Brousse, D. Bélanger, and J. W. Long, "To be or not to be pseudocapacitive?," *J. Electrochem. Soc.*, vol. 162, no. 5, pp. A5185–A5189, 2015.

[23] P. Simon, Y. Gogotsi, and B. Dunn, "Where do batteries end and supercapacitors begin?," *Science*, vol. 343, no. 6176, pp. 1210–1211, 2014.

[24] J. Zheng and T. Jow, "A new charge storage mechanism for electrochemical capacitors," *J. Electrochem. Soc.*, vol. 142, no. 1, pp. L6–L8, 1995.

[25] V. Subramanian, H. Zhu, R. Vajtai, P. Ajayan, and B. Wei, "Hydrothermal synthesis and pseudocapacitance properties of MnO_2 nanostructures," *J. Phys. Chem. B*, vol. 109, no. 43, pp. 20207–20214, 2005.

[26] M. Huang, C. Gu, X. Ge, X. Wang, and J. Tu, "NiO nanoflakes grown on porous graphene frameworks as advanced electrochemical pseudocapacitor materials," *J. Power Sources*, vol. 259, pp. 98–105, 2014.

[27] C. Yuan, J. Li, L. Hou, X. Zhang, L. Shen, and X. W. D. Lou, "Ultrathin mesoporous $NiCo_2O_4$ nanosheets supported on ni foam as advanced electrodes for supercapacitors," *Adv. Funct. Mater.*, vol. 22, no. 21, pp. 4592–4597, 2012.

[28] B. Liu, D. Kong, Z. X. Huang, R. Mo, Y. Wang, Z. Han, C. Cheng, and H. Y. Yang, "Three-dimensional hierarchical $NiCo_2O_4$ nanowire@ Ni_3S_2 nanosheet core/shell arrays for flexible asymmetric supercapacitors," *Nanoscale*, vol. 8, no. 20, pp. 10686–10694, 2016.

[29] L. Huang, D. Chen, Y. Ding, S. Feng, Z. L. Wang, and M. Liu, "Nickel–cobalt hydroxide nanosheets coated on $NiCo_2O_4$ nanowires grown on carbon fiber paper for high-performance pseudocapacitors," *Nano Lett.*, vol. 13, no. 7, pp. 3135–3139, 2013.